NAA-SR-11502

COPY

THERMAL BEHAVIOR OF SNAP REACTOR FUEL ELEMENTS DURING ATMOSPHERIC REENTRY

AEC Research and Development Report

ATOMICS INTERNATIONAL
A DIVISION OF NORTH AMERICAN AVIATION, INC.

DISCLAIMER

Printed in USA. Price $4.00 . Available from the Clearinghouse for Federal Scientific and Technical Information, National Bureau of Standards, U. S. Department of Commerce, Springfield, Virginia

NAA-SR-11502
AEROSPACE SAFETY
124 PAGES

CFSTI PRICES

H.C. $ 4.00 ; MN 1.00

THERMAL BEHAVIOR OF SNAP REACTOR FUEL ELEMENTS DURING ATMOSPHERIC REENTRY

By

A. W. BARSELL
L. D. MONTGOMERY
J. E. ARNOLD

ATOMICS INTERNATIONAL

A DIVISION OF NORTH AMERICAN AVIATION, INC.

CONTRACT: AT(11-1)-GEN-8
ISSUED: MAR 25 1966

DISTRIBUTION

This report has been distributed according to the category "Aerospace Safety" as given in the Standard Distribution for Unclassified Scientific and Technical Reports, TID-4500. The edition used was the one currently in effect on the date this document was issued.

ACKNOWLEDGMENT

The authors wish to express their appreciation to K. Y. Eng, for analytical work performed on the chemical reactions of the fuel with air during reentry, and to S. R. Fields, for active guidance and assistance throughout the course of this study.

CONTENTS

CONTENTS

TABLES

TABLES

FIGURES

FIGURES

FIGURES

BLANK

ABSTRACT

An analytical model is developed to describe the thermochemical behavior of SNAP reactor fuel elements during atmospheric reentry. The aerodynamic heating, transpiration cooling, and the chemical reactions of the fuel with air are investigated. A detailed evaluation of zirconium-uranium hydride fuel material properties is presented. Results using the analytical model are presented and compared with experimental data.

A statistical probability analysis of initial fuel ablation is conducted for SNAP 10A elements. The statistical procedure is concluded to be a valid, optimum approach Parameter influence is precisely fixed and ranked, providing direction for experimental support investigations. The procedure also enables an organized, reiterative narrowing of the accuracy attributed to the study results.

SUMMARY

Analytical studies of the transient behavior of zirconium-uranium hydride SNAP reactor fuel elements under atmospheric reentry conditions have been undertaken to describe the conditions which are necessary for burnup and dispersal of the radioactive fuel material. In this report, trajectory transient calculations are made for SNAP 10A reactor fuel elements released from the reactor vehicle at selected altitudes between 200,000 and 400,000 ft. The aerodynamic heating, transpiration cooling, and the chemical reactions of the fuel with air are analyzed to determine the net surface heat flux to the elements. An analytical model is described with which simultaneous solutions of the heat and hydrogen transport equations are obtained including variable material properties and material phase changes.

A detailed evaluation of present available information concerning fuel material properties is given. Using the best available data, minimum fuel element ejection altitudes are estimated from which complete ablation of the fuel can be achieved. The computations are performed for fuel element trajectories with cross-axial-spinning, end-over-end-tumbling, and random-tumbling flight orientations. A statistical analysis of the computations is presented, from which probabilities of initial fuel ablation are derived as a function of release altitude. The statistical procedure is concluded to be a valid and optimum method of analysis. The influence of each parameter may be precisely determined and ranked to provide direction for experimental support investigations. The procedure also enables an organized, reiterative narrowing of the accuracy attributed to the study results.

Data from experimental tests on the transient heating and burnup of the fuel material in a hyperthermal wind tunnel are used to correlate the analytical description. The agreement is found to be good and within deviation due to uncertainties in parameters.

I. INTRODUCTION

The safe disposal of the zirconium-uranium hydride fuel in SNAP (Systems for Nuclear Auxiliary Power) reactors during atmospheric reentry has been a primary concern in the Aerospace Nuclear Safety Program. Burnup and dispersal of the fuel as a result of aerodynamic heating has been considered as a practical and convenient method of diluting the fission products to a harmless level in the atmosphere.

In recent years, an analytical and experimental program to investigate the reentry behavior of SNAP reactors and the radioactive fuel material upon descent from satellite orbits has been pursued at Atomics International. Investigations of the reentry heating and disintegration of the SNAP 10A reactor vehicle system have been reported in References 1 through 4. These studies, along with the study presented in Reference 5, have shown that the disintegration of the reactor system proceeds to an extent where individual fuel elements are released and subjected directly to aerodynamic heating at about 240,000 ft.

The study of the reentry heating and thermophysical behavior of the released fuel elements is the subject of this report. This report contains a description of the analytical methods developed to attain a rigorous and comprehensive evaluation of the reentry behavior, and a demonstration of these methods to arrive at some preliminary results.

Several previous studies have been made by separate investigators of the reentry behavior of zirconium-uranium hydride fuel elements. The earliest of these was an AVCO Corporation report,[6] which defined and discussed the phenomena and problems involved. In other studies, preliminary analytical models to approximate the thermophysical behavior of the fuel material during reentry were developed by Childers et al.,[7] and by Leadon et al.[8] These models are roughly equivalent to the preliminary analytical fuel burnup model[1, 9] developed at Atomics International to analyze the results of the first series of experimental tests on SNAP fuel material heated in a hyperthermal wind tunnel[9] and to perform preliminary reentry calculations. All of these models, however, were not deemed to be of sufficient accuracy to meet the specific requirements and objectives of the Aerospace Nuclear Safety Program.

In this report, an analytical model is developed which incorporates all known processes occurring at or near the fuel element surface and within the fuel material. More specifically, the model generates simultaneous heat and mass transfer solutions considering (1) temperature and hydrogen concentration dependent material properties, (2) material phase changes, and (3) a complex surface heat flux which varies with time, surface temperature, and the hydrogen loss rate. In addition, fusion and ablation of the cladding and fuel material are simulated. A principal advantage of this analytical model is that it utilizes a known, familiar computer code (Thermal Analyzer Program, TAP-3) for obtaining these solutions.

The determination of the net surface heat flux to the fuel element is based on an evaluation of the aerodynamic heating, transpiration cooling, and the heating contributions of the surface chemical reactions. Such reactions are (1) oxidation of the fuel material and (2) hydrogen combustion. An evaluation of each of these processes is presented in Section IV.

Superscript numbers refer to the References listed in Section 10 of this report.

The analysis contained in the main body of this report is confined to fuel element flight orientations which effect a uniform heating around the surface of the element. Such orientations are: (1) cross-axial spinning, (2) random tumbling, and (3) end-over-end tumbling. In these cases, the analysis is simplified to a one-dimensional, radial description. Such a description begins with a fully clad fuel element, released at a given altitude along the reference vehicle trajectory, at a given initial temperature, and revolving in one of the aforementioned flight orientations. The material response of the fuel element following release is then computed by means of the analytical model upon specification of the aerodynamic heating, stagnation enthalpy, and fraction of completion for hydrogen combustion, all as functions of time.

The case of a cross-axial, nonrotating flight orientation is treated in an appendix section. This orientation results in a heating distribution around the circumference of the element with maximum heating occurring along the stagnation line of the cylinder. A two-dimensional version of the analytical model is developed to describe the fuel behavior up to initial fuel melting for this flight orientation.

The overall fuel element reentry behavior, including evaluation of the trajectory heating and the material response calculations, has been analyzed using statistical methods. The objective of this statistical analysis is to pinpoint those parameters and processes requisite of further experimental and analytical research and to arrive at probabilities of fuel element survival or burnup for the conditions considered. Such a program of statistical analysis is outlined in Section VIII of this report. The process of analysis is shown to be iterative. That is, with each set of subsequent data factored in, the process is repeated to further refine the accuracy of the analytical method and the corresponding results.

II. INITIAL CONDITIONS AT FUEL ELEMENT RELEASE

A. REFERENCE TRAJECTORY AND RELEASE ALTITUDE

In order to properly evaluate the reentry performance of a SNAP fuel element, the conditions, location, and dynamics of the element at the instant of its release from the reactor must be known. Where is the element with respect to the earth at the time of its release? How fast is it traveling? How is it spinning or tumbling? What is the initial temperature and hydrogen composition? The answer to each of these questions influences the calculated thermal behavior of the element during descent.

The fuel element calculations reported in this document are based, in large part, on the normal sequence of events for the SNAP 10A-Agena vehicle during reentry following orbital decay. Investigations of the reentry behavior of the SNAP 10A system are described in References 1 through 5.

The results of these studies show that both the nominal and non-nominal orbits decay to a narrow range of velocities and reentry angles at 400,000-ft altitude. This altitude represents the upper limit of the sensible atmosphere and is frequently used as a starting point for reentry calculations. Below 400,000 ft, the vehicle will not make another complete circuit of the earth due to the energy dissipated in atmospheric drag. Initial ablation and breakup of the reactor system is estimated to occur in the altitude range from 300,000 to 275,000 ft. The breakup of the reactor is followed by the exposure and release of the individual fuel elements at an estimated altitude of about 240,000 ft. The fuel elements separate and continue on independent trajectories characterized by the imparted velocities, altitudes, flight path angle, and the fuel element drag coefficient. The basic assumption is made that the fuel elements possess the velocity and flight path angle of the parent vehicle at the instant of their release.

As a consequence of the reactor disintegration studies, fuel element behavior calculations were first made for a spectrum of release altitudes focused around 240,000 ft. The range was then extended to include release altitudes from 400,000 to 200,000 ft. Fuel element calculations made over this broad range were patterned to assist in determining optimum release altitudes and optimum orbital decay schemes in which atmospheric burnup and dispersal of the fuel material could be assured.

From the narrow range of parent vehicle decay trajectories, a representative trajectory was selected and used as a basis for the individual fuel element trajectories. At 400,000 ft, this reference trajectory has the following characteristics

Orbit	Polar
Longitude	0 degrees
Latitude	90 degrees
Velocity	25,694 ft/sec
Flight Angle	0.05 degrees
$W/C_D A_p$	132 lb/ft^2

Thus, the reference trajectory assumes entry into the sensible atmosphere over the North Pole, traveling at a near-horizontal angle in the direction of the South Pole with circular velocity. Subsequent velocities, altitudes, and aerodynamic heating to the vehicle are shown as a function of time after 400,000 ft in Figure 1. Calculations of these trajectory transients were performed using the RESTORE digital code, outlined in Section IV.

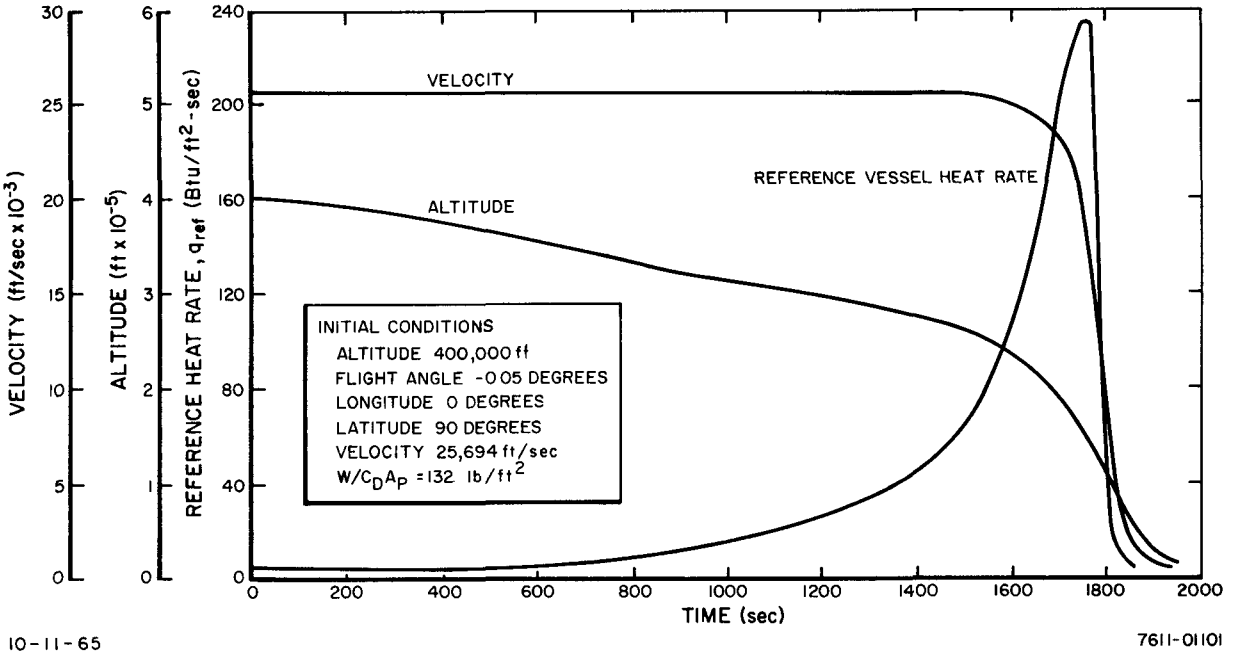

Figure 1. Trajectory Transients for an Orbital Decaying SNAP 10A Reactor Vehicle in a Polar Orbit

B. ATTITUDE AND ANGULAR MOTION

Through a consideration of the angular dynamic motions, it can be shown that, should a fuel element receive even a small angular impulse during release, random tumbling of the elements will occur throughout atmospheric descent. A random tumbling orientation has thus been deemed as the most probable flight mode. Other possible flight orientations include

1) Stabilized cross-axial spinning (axis of rotation perpendicular to line of flight)

2) End-over-end tumbling

3) Stabilized cross-axial nonspinning

4) Stabilized end-on (spear reentry).

The foregoing orientations can be grouped into two categories. Random tumbling, cross-axial spinning, and end-over-end tumbling effect a uniform aerodynamic heating distribution around the cylindrical surface of the fuel element, provided a minimal rotational speed is maintained. This minimal rotational speed has, in other studies, been judged to be on the order of 60 revolutions per min.[8] Of these three orientations, the spinning, cross-axial case results in the lowest average

heat input to a SNAP fuel element. This orientation was often applied in initial material response calculations. End-over-end tumbling results in an average heat input about midway between that for cross-axial spinning and random tumbling.

In a second category are classed those orientations which effect a nonuniform heating distribution on the fuel element surface. End-on reentry is characterized by an intense localized heating on the front flat face of the cylindrical element. Similarly, a nonspinning, cross-axial orientation results in high localized heating along the stagnation line of the cylindrical surface. In these cases, melting of the fuel material should occur sooner and the ablation period should be longer than for those orientations of the first category.

C. TEMPERATURE AND HYDROGEN CONCENTRATION

The initial temperature and hydrogen content of the fuel elements at release are naturally dependent on the sequence of events leading to the separation of the elements from the reactor core. To obtain an appropriate range of initial temperatures, recourse was made to the SNAP 10A reactor disintegration studies[1-4] conducted at Atomics International. The results of calculations made in these studies show that the reactor core will attain a temperature of about 940°F at an altitude of 310,000 ft, if the NaK coolant remains in the system during reentry.[4] If the NaK is lost from the core prior to reentry, the core temperature at the same altitude will be about 100°F, assuming that fission-product-decay heat is negligible.[4] Accounting for the heat release from the fission products, this temperature has been estimated to be about 200 to 450°F, depending on whether reentry is made in sunlight or dark sky. Below 310,000 ft, the reactor system will break up and disintegrate. Heat transfer calculations made for the reactor core without NaK indicate that the vessel wall ablates away with little or no heat transfer to the inner elements of the fuel element bundle. Release temperatures for these elements can then be set at about 200 to 450°F. The outermost elements will be at higher temperatures at release, on the order of 1000°F.

Considering these results, the estimated range of initial temperatures can be given as 200 to 1000°F. In arriving at this temperature range, attention was focused on the lower bound, since higher initial temperatures increase the probability of fuel melting and ablation.

In contrast to the wide initial temperature range, the initial hydrogen concentration of the zirconium-uranium hydride fuel elements is a relatively fixed quantity. The final hydriding composition is set during fuel element fabrication within a close tolerance of less than 1%. This final composition is designed to achieve suitable neutron moderation during normal reactor operation and, at the same time, physical and mechanical property requirements. For example, higher hydrogen concentrations improve neutron moderation but increase the equilibrium hydrogen pressure in the fuel-cladding gap. Higher hydrogen pressures result in greater hydrogen leakage through permeation of the cladding and hydrogen barrier material.

SNAP 10A reactor fuel elements are fabricated with 6.35×10^{22} ($\pm 0.03 \times 10^{22}$) atoms of hydrogen per cm^3 of fuel-moderator material.[10] This number corresponds to 6.61 lb of hydrogen per ft^3. A convenient and frequently used measure of the hydrogen content is the hydrogen-to-zirconium atom ratio (H/Zr). A SNAP 10A fuel element has an H/Zr ratio of 1.80.

Past analysis[10] based on empirical hydrogen leakage data has shown that a SNAP 10A fuel element loses a negligible amount of hydrogen during its full, normal lifetime of operation. After reactor shutdown, the hydrogen is essentially frozen within the fuel element and no further hydrogen loss should occur.

Based on the foregoing analysis, the hydrogen concentration at fuel element release can be set at 6.61 lb of $H_2/ft^3 \pm 1\%$. This corresponds to an initial $H/Zr = 1.80 \pm 0.02$.

III. ANALYTICAL MODEL DESCRIPTION AND EQUATIONS

As stated in the previous section, random tumbling, end-over-end tumbling, and cross-axial spinning orientations can effect a uniform aerodynamic heating distribution around the cylindrical surface of the fuel element. The corresponding material response of the fuel element is then characterized by a one-dimensional radial description. Such a description begins with a fully clad fuel element at a given uniform temperature, released at a given altitude and rotating in one of the three orientations mentioned above. The fuel element is treated as an infinitely long cylinder with radial heat and hydrogen transfer. Heat generation due to fission product decay is neglected commensurate with the assumption of a long (about 3000-yr) orbital lifetime for the SNAP 10A reactor system.

In this section, a delineation is given of the analytical model used for the one-dimensional material response solutions. As explained in Appendix B, two- or three-dimensional solutions can be obtained using a similar model which is a product of the logical compounding of the one-dimensional model processes.

The calculation procedure executed by the analytical model progresses in three successive stages. Beginning at the time of fuel element release or ejection from the reactor vessel, the transient temperatures of the cladding material and the fuel material are computed up to the time of cladding meltdown. In the second stage, the bare fuel material is exposed to aerodynamic heating. At this point, the calculation process is complicated by hydrogen dissociation and migration within the fuel, and by the chemical reactions at the fuel surface. As the fuel reaches the melting temperature, a third stage is initiated in which melting and ablation of the fuel increments are approximated.

A. BEFORE CLADDING BURNOFF

Immediately following fuel element release, the following heat transfer processes are simulated by the analytical model:

1) Aerodynamic heating to the cladding surface

2) Heat storage within the cladding

3) Heat radiation to space

4) Heat radiation across the element gap

5) Heat conduction and storage within the fuel.

An illustration of these processes occurring simultaneously along the radius of the fuel element is shown in Figure 2a.

The heat transfer equation which describes the temperature response of the cladding material is:

$$V_c \rho_c C_{p_c} \frac{\partial T}{\partial t} = A_s \cdot q_{aero} - A_s \Sigma q_{rad} \ , \qquad \ldots(1)^*$$

where

$$\Sigma q_{rad} = \frac{\sigma_1 \left(T_c^{\,4} - T_s^{\,4} \right)}{1/\epsilon_c + 1/\epsilon - 1} + \epsilon_c \sigma_1 T_c^{\,4} \ . \qquad \ldots(2)$$

*The mathematical symbols and terms used throughout this report are defined in Section IX, Nomenclature.

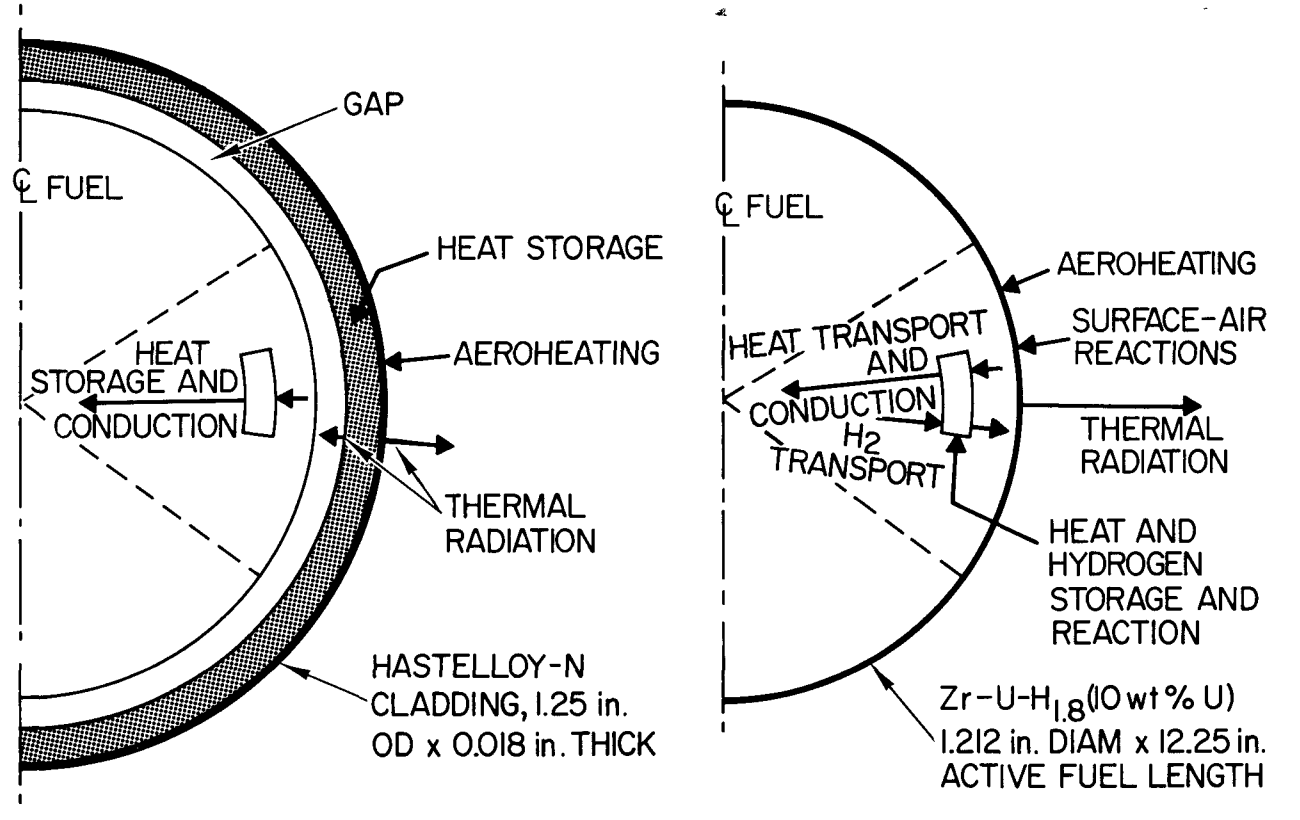

Figure 2. Heat and Mass Transfer Processes

Aerodynamic heating (q_{aero}) to the clad element is computed and specified as a function of time after release as recounted in Section IV. Heat is radiated from the Hastelloy-N cladding to space and across the element gap to the fuel. Heat is conducted and stored within the fuel, but no redistribution of hydrogen is calculated since the hydrogen is contained by the still intact cladding. Side calculations indicate the hydrogen pressure buildup within the element gap is not sufficient for appreciable heat conduction across the gap.

The heat transfer equation which describes the temperature response of the fuel is

$$\rho C_p \frac{\partial T}{\partial t} = \frac{1}{A}\frac{\partial}{\partial r}\left(kA\frac{\partial T}{\partial r}\right) . \qquad \ldots(3)$$

The boundary conditions are given by

$$\frac{\partial T}{\partial r} = 0 \ , \text{ at } r = 0 \ , \qquad \ldots(4)$$

and

$$\frac{\sigma_1\left(T_c^{\,4} - T_s^{\,4}\right)}{1/\epsilon_c + 1/\epsilon - 1} - k\left(\frac{\partial T}{\partial r}\right)_{r=R_f} = 0 \ . \qquad \ldots(5)$$

Equation 4 is the usual center boundary condition for one-dimensional radial heat transfer in a cylinder. Equation 5 is a heat balance at the fuel surface, in which the heat radiated across the gap is equated with the heat conducted into the fuel interior.

The simultaneous solution of Equations 1 and 3 in time and space with the indicated boundary conditions is the function of the analytical model in the first calculation stage. The method by which this is accomplished is explained in Section VI.

As the cladding reaches the melting temperature (2400°F), a latent heat of fusion (133 Btu/lb) is attributed to the Hastelloy-N cladding. When this latent heat is absorbed, the entire cladding is assumed to be sheared away leaving the bare fuel-moderator material exposed to aerodynamic heating.

B. AFTER CLADDING BURNOFF

The second stage in the model calculations extends between the time of cladding burnoff and the time of initial melting at the fuel surface. This stage is by far the most important, since the greater portion of the total heat necessary to completely ablate a fuel element is herein consumed. The behavior of the fuel throughout this period can be described by heat and hydrogen continuity equations. These equations are developed considering all possible individual heat and mass transfer processes which occur within the fuel and at the fuel surface. These processes are illustrated in Figure 2b and can be listed as follows

1) Heat conduction and storage

2) Hydrogen transport under the influence of a concentration gradient

3) Heat transport due to hydrogen enthalpy redistribution

4) Thermal radiation from the fuel surface to the environment

5) Heat of hydrogen dissociation.

The resulting equations are for a uniform surface heating:

$$\rho C_p \frac{\partial T}{\partial t} = \frac{1}{A}\frac{\partial}{\partial r}\left(k A \frac{\partial T}{\partial r}\right) + \overline{C}_p D \frac{\partial N}{\partial r} \cdot \frac{\partial T}{\partial r} - H_{diss} \frac{\partial N}{\partial t} \qquad \ldots(6)$$

$$\frac{\partial N}{\partial t} = \frac{1}{A}\frac{\partial}{\partial r}\left(D A \frac{\partial N}{\partial r}\right) . \qquad \ldots(7)$$

Equation 6 is the energy equation within the fuel material. The first term on the right-hand side of the equation is the heat conduction term. The second term describes the heat transport due to hydrogen enthalpy redistribution. The last term, $H_{diss} \frac{\partial N}{\partial t}$, is an energy change due to endothermic hydrogen dissociation.

Equation 7 represents a hydrogen balance within the fuel material. The equation neglects the redistribution of hydrogen under the influence of a temperature gradient (thermal diffusion). Thermal diffusion effects were originally included in the material response model. The solutions of the resulting equations, however, demonstrated that these effects were indeed negligible under reentry conditions. A detailed discussion of the hydrogen diffusion equation is given in Appendix C.

The boundary condition necessary for the particular solution of the energy Equation 6 is given by the expression:

$$q_{net} = k\left(\frac{\partial T}{\partial r}\right)_{r=R_o} + \overline{C}_p D\left(\frac{\partial N}{\partial r} \cdot \frac{\partial T}{\partial r}\right)_{r=R_o} - q_{rad} , \qquad \ldots(8)$$

where

$$q_{net} = q_{aero} + q_{oxid} - q_{tran} + q_{comb} . \qquad \ldots(9)$$

The radiation heat loss term is:

$$q_{rad} = \epsilon \sigma_1 T_s^4 .$$

The boundary condition, $N_s = 0$ (zero surface concentration), is generally applicable to the hydrogen continuity Equation 7 in a reentry environment. For a thick oxide film on the fuel surface, this condition may not necessarily be a valid one. In a later section, it will be shown that the expected magnitude of the oxide film thickness is of the order of 1 to 4 mils. Such film thicknesses can be shown, analytically, to be ineffective in retarding the outflow of hydrogen from a rod. Nevertheless, provision is made in the model to use, as an alternative boundary condition, the equation:

$$D\left(\frac{\partial N}{\partial t}\right)_{r=R_f} - \frac{D_F N_s}{\Delta \tau_1} = 0 \qquad \ldots(10)$$

This equation is appropriate for a non-zero surface concentration, N_s, and a hydrogen permeation rate of the oxide film, $D_F N_s / \Delta \tau_1$.

When the fuel is initially exposed to aerodynamic heating, a rapid temperature rise takes place at the fuel surface. The near hydrogen-free environment adjoining the surface provides the driving force for the outflow of hydrogen. Activated by the increasing temperatures near the fuel surface, hydrogen evolution proceeds at an increasing rate. When the surface temperature reaches about 1900°F, microcracking* of the fuel material is known to occur under these rapid dehydriding conditions. The main effect of microcracking is to greatly increase the hydrogen loss rate. The mechanism of diffusion changes from atomic hydrogen diffusion through polycrystalline fuel to molecular hydrogen diffusion through microcracks. The basic hydrogen continuity Equation 7, however, is independent of the mechanism of diffusion provided that:

1) The hydrogen outflow is reasonably uniform over the fuel surface

2) An appropriate diffusion coefficient is used, pertinent to the particular mechanism and rate of diffusion.

Analytical calculations presented in this report are thus based on the assumption of uniform hydrogen outflow around the fuel surface, as well as uniform heating and temperature response. An empirical diffusion coefficient is used to describe the hydrogen diffusion through the microcracked fuel material. The derivation of this empirical diffusion coefficient from experimental data is explained in Section V.

C. FUEL ABLATION PROCESS

The third stage in the analytical description of a reentering fuel element is concerned with the fuel meltdown and ablation. In this stage, a number of simplifying assumptions were made in the analytical model:

1) A heat of fusion of 90 Btu/lb of fuel was used

2) A gradual and steady recession of the fuel surface during meltdown was simulated, as shown in Section VI

3) Aerodynamic heat flux changes due to changes in shape of the fuel were neglected

4) Oxidation heating of the fuel material during melting was assumed to be constant and equal to the oxidation heating at the melting point.

These assumptions represent an approximate approach regarding the fuel ablation process. To a certain extent, the simplified approach is justified for the uniform surface heating case because

*Microcracking is defined here to be the occurrence of infinitesimal cracks, voids or pores, grain boundary openings, or other crystal structure defects.

of the relatively small amount of additional heat necessary to completely ablate the fuel once surface melting begins. Moreover, it will be seen that reasonable correlation is attained with the available experimental data. Still, it should be noted that the simplified approach was necessitated by a lack of more specific knowledge of the heating and shearing phenomena associated with the ablation process. Investigations of these phenomena are currently being conducted at Atomics International. It is anticipated that future calculations will have the advantage of better experimental and analytical resolution of these phenomena.

IV. AERODYNAMIC HEATING AND SURFACE REACTIONS

A. AERODYNAMIC HEAT RATE

Methods of computing aerodynamic heating to reentering satellites have been previously discussed by R. D. Elliott in References 1, 2, and 4. The basic heating equations given in these references and employed in the SNAP 10A reactor reentry behavior analyses can also be applied to the calculations of the fuel element aerodynamic heating. For the fundamental definitions of the aerodynamic heating phenomena, the reader is referred to Appendix B of Reference 4.

A SNAP 10A reactor fuel element released along the reference vehicle trajectory at very high altitudes (up to 400,000 ft) will initially encounter free-molecular heating. In this regime, the total aerodynamic heat rate to the element is evaluated from the equation:

$$q_{aero} = 57.82 \times 10^{-5} \rho_A v^3 \frac{A_p}{A_s} \left(\frac{H_s - H_w}{H_s - H_{300°K}} \right) , \qquad \ldots(11)$$

where the numerical constant $= \frac{1}{2} \frac{\text{thermal accommodation coefficient}}{\text{mechanical equivalent of heat}}$.

In arriving at the constant 57.82×10^{-5} in Equation 11, a value of 0.9 was used for the thermal accommodation coefficient.[4]

At lower altitudes, 250,000 ft and below, the same fuel element will be entirely in the continuum flow regime. In this regime, the equation used to evaluate the total aerodynamic heat rate to the element is:

$$q_{aero} = q_{ref} F_Q \frac{1}{\sqrt{2 R_o}} \left(\frac{H_s - H_w}{H_s - H_{300°K}} \right) , \qquad \ldots(12)$$

where .

$$q_{ref} = 865 \left(\frac{\rho_A}{\rho_{s1}} \right)^{1/2} \left(\frac{v}{10^4} \right)^{3.15} \qquad (\text{Btu/ft}^2 - \text{sec}) .$$

The reference heat rate, q_{ref}, is defined as the heating rate at the stagnation point of a cold (300°K) spherical body having a 1-ft radius. The expression, in which the reference heat rate is related to the air density and the element velocity, is based on the work of Fay and Riddell[11] and the subsequent correlations by Kemp and Riddell[12] and by Detra and Hidalgo.[13]

Equation 12 is developed from the reference heat rate considering the fuel element geometry, flight orientation, and surface temperature. The cold wall heating rate along the stagnation line of a cylinder of radius R_o, q_{cyl}, is related to the reference heat rate by the expression:

$$q_{cyl} = \frac{\sqrt{1 \text{ ft}}}{\sqrt{2R_o}} \cdot q_{ref} . \qquad \ldots(13)$$

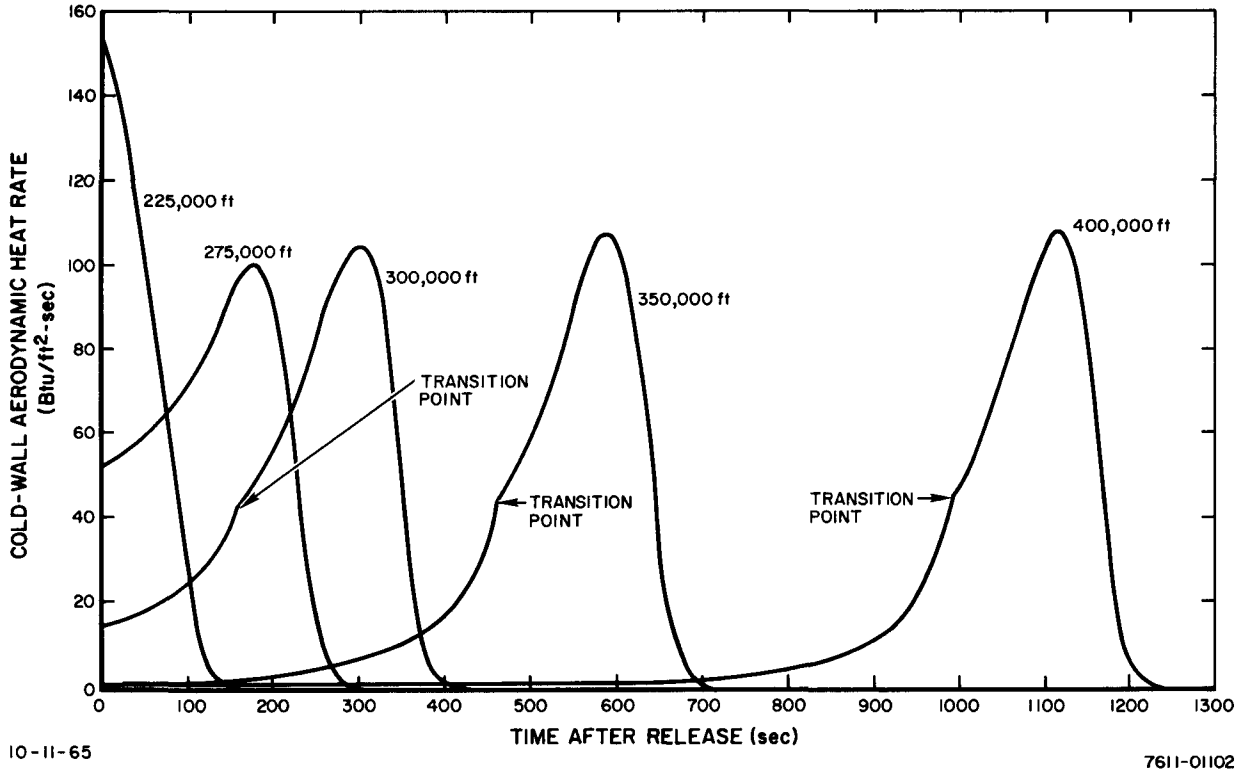

Figure 3. Average Cold-Wall Aerodynamic Heat Rate to a SNAP 10A Fuel Element Spinning Cross-Axially vs Time After Release From Various Altitudes

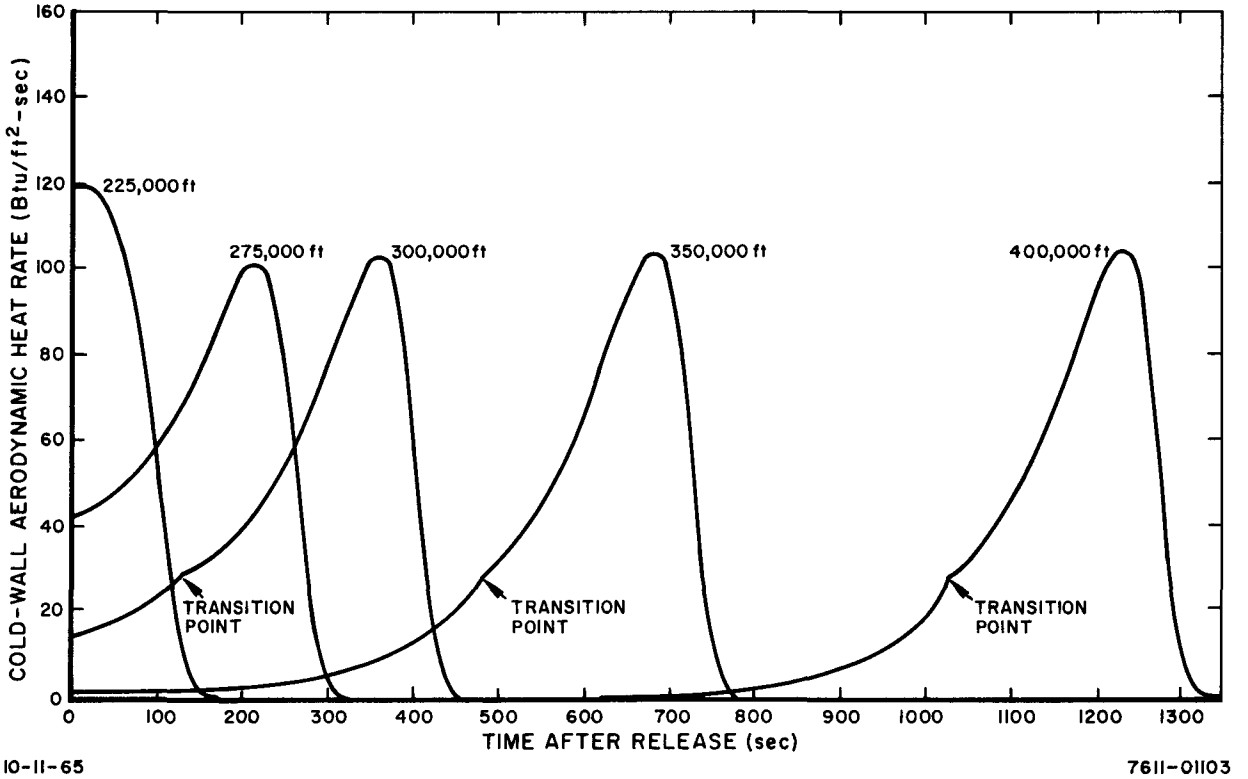

Figure 4. Average Cold-Wall Aerodynamic Heat Rate to a SNAP 10A Fuel Element Tumbling at Random vs Time After Release From Various Altitudes

For a rotating or tumbling fuel element for which the aerodynamic heating is uniformly distributed around the surface, the average heat flux (per unit surface area) in the continuum regime is

$$\bar{q}_{cyl} = F_Q q_{cyl} \quad q_{ref} \cdot \frac{F_Q}{\sqrt{2R_o}} \quad . \qquad \ldots(14)$$

Values of the average heating to the stagnation-line heating ratio, F_Q, have been given in Reference 1 for the three flight orientations which effect uniform surface heating. These values are as follows

F_Q - 0.36 for stable cross-axial spinning

= 0.28 for random tumbling

= 0.22 for end-over-end tumbling.

Transition from free-molecular to continuum heating occurs, for a SNAP 10A fuel element, over an altitude range centered around 285,000 ft. The computations in this report are based upon a sharp transition from free-molecular heating to continuum heating at the point where the two heating curves intersect (at about 285,000 ft).

The reference heating rates were evaluated as a function of time after release using the trajectory digital code, RESTORE, developed at Atomics International. This code represents the reentering body by a point-mass sphere with a given drag coefficient and a projected area. This drag coefficient may be constant, or may vary with the Knudsen number. The code integrates the equations of motion relative to a rotating, oblate earth. From the calculated values of the velocity and the air density, the code computes, at each time step, a reference free-molecular heating rate,

$$q_{fm} = 57.82 \times 10^{-5} \rho_A \cdot v^3 \quad , \qquad \ldots(15)$$

a continuum reference heating rate, q_{ref}, and H_s, the enthalpy level of the air in the stagnation region (Btu/lb). Using these quantities, the heat rate input to the fuel element at any time can then be specified by the expression

$$q_{aero} = \frac{1}{A_s} \cdot \text{Min}\left(q_{fm} A_p, \bar{q}_{cyl} \cdot A_s\right)\left(\frac{H_s - H_w}{H_s - H_{300°K}}\right) \quad . \qquad \ldots(16)$$

For selected fuel element release altitudes and for each assumed flight orientation, RESTORE calculations were performed to provide the information needed by the analytical model to evaluate the aerodynamic heating. Tables of the cold wall heat rate, $1/A_s \cdot \text{Min}\,(q_{fm} A_p, \bar{q}_{cyl} \cdot A_s)$, and of the stagnation enthalpy were formulated from the RESTORE output as functions of time after release. These tables were then used as input to the analytical model. At each iteration in the material response calculations, Equation 16 was evaluated by the analytical model according to these tables and according to the surface temperature (or wall enthalpy, H_w) of the fuel element.

Plots of the RESTORE-calculated, cold-wall heat flux transients are shown in Figures 3 and 4 for selected fuel element release altitudes. The corresponding air stagnation enthalpy transients

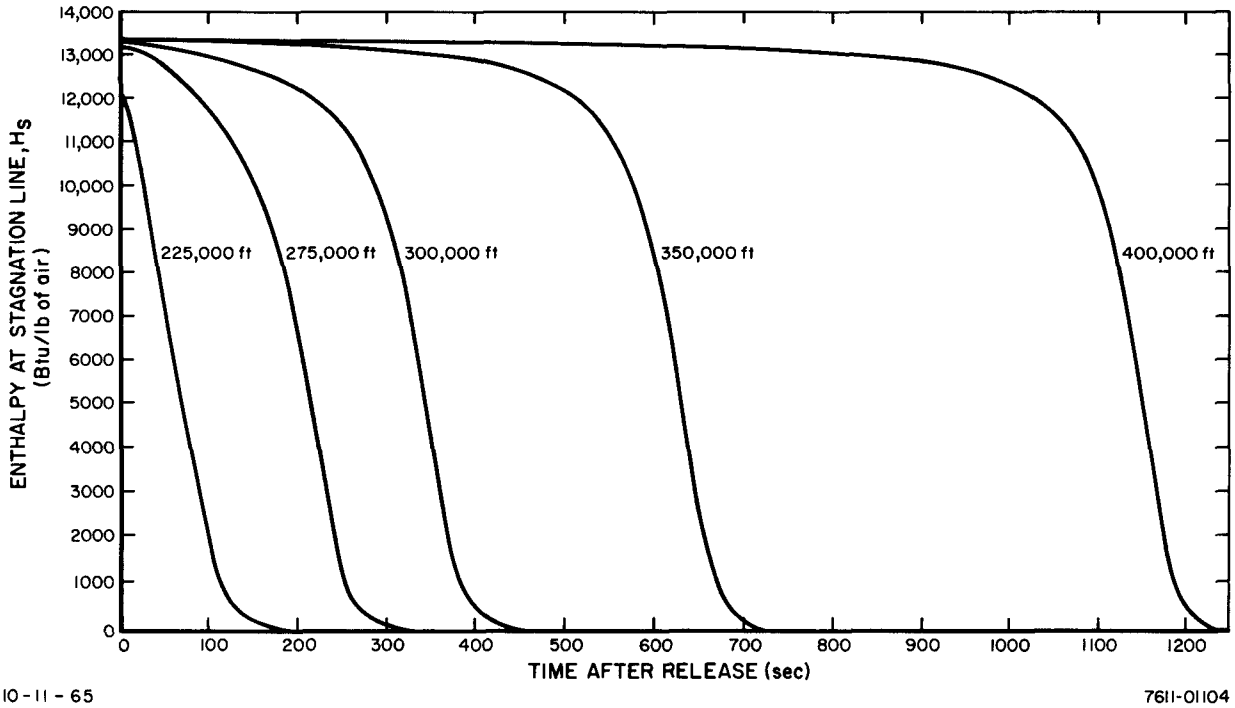

Figure 5. Air Enthalpy at the Stagnation Line of a SNAP 10A Fuel Element Spinning Cross-Axially vs Time After Release From Various Altitudes

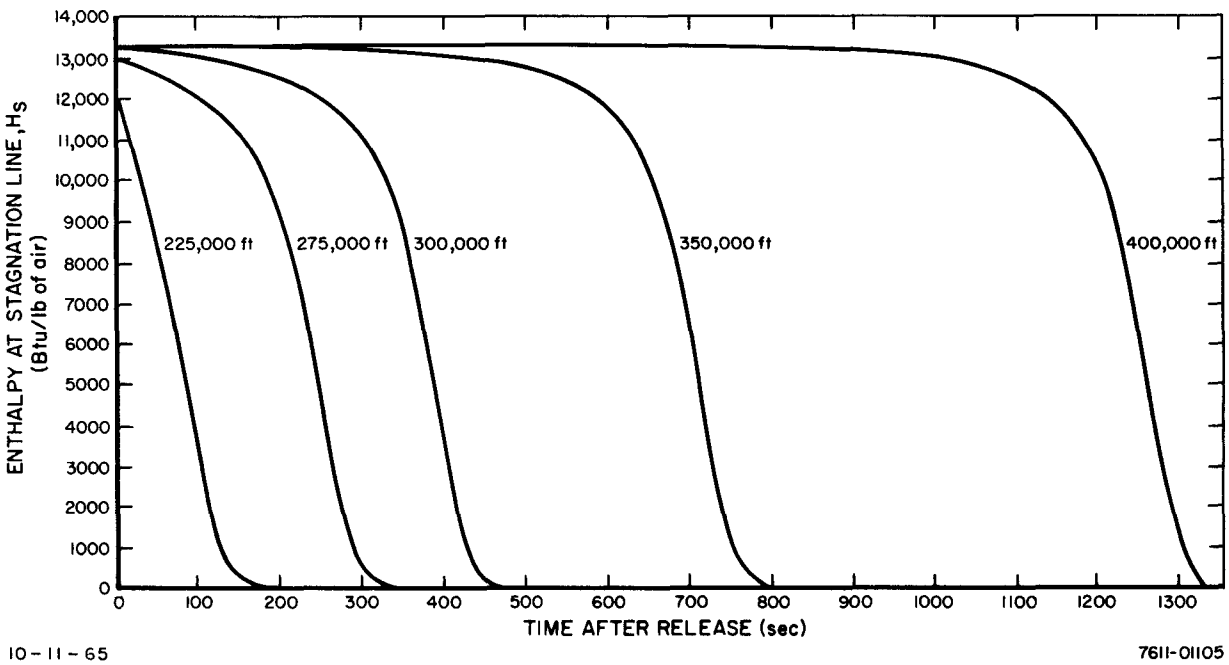

Figure 6. Air Enthalpy at the Stagnation Line of a SNAP 10A Fuel Element Tumbling at Random vs Time After Release From Various Altitudes

are shown in Figures 5 and 6. In Figures 3 and 4, changes in the shapes of the curves at the lower release altitudes are immediately evident. The integrated heating under these curves has been evaluated up to the time at which $\bar{q}_{cyl}$ equals 52 Btu/ft^2-sec. A plot of this integrated cold-wall heat flux, Q_{avail}, is included in Section VIII as a function of release altitude. The integration cutoff point at 52 Btu/ft^2-sec was chosen since this is the point at which q_{aero} equals the radiation heat loss of the fuel at the melting temperature.

In obtaining these fuel element trajectory transients, it was necessary to provide as input, to the RESTORE code, values of the ballistic coefficient, $W/C_D A_P$. The total weight, W, of a SNAP fuel element is 3.42 lb. The drag coefficients for the cylindrical elements were determined from data presented in Reference 14, which discusses cylinder drag near the transition region. The drag coefficient, C_D, was found to be highly dependent on the Knudsen number at altitudes corresponding to the transition region. Near the continuum flow regime, however, the drag coefficient becomes relatively constant at high Mach numbers. Thus, for release altitudes around 250,000 ft and below, constant, average ballistic coefficients were used in the RESTORE computations. Details of the calculations of these ballistic coefficient values are given in Appendix A. Values of these constant ballistic coefficients, along with the corresponding average values of $C_D \cdot A_P$ are given in Table 1 for different flight orientations.

TABLE 1

SNAP 10A FUEL ELEMENT BALLISTIC COEFFICIENTS IN CONTINUUM FLOW

Flight Orientation	Average $C_D A_P$ (ft^2)	$W/C_D A_P$ (lb/ft^2)
Cross-axial spinning	0.1674	20
End-over-end tumbling	0.0781	44
Random tumbling	0.1025	34

For release altitudes above 250,000 ft, variable ballistic coefficients were used in the RESTORE computations. These ballistic coefficients were based on drag coefficients varying with the Knudsen number according to the data obtained from Reference 14 (see Appendix A). At higher altitudes, the ballistic coefficients are lower than those given in Table 1. At 400,000 ft, the values are 11.12, 24.81, and 18.48, respectively, for cross-axial spinning, end-over-end tumbling, and random-tumbling flight orientations.

B. OXIDATION

After the fuel element cladding ablates away during reentry, a heat release due to oxidation of the zirconium-uranium hydride fuel augments the aerodynamic heat flux at the fuel surface. A study of this oxidation was undertaken to determine the magnitude of the oxidation heating contribution. In addition, the amount of oxide film buildup is of interest since these oxide layers could, conceivably, inhibit hydrogen evolution as well as affect the catalytic efficiency of the fuel surface.

Various sets of experimental data are available in the literature regarding the oxidation reaction rate constants for pure zirconium metal exposed to dry oxygen atmospheres. Some investigators fitted their data to a parabolic rate law and some fitted their data to a cubic rate law. It is important to note, however, that, in all of these experiments, data were obtained at low or intermediate temperatures.

Cubicciotti,[15] in 1958, determined the reaction kinetics of zirconium metal in oxygen pressures from 1 to 200 torr over a temperature range from 600 to 920°C (110 to 1690°F). Cubicciotti's data followed the parabolic rate law. The temperature dependence of the reaction rate constants was found to follow the equation:

$$K_p = 2400 \exp\left(\frac{-32,000}{RT}\right) , \qquad \ldots(17)$$

where K_p represents the reaction rate constants (mg^2/cm^4-sec) for a parabolic rate law. The oxidation rates were not affected by changing the oxygen pressure from 1 to 200 torr. A plot of these rate constants as a function of inverse temperature is shown in Figure 7.

Cubicciotti's data were initially used as a basis for computing the oxidation heating rate to a re-entering fuel element. The underlying uncertainties in using these data were duly recognized and can be listed as follows:

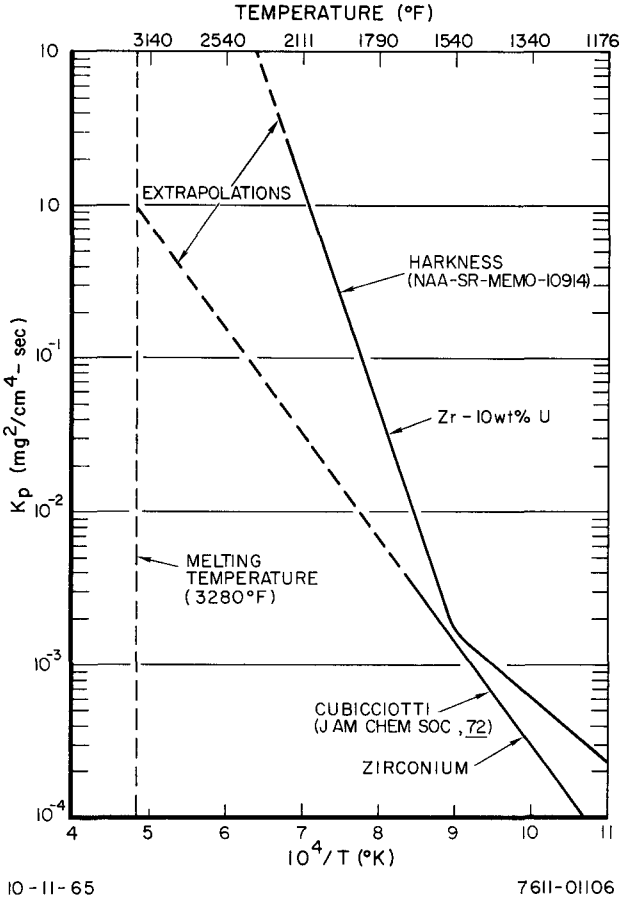

Figure 7. Parabolic Oxidation Rate Constants vs Reciprocal Temperatures

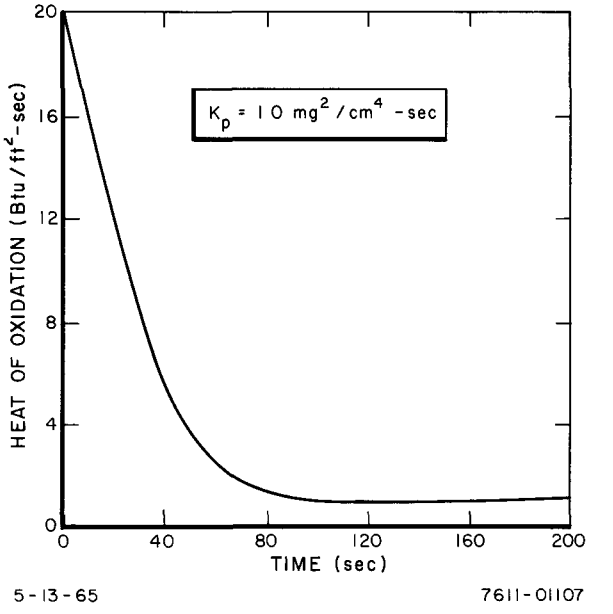

Figure 8. Oxidation Heating Rate vs Time Based on Parabolic Oxidation With a Constant Reaction Rate Constant

1) Oxidation rate data for the fuel material were based on those of zirconium metal.

2) The oxide layer formed under reentry conditions was assumed similar to the layer formed under static conditions.

3) The influence of hydrogen outgassing on oxide formation was not considered.

In view of these uncertainties, it was felt that the use of a temperature-dependent K_p (given by Equation 17) was probably not warranted. In the actual calculations, a constant value for K_p was used which (it was felt) would give maximum oxidation heating rates. This constant value was obtained by evaluating Equation 17 at the melting temperature of the fuel. The resulting calculated heat of oxidation was found to be small — about 5% of the total heat necessary to initiate melting of the fuel. The time behavior of this calculated heating is shown in Figure 8. This heating is invariant for all reentry and arc-jet calculations, since a temperature-independent kinetics rate constant was used.

In the above calculation of the oxidation heating, it was assumed that the sluggishness of the chemical kinetics controls the overall oxidation process. This is true if the heat calculated for the complete reaction of all oxygen diffusing to the fuel surface is always greater than that calculated using the kinetic reaction rate constants. For the reaction rate constants given by Cubicciotti, it can be shown that this is indeed the case during reentry.

Recently, parabolic oxidation reaction rate constants for unhydrided, modified SNAP fuel material exposed to air and oxygen atmospheres were determined by Harkness at Atomics International.[16] These rate constants, measured up to a maximum temperature of 1200°C (2200°F), are shown as a function of inverse temperature in Figure 7. Note the strong increase in K_p for temperatures above 840°C (1544°F). The discontinuity in the slope of the line at 840°C indicates a change in the mechanism of oxidation. It has been postulated that this change is caused by the increasing importance of oxygen diffusion into t e metal lattice. This effect would limit the oxide film buildup and increase the overall oxygen uptake.

According to these new data, the oxidation of the (unhydrided) fuel proceeds at much faster rates at higher temperatures than that initially calculated using the rate data of Cubicciotti. At temperatures approaching the fuel melting point, the heat calculated for the complete reaction of all oxygen diffusing to the fuel surface becomes less than that calculated using the kinetic reaction rate constants of Harkness. At these temperatures, therefore, one may assume an instantaneous kinetic reaction rate and consider only the oxygen flux supplied to the fuel surface.

The heating rate due to oxidation of the fuel material can be calculated by the general expression

$$q_{oxid} = \Delta H_{oxid} \cdot \frac{dm}{dt} \quad , \qquad \ldots(18)$$

where

q_{oxid} = heat release rate due to oxidation (Btu/ft^2-sec),

ΔH_{oxid} = heat of reaction (Btu/lb of O_2),

$\frac{dm}{dt}$ = mass rate of reacting oxygen (lb of O_2/ft^2-sec).

For the chemical reaction,

$$Zr + O_2 \rightarrow ZrO_2 \quad ,$$

the literature value[17] of the heat of reaction (ΔH_{oxid}) is 260 kcal/mole or 14,625 Btu/lb of O_2.

In order to apply Equation 18, the mass rate of reacting oxygen, dm/dt, must be expressed in terms of known quantities. If the reaction is kinetics controlled, dm/dt must be expressed in terms of the kinetic rate constants. If the reaction is limited by the supply of oxygen to the reaction zone, dm/dt must be expressed in terms of the oxygen flux diffusing through the boundary layer.

1. Oxidation Heat Rate for a Kinetics-Controlled Reaction

The basic law, which leads to parabolic oxidation at constant temperatures, can be written:

$$\frac{dm}{dt} = \frac{K_p}{2m} \quad , \qquad \ldots(19)$$

where m is the mass of reacted oxygen. The values of m can be evaluated at any time through integration of Equation 19:

$$\int_{m=0}^{m} 2\, m\, dm = \int_{t=0}^{t} K_p\, dt \quad , \qquad \ldots(20)$$

$$m = \left(\int_{t=0}^{t} K_p\, dt\right)^{1/2} \quad . \qquad \ldots(21)$$

Substituting this expression into Equation 19, one gets:

$$\frac{dm}{dt} = \frac{K_p}{2\left(\int_{t=0}^{t} K_p\, dt\right)^{1/2}} \quad . \qquad \ldots(22)$$

Using Equation 22, Equation 18 can then be expressed as:

$$q_{oxid} = \Delta H_{oxid} \frac{K_p}{2\left(\int_{t=0}^{t} K_p\, dt\right)^{1/2}} \quad . \qquad \ldots(23)$$

Equation 23 is a usable expression with which one can calculate the oxidation heat rate for a kinetics-controlled reaction with known rate constants and a known surface temperature behavior.

2. Oxidation Heat Rate for an Oxygen-Supply-Limited Reaction

The analysis of the diffusion of oxygen through the boundary layer can be simplified by utilizing an analogy between heat and mass transfer. This approach is based on the assumption that the oxygen molecular diffusivity is equal to the diffusivity of heat across the boundary layer; i.e., that $D_O = \alpha_A$.

The aerodynamic heat flux relationship at the stagnation point can be simplified to the form:

$$q_{stag} = F_s \cdot h(T_s - T_w) \quad ,$$

where

$$q_{stag} = q_{ref}\left(\frac{H_s - H_w}{H_s - H_{300°K}}\right) \qquad (Btu/ft^2\text{-sec}) \quad .$$

This equation can also be written

$$q_{stag} = F_s \cdot \alpha_A \rho_A (H_s - H_w) \quad . \qquad \ldots(24)$$

The molecular flux of oxygen diffusing through the boundary layer at the stagnation point can be given by a similar expression

$$J_O = D_O \cdot F_s \quad (C_s - C_w) \quad ,$$

where D_O is the diffusivity of the oxygen. If all of the oxygen reaching the fuel element surface reacts at the surface, then C_w can be set equal to zero. Also, since the mass fraction of oxygen in air is 0.2, the concentration of oxygen at the stagnation point, C_s, can be given as $0.2\ \rho_A$. Then,

$$J_O = \frac{0.2\ q_{stag}}{H_s - H_w} \quad . \qquad \ldots(25)$$

If q_{aero} is the average heat flux to the fuel element surface, then the average oxygen flux to the surface is

$$\overline{J}_O = \frac{0.2\ q_{aero}}{H_s - H_w} \quad . \qquad \ldots(26)$$

Under the assumption of an instantaneous chemical reaction rate, the mass rate of reacting oxygen can be set equal to the oxygen flux reaching the surface,

$$\frac{dm}{dt} = \overline{J}_O = \frac{0.2\ q_{aero}}{H_s - H_w} \quad . \qquad \ldots(27)$$

Finally, the heating rate for an oxygen-supply-limited reaction is obtained by combining Equations 18 and 27

$$q_{oxid} - H_{oxid}\left(\frac{0.2\ q_{aero}}{H_s - H_w}\right) \quad . \qquad \ldots(28)$$

In the preceding development, expressions (Equations 23 and 28) have been derived with which the heating contribution of fuel material oxidation can be evaluated throughout reentry. The heating contribution is always taken to be the lesser of the respective heats calculated by Equations 23 and 28. A typical calculation is shown as a function of time after release from 260,000 ft in Figure 9. In this calculation, the oxidation mechanism transfers from a kinetics-controlled to an oxygen-supply-limited reaction when the surface temperature reaches about 2600°F. The integrated

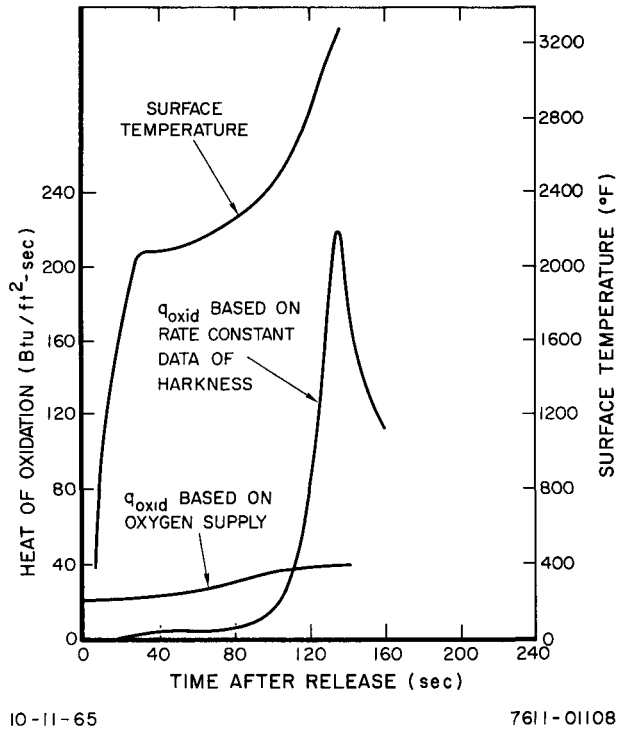

Figure 9. Oxidation Heating Rate as a Function of Time for a Release Altitude of 260,000 ft

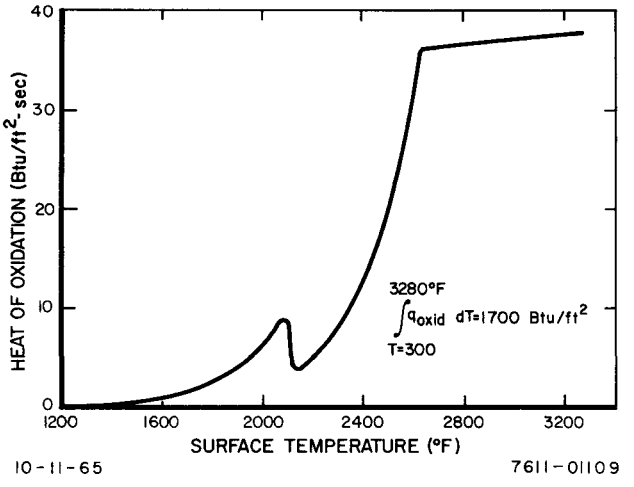

Figure 10. Heat of Oxidation as a Function of Fuel Surface Temperature

oxidation heating contribution up to melting is about 1700 Btu/ft^2, taking the lesser of the two computed heating rates at all times.

Similar calculations made for different release altitudes result in analogous behavior of the oxidation heating rate, if one plots the minimum q_{oxid} as a function of surface temperature. This behavior is shown in Figure 10. The small dip in this curve at about 2100°F is caused by the very slow rise in temperature at that time.

In the analytical description, this oxidation heating curve may then be used for any release altitude or heating rate within the ranges of interest in this study. Although this heating curve represents the best data available to date, it is still based on rate constants obtained under static conditions without the presence of hydrogen outflow. Laboratory experiments are presently being undertaken at Atomics International in which oxidation weight gains are to be measured under simulated transient reentry conditions.

Under the assumption that all of the reacting oxygen contributes to the buildup of an oxide film, the thickness of this film can be computed through integration of Equation 18. Using the heating rates given in Figure 10, these oxide film thicknesses during the period of rapid hydrogen evolution (2000 to 2500°F) are calculated to be from about 1 to 4 mils.

C. TRANSPIRATION COOLING

The flow of hydrogen out of the fuel element occurring simultaneously with heat transfer to the fuel element surface produces an effect known as transpiration cooling. Actually, this effect is twofold, and is characterized by the following processes:

1) The relatively cool hydrogen gas is injected into the boundary layer with an ensuing chilling effect.

2) The boundary layer becomes thickened, resulting in added resistance to heat transfer across the boundary layer.

The theory and the experimental aspects of transpiration cooling have been studied by Bethe and Adams,[18] by Georgiev,[19] and by others. According to the development given in these references, the transpiration cooling effect is approximately described by the expression,

$$\psi = 1 - 0.60\, M^{0.26} (H_s - H_w) \cdot \frac{J_H}{q_{stag}} , \qquad \ldots(29)$$

where

ψ = the ratio of the amount of heat (at the stagnation line) which actually can get to the surface with transpiration to the amount of heat without transpiration ($0 < \psi < 1$).

From Equation 29, the average (over the fuel surface) heating blocked due to transpiration cooling can be defined as:

$$q_{tran} = 1.2\, F_Q (H_s - H_w) \left(D \frac{dN}{dr}\right)_{r=R_f} , \qquad \ldots(30)$$

where the factor, F_Q, was included to average the heating around the surface and the substitution,

$$J_H = \left(D \frac{dN}{dr}\right)_{r=R_f} ,$$

was made. Equation 30 is used, in the analytical model, to evaluate the transpiration cooling reduction at each calculation iteration.

D. HYDROGEN COMBUSTION

As the hydrogen gas is injected into the high-temperature boundary layer, it will react with oxygen. The heat release due to the reaction,

$$H_2 + 1/2\, O_2 \rightarrow H_2O ,$$

can be evaluated by considering the chemical kinetics and the supply of the reactants to the reaction zone. In order for the combustion reaction to be pertinent, hydrogen must react in the boundary layer or behind the shock. The reaction time is on the order of 10^{-6} sec, according to Fowler.[20] Thus, using a detachment distance (10% of the fuel radius) of 6.25×10^{-2} in. and a reaction time of 10^{-6} sec, the hydrogen injection rate must be greater than 5×10^3 ft/sec before it can escape into the free stream outside the shock without reacting with oxygen. The high velocity of 5×10^3 ft/sec is unlikely or impossible for the process being considered.

For the analytical model, the fraction of completion for the foregoing reaction is evaluated as a function of time after rod release. This is done by using the atmospheric pressure and the

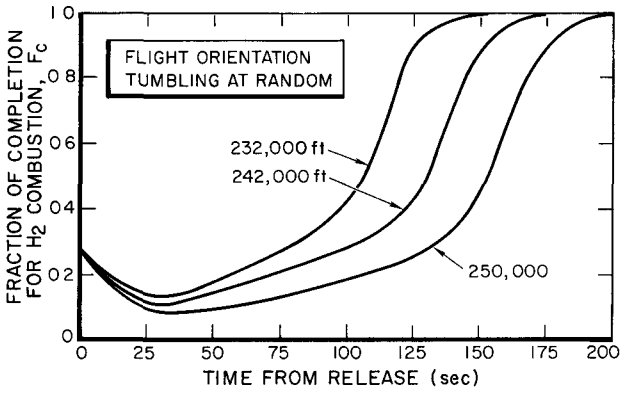

Figure 11. F_c as a Function of Time After Release From Various Altitudes

temperature behind the shock, obtained from the fuel element trajectory (RESTORE) computations. With these quantities, the fraction of completion can be evaluated from known temperature-pressure dependent reaction rates. Typical fractions of completion are presented in Figure 11 for different release altitudes. Because of the relatively high temperature behind the shock immediately following fuel element release, the combustion of hydrogen does not proceed to a great extent. The combustion proceeds to a higher fractional completion at the last portion of the reentry trajectory where the aerodynamic heating becomes small.

The heat release due to hydrogen combustion is proportional to the product of the fraction completion, F_c, and the average mass flux of the limiting reactant, $\overline{J}_O$ or $\overline{J}_H$, according to the expression,

$$q_{comb} = \Delta H_{comb} \overline{J}_{O/H} \cdot F_c \quad . \qquad \ldots(31)$$

Both hydrogen and oxygen must be considered as the limiting reactant during reentry.

If hydrogen is the limiting reactant, then,

$$q_{comb} = \Delta H_{comb} \left(D \frac{dN}{dr} \right)_{r=R_f} \cdot F_c \quad , \qquad \ldots(32)$$

where $\Delta H_{comb} = 5.2 \times 10^4$ Btu/lb of H_2.

If oxygen is the limiting reactant, then, using Equation 26,

$$q_{comb} = \Delta H_{comb} \frac{0.2\, q_{aero}}{H_s - H_w} F_c \quad , \qquad \ldots(33)$$

where $\Delta H_{comb} = 6.5 \times 10^3$ Btu/lb of O_2.

The heating rate due to hydrogen combustion used in the analytical process is always taken to be the lower of the two values obtained from Equations 32 and 33. The total contribution of the combustion of hydrogen toward the heating of the fuel element is calculated to be less than 10%, for all release altitudes considered. The characteristic transient behavior of the calculated heat of combustion is shown in Figure 12, for a sample reentry solution, and compared to the corresponding heat of oxidation (assuming a constant $K_p = 1.0$ mg^2/cm^4-sec) and the heat rate losses due to transpiration cooling and radiation.

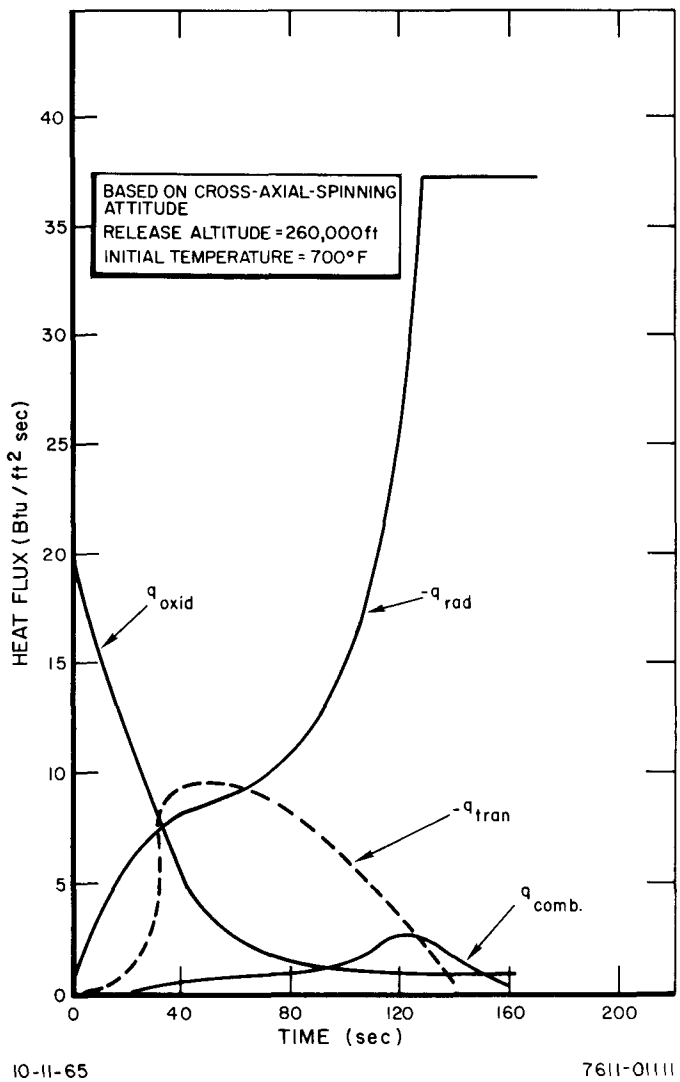

Figure 12. Comparison of Fuel Surface Heating Contributions During Reentry

V. FUEL ELEMENT MATERIAL PROPERTIES

A. ZIRCONIUM-URANIUM HYDRIDE FUEL

In this section, available data on the thermophysical properties of SNAP fuel material are analyzed and evaluated for the purpose of arriving at a best or standard set of values for reentry conditions. A complete listing of this standard set of parameter values is given in Section VIII-C.

As a preliminary step for this evaluation, a comprehensive survey, reviewing all investigations conducted on zirconium hydride and zirconium-uranium hydride systems, was made under the direction of the SNAP Aerospace Nuclear Safety Program. Abstracts of publications pertaining to the subject were compiled and categorized in the form of a bibliographical survey and published separately.[21] Unclassified publications were included in Volume I of this document while the classified reports were included in Volume II. These abstracts served as source information for the material property evaluation which follows.

1. Phase Diagram

SNAP fuel material has three main constituents: zirconium, uranium, and hydrogen. During fabrication of the fuel elements, long cylinders of zirconium - 10 wt % uranium alloy are first formed. These cylinders are then slowly hydrided under closely controlled conditions until the desired final composition is attained. The absorbed hydrogen forms a thermodynamic solution with the zirconium with the consequent separation of minute, inert uranium particles dispersed throughout the matrix. This interpretation is supported by the work of La Grange, et al.,[22] who showed that the microstructures of the ternary Zr-U-H system are analogous to those of the Zr-H binary system. The P-C-T studies of Atkins,[23] Toy and Vetrano,[24] and the P-C-T and x-ray diffraction studies of Bigony, et al.,[25] and Singleton, et al.,[26] provide further substantiation. As a consequence, the phase characteristics of SNAP fuel material may be inferred from those of the binary Zr-H system.

The Zr-H constitutional diagram used for the fuel element burnup studies is shown in Figure 13. The basic phase structure of this diagram was obtained from a diagram suggested by Douglas in Reference 27. His suggested diagram represents a composite interpretation of the results of many independent phase studies, including his own. Douglas' delta-beta+delta phase boundary was extended, in Figure 13, to higher temperatures using the P-C-T data of Atkins.[23] The two sets of data joined smoothly at common temperatures. At the present time, it is thought that this resulting constitutional diagram most accurately portrays the phase characteristics of SNAP fuel material.

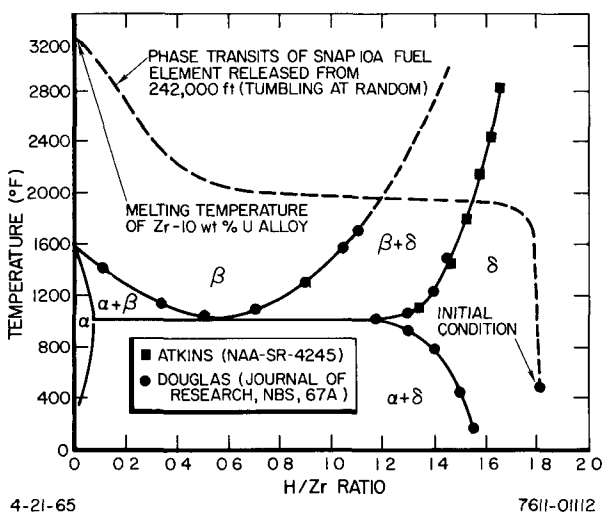

Figure 13. Zirconium-Hydrogen Phase Diagram

Representative phase transits of the fuel material calculated by means of the analytical model during reentry are shown by the dashed line in Figure 13. Plotted here is the changing average

temperature and hydrogen content of a SNAP 10A fuel element under typical reentry conditions. One is guided along the sequence of events leading to fuel melting by following the dashed line upwards from the indicated initial (time = 0) point. As the temperature rises, the hydrogen loss, initially lethargic, increases rapidly as the temperature reaches about 1900°F (1040°C). A change of phase occurs at around 2000°F after which the average temperature remains near-constant and the width of the beta phase is traversed. At low hydrogen concentrations, the temperature rises sharply to the melting point. No points of discontinuity are seen at the phase boundaries since the phase changes occur gradually across the radius of the fuel. Such phase boundary discontinuities are evident in plots of local temperature vs local hydrogen content.

Each nodal segment in the fuel material is programmed to change phase according to the constitutional diagram and the temperature and the H/Zr ratio of the segment. This implies an instantaneous phase transformation rate. In regard to this, the electrical pulse-heating tests of Taylor and Finch et al.[28, 29, 30] indicated that complete and rapid crossing of the beta+delta, two-phase region could be made without any noticeable phase transformation time lag. For the slower transient conditions of reentry, this same phenomena should manifest itself.

The material phase of each nodal segment is determined by inputing, to the analytical model, tables of the beta+delta phase boundaries and comparing, at each time step, the boundary H/Zr ratios with the corresponding nodal H/Zr ratios for the particular nodal temperature (see phase diagram, Figure 13). The difference between the nodal H/Zr ratio and the beta-beta+delta boundary H/Zr ratio is defined by the variable, a. Likewise, the variable, b, is defined as the difference between the nodal H/Zr ratio and the delta-beta+delta boundary H/Zr ratio. Phase mass fractions for each nodal segment were then computed at each time step according to the Lever Arm Principle of the phase diagram. Thus,

$$\left.\begin{aligned} M_{\delta} &= \frac{a}{a+b} \\ M_{\beta} &= \frac{b}{a+b} \end{aligned}\right\} \text{ in the beta + delta two-phase mixture}$$

$$\left.\begin{aligned} M_{\delta} &= 0 \\ M_{\beta} &= 1 \end{aligned}\right\} \text{ in the all beta phase, and}$$

$$\left.\begin{aligned} M_{\delta} &= 1 \\ M_{\beta} &= 0 \end{aligned}\right\} \text{ in the delta-epsilon phase region.}$$

2. Melting Temperature and Heat of Fusion

Pure zirconium metal melts at 1857°C (3375°F) with a latent heat of 53.7 cal/gm (96.6 Btu/lb).[17] Uranium metal is known to melt at 1133°C (2071°F) with a latent heat of 12.6 cal/gm (22.7 Btu/lb).[17] Weighing these latent heats appropriately, one obtains about 50 cal/gm (90 Btu/lb) for the theoretical heat of fusion of Zr - 10 wt % U alloy. This value is in fair agreement with the measured latent heat value of 56.5 cal/gm reported in Reference 31.

The melting temperature of Zr - 10 wt % U alloy can be obtained from the Zr-U constitutional diagram given in Reference 32. At 10 wt % uranium content, the melting temperature of the alloy is

1805°C (3280°F). In a recent report,[33] Battelle reported a solidus melting temperature of 1810 ±25°C for the alloy. Also, in this latter report, it was noted that the presence of dissolved oxygen markedly increases the melting temperature. This unfavorable effect creates additional uncertainty in the melting temperature of the alloy in an oxygen atmosphere.

Post-test microstructural analyses performed for both the experimental arc-jet tests and the electrical pulse-heating tests indicate that a fuel segment becomes essentially devoid of hydrogen before the segment melts.[9, 28, 29, 30] Analytical calculations using the standard set of parameter values are characterized by this same behavior. Accordingly, the melting temperature and heat of fusion for the fuel material can be taken to be that for unhydrided Zr-10 wt % U alloy. Thus, in the standard set of parameter values, a heat of fusion of 90 Btu/lb is used for the fuel material while the melting temperature is taken to be 3280°F.

3. Specific Heat

In order to provide the necessary input information for the analytical model, the available data on the specific heat of zirconium hydride and of zirconium-uranium hydride were evaluated. Generally, the existing data are characterized by noticeable variation with both temperature and hydrogen content. For some of the data, the derivation of empirical relationships which adequately describe the bivariate dependence was possible. Each such relationship was necessarily confined within the appropriate material phase; the expressions were found to change drastically from phase to phase.

For fuel element reentry calculations, three phase regions are of interest: the delta-epsilon phase region, the beta phase, and the beta+delta two-phase region. At the time of fuel element release, the fuel material is completely delta or epsilon phase material. A temperature rise of about 1700°F ensues, in the typical case, until a material phase change is encountered. Throughout this initial temperature rise, the following expression is used for the fuel specific heat in the standard set of parameters:

$$(C_p)_{\delta,\epsilon} = 0.1\ (H/Zr - 1.073) + 0.711 \times 10^{-4} \times T\ °F\ (Btu/lb-°F)\ . \qquad ...(34)$$

Equation 34 is an empirical relationship derived from data presented in References 31, 34, and 35. These data were obtained using the well known electrical pulse-heating technique[28, 29, 30] for actual modified SNAP fuel samples of delta or epsilon phase composition. Measurements were made over a temperature range from room temperature to 1100°F. Because of the rapid heating rates and the moderately low temperatures, the measurements were unblemished by hydrogen evolution effects. Considering both the experimental method and the degree to which the data fit the empirical expression, specific heat values calculated by Equation 34 should be accurate to within about 10%. Actually, values calculated for temperatures greater than 1100°F may be subject to a wider error range.

Reported results of other investigations on the delta or epsilon phase specific heat for both zirconium hydride can be found in the literature. Abstracts of these reports can be found by means of the Subject Index of Reference 21 under heat, specific. Some comparisons and discussion of the various experimental results are given by Taylor and Ambrose in Reference 34. General trends in the various sets of data are not always consistent. This is particularly true for the higher temperature data. Often, however, causes for the discrepancies could be attributed to the experimental methods and procedures used.

Reliable experimental determinations of the beta phase specific heat for actual fuel material have not been reported to date. For zirconium hydride, the beta phase specific heat was found by Douglas and Victor[36] to be independent of temperature but strongly dependent on hydrogen content. Their experimental method of measurement was based on a Bunsen ice calorimeter. The resulting data can be fitted to the equation,

$$(C_p)_\beta = 0.085 + 0.05\ H/Zr\ \text{Btu/lb-°F} \quad . \qquad \ldots(35)$$

From this expression, the beta phase specific heat equation for the actual fuel material can be derived by accounting for the presence of 10 wt % uranium. Assuming a specific heat value of 0.0393 Btu/lb-°F for the uranium,[17] one gets, for the fuel material,

$$(C_p)_\beta = 0.9(0.085 + 0.05\ H/Zr) + 0.1(0.0393)\ \text{Btu/lb-°F}$$

or

$$(C_p)_\beta = 0.045(1.787 + H/Zr)\ \text{Btu/lb-°F} \quad . \qquad \ldots(36)$$

Equation 36 is used to calculate the beta phase fuel specific heat in the standard set of parameter values.

Within the beta+delta, two-phase region, the fuel specific heat is calculated within the analytical model according to the expression,

$$(C_p)_{\beta+\delta} = (C_p \cdot M_F)_\beta + (C_p \cdot M_F)_\delta \ , \qquad \ldots(37)$$

where M_F is the phase mass fraction according to the phase diagram. For typical reentry calculations, very little heat is stored as the fuel material passes through the beta+delta, two-phase region. A typical plot of the fuel specific heat as a function of temperature during reentry heating is shown in Figure 14.

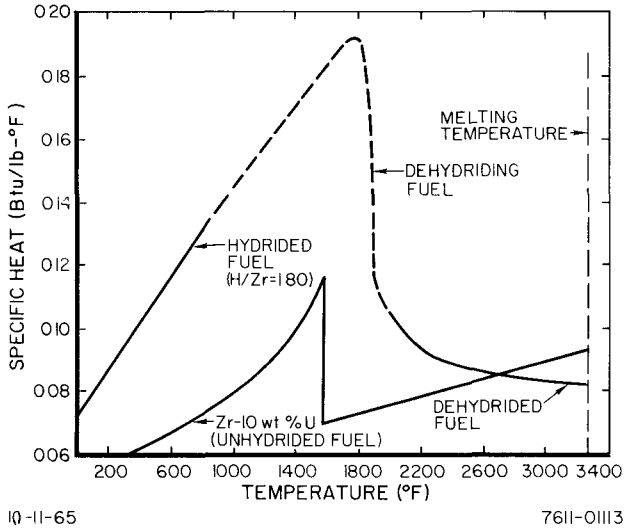

Figure 14. Specific Heat of Fuel Material as a Function of Temperature

4. Heat of Dissociation

When hydrogen gas dissolves in zirconium metal, a quantity of heat, the partial molar heat of solution, is evolved. In the opposite reaction, the hydrogen dissociates from the mixture with a consequent heat absorption of equal magnitude. In using the term "dissociation" for this latter reaction, it is understood that the metal-gas system is merely a solution,[37, 38] whether ideal or non-ideal, and that the so-called dissociation is given by the equation,[39]

$$2H\ (\text{dissolved in Zr}) \rightarrow H_2\ (\text{gas}) \quad .$$

The heat of solution or dissociation appears in the classical expression for the equilibrium hydrogen dissociation pressure,[24, 39, 40, 41]

$$\ell n\ P = K_1 + \frac{H_{diss}}{RT} \quad , \qquad \ldots(38)$$

where K_1 is the solubility coefficient, a function of hydrogen concentration in any single-phase region. Values of H_{diss} are obtained from plots of $\ell n\ P$ as a function of reciprocal temperature (isochores) for constant hydrogen concentration. Isochores for the pure zirconium-hydrogen system, and for both modified and unmodified SNAP fuel material have been experimentally determined by numerous investigators in recent years. Among these, the data of Johnson[42] and Douglas[27] were chosen and used as primary bases for the phase-dependent heats of dissociation in the standard set of parameter values.

The equilibrium hydrogen pressure measurements of Johnson were made on modified fuel material over a composition range from H/Zr = 1.40 to H/Zr = 2.00 in H/Zr intervals of 0.05. Data were obtained on a large number of samples. In addition, particular care was taken to guard against impurity contamination of the samples. The results showed that the heat of dissociation varies somewhat with hydrogen content throughout the delta-epsilon phase region, decreasing from 49.4 kcal/mole of H_2 at H/Zr = 1.40 to 34.0 kcal/mole of H_2 at H/Zr = 2.00. These results are illustrated in Figure 15.

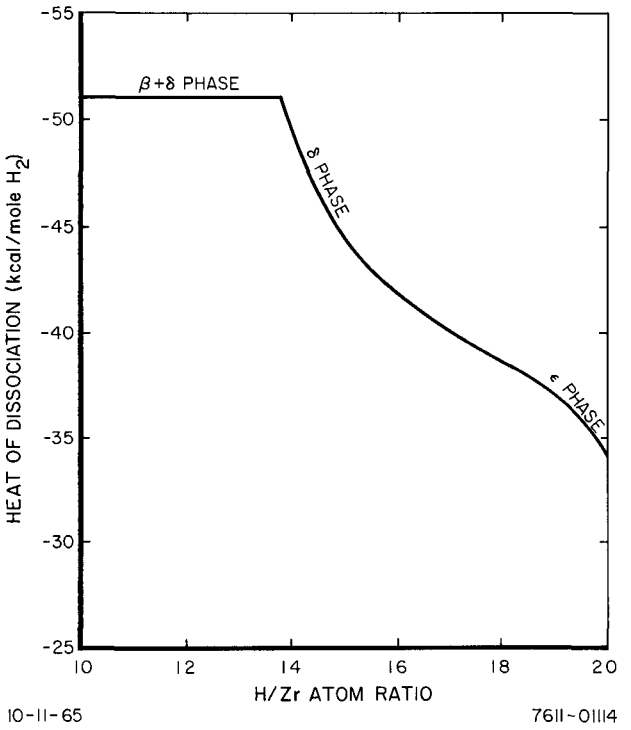

Figure 15. Hydrogen Heat of Dissociation in SNAP Fuel Material at High Hydrogen Concentrations[43]

In a separate investigation, Raymond[40] found the heat of dissociation for pure zirconium hydride to be concentration-dependent within the delta-epsilon phase region. His reported values decrease from 46.3 kcal/mole of H_2 at H/Zr = 1.4 to 37.7 kcal/mole of H_2 at H/Zr = 1.90. These values are in excellent agreement with those of Johnson, both in magnitude and in concentration dependence. Further comparisons can be made with other available data from the literature. Westlake[43] has given a nearly complete collection of heat of dissociation data for all phases of the zirconium-hydrogen system. His summary, supplemented by the addition of the most recent data, is shown in Table 2 for the three phase regions of interest. In this table, consistency in the reported sets of data is most evident.

For the beta phase heat of dissociation, the results of the thermodynamic analysis by Douglas[27] were of particular interest. Douglas based his analysis upon the experimental data from References 22, 37, and 44. Particular equation forms were assumed. His derived H_{diss} values

TABLE 2

HEAT OF HYDROGEN DISSOCIATION DATA

Delta-Epsilon Region			Delta + Beta		Beta Phase			
H_{diss} (kcal/mole of H_2)	H/Zr	Reference	H_{diss} (kcal/mole of H_2)	Reference	H_{diss} (kcal/mole of H_2)	H/Zr	Temperature (°C)	Reference
-45.1	1.38	46	-50.7	46	-39 6	0.65 - 0.89	600 to 900	37
-39.5	1.4 to 1.6	23	-49.6	37	-35 0	0.46	500 to 900	44
-43.5	1.5 to 1.6	47, 48	-53.2†	23	-30.8	0.042	500 to 900	44
Figure 15	1.4 to 2 0	42	-50.8	44	-37.9	0.50	600 to 800	22
-46.3 to -37.7	1.4 to 1.9	40	-52.0	22	-37 7	0 86	680 to 870	38
-45.2	1.25	27	-50.1	47, 48	-34 6	0 44	590 to 880	38
-38.2†	1.75 to 1.86	23	-49.2†	29	-29.6 to -39.8§	0 29 to 0.93	535 to 835	25
-39.6	1.88 to 1.94	41	-53.0 †	42	-37.9 to -40.3	0.57 to 0.75	535 to 835	25
			-52.4	40				
			-51.6	27				
			-50.6	25				
			-47.9§	25				
			-51.8	49				

Estimated from published P-C-T curves
†10 wt % uranium
§1 wt % uranium
25 wt % uranium

are expressed as a function of both temperature and hydrogen content for H/Zr<0.57 and as a function of temperature alone for H/Zr>0.57. The temperature dependence is not great, a deviation of about 3% is effected over a temperature interval of 700°F. The manner in which the values vary with temperature and hydrogen content is not simple. At constant temperature, however, the heat of dissociation becomes lower at lower hydrogen concentrations. The absolute minimum beta phase value is about 32.6 kcal/mole of H_2, whereas the maximum value is about 43 kcal/mole of H_2. An average high temperature value throughout the entire beta phase region is about 40 kcal/mole of H_2.

According to the results of Douglas then, the beta phase heat of dissociation varies somewhat, but not critically, with both temperature and hydrogen concentration. In comparison, Bigony et al.[25] also reported a varying heat of dissociation with hydrogen content which proved similar in concentration dependence but slightly lower in magnitude. Safina and Pavlovskaya,[45] in a Russian paper, report hydrogen dissociation values for various phases from 29 to 42 kcal/mole of H_2, dependent on temperature and hydrogen concentration.

In Table 2, a considerable number of H_{diss} values are listed for the beta+delta, two-phase region. In this region, the equilibrium hydrogen dissociation pressure is independent of hydrogen concentration in observance of the Gibbs Phase Rule on degrees of freedom. It follows that the heat of dissociation is also invariant with concentration within this region. Also, no deviation from linearity in the plotted isochores have been reported so that a temperature dependence is not in evidence. A direct comparison of the values listed in Table 2 is then possible. Weighing each value equally, one obtains for the average value, H_{diss} = -51.0 kcal/mole of H_2. This average value is within 6% of all values listed for the $\beta+\delta$ phase region.

For the standard set of parameter values, the heat of dissociation is assumed to be concentration dependent within the delta-epsilon phase region following the data of Johnson[42] (see Figure 15). In the $\beta+\delta$, two-phase region, the constant average value of -51.0 kcal/mole of H_2 is used. Finally, throughout the beta phase, the high-temperature, average value of -40.0 kcal/mole of H_2 is adopted. These values should be accurate within about 6% except for the beta phase values which are deemed accurate to within about 15%.

5. Emissivity

Experimentally measured emissivity values for the fuel material have been reported by Hedge, et al[31] at the Armour Research Foundation and by Nelson[33] at Battelle Memorial Institute. In these data, considerable variation is noted depending on the environmental and surface conditions, oxygen content, etc. Precise emissivity values appropriate for an oxidizing fuel surface during reentry cannot be deduced from the available data. It is recognized that additional experiments are needed to properly evaluate this important parameter (see Section VIII). The available data do, however, serve to define the range of emissivity values expected during reentry.

For the standard set of parameter values, a constant emissivity value of 0.4 was assumed at all temperatures. This value is in fair agreement with the high-temperature emissivity values reported in References 31 and 33.

6. Hydrogen Diffusion Coefficient

The rate of hydrogen loss from the fuel element is governed by the hydrogen diffusion coefficient. During reentry, the zero hydrogen concentration at the surface of the exposed fuel material provides the sink for the outflow of hydrogen. The high temperatures of the fuel matrix material provide the activation for mobilization of the hydrogen. Providing that the hydrogen outflow is reasonably uniform over the fuel surface, such hydrogen loss may always be described by the ordinary diffusion equation with the "appropriate" diffusion coefficient and boundary conditions. Most important, one must recognize that the appropriate diffusion coefficient is dependent, in addition to temperature, on the environmental conditions and on the mechanism of hydrogen transport. Thus, the diffusion may take place through the matrix material in atomistic form via a vacancy mechanism[50] or the principal mode of transport may be through microcracks, voids, or grain boundaries. During reentry, it appears that each of these mechanisms presents itself and must be considered.

The hydrogen diffusion coefficient in polycrystalline zirconium hydride and zirconium-uranium hydride has been studied by many investigators (References 51 through 58). The results of these studies are summarized in Table 3. Aside from the results of Albrecht and Goode,[51,52] reasonable agreement was obtained among the different investigations

In a nuclear magnetic resonance study on delta phase zirconium hydride, Hon[59] obtained a value of 12.5 kcal/mole for the activation energy of the hydrogen This value agrees very well with the corresponding value obtained by Harkness[57] at Atomics International The latter investigator employed the microbalance weight gain technique to measure hydrogen diffusion coefficients in SNAP fuel material.

TABLE 3

HYDROGEN DIFFUSION COEFFICIENTS
[$D = D_o \exp(-\Delta H/RT)$]

D_o (cm^2/sec)	ΔH (cal/gm-atom)	Temperature Range (°C)	Phase	Reference
4.15×10^{-3}	-9470	450 to 700	α	56
7.00×10^{-4}	-7090±260	305 to 610	α	55
2.17×10^{-3}	-8380	260 to 560	α	58*
7.37×10^{-3}	-8540±1050	870 to 1100	β	56
5.32×10^{-3}	-8320±170	760 to 1010	β	53
$6.14 \times 10^{+4}$	-43,900	650 to 850	β	51
3.23×10^{-5}	-9700	20 to 80	δ	58*
1.09×10^{-3} $\pm 0.3 \times 10^{-3}$	-11,400	60 to 250	δ	54
$5.99 \times 10^{+2}$	-34,800	500 to 750	δ	52
9.18×10^{-3}	-12,400	650 to 900	δ	57†

*In Zircaloy-2 at 61 to 65 at. % hydrogen
†In Zr - 10 wt % U hydride

The standard hydrogen diffusion coefficients for polycrystalline fuel (without microcracks) are taken, in this study, to be those obtained by Harkness[57] in the delta phase and by Gelezunas[53] in the beta phase. These coefficients are plotted as a function of inverse temperature in Figure 16.

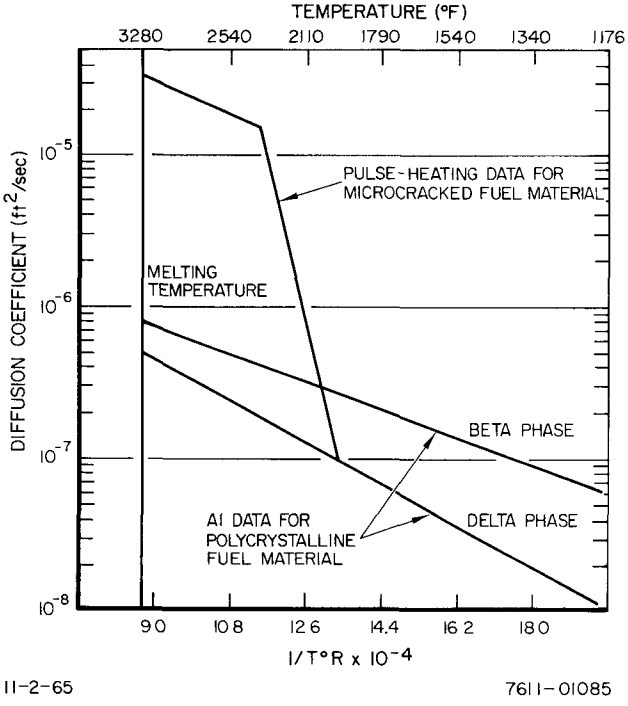

Figure 16. Hydrogen Diffusion Coefficients in SNAP Fuel Material as a Function of Reciprocal Temperature

Under rapid dehydriding conditions, the fuel material is known to develop microcracks and voids. When this happens, the foregoing diffusion coefficients are no longer valid. Use must then be made of an "effective" diffusion coefficient derived from available experimental data. At the present time, such experimental data are somewhat meager for the particular conditions being considered, although further appropriate experimental research is now being planned and conducted under the Aerospace Nuclear Safety Program at Atomics International.

In recent experiments conducted at Battelle Memorial Institute,[60] several 6-in.-long sections of SNAP 10A fuel slugs were rapidly dehydrided at temperature levels around 1800°F. Audible cracking was noted during heatup, beginning when the sample temperature reached 1450°F. The rate of cracking increased at higher temperatures. In all cases, the dehydrided samples were characterized by a uniform distribution of fine cracks, as clearly evidenced by the photograph labled Figure 4 in Reference 60 (see Figure 17).

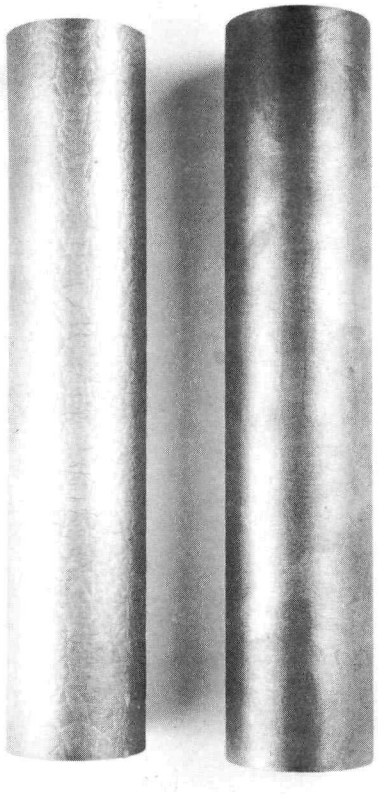

10-11-65 7611-01115

Figure 17. Six-inch Section of a SNAP 10A Fuel Element Before and After Rapid Dehydriding at 1800°F

The results of similar experiments have been reported by Leadon, et al.[8] and also by Hedge, et al.[31] In these experiments, SNAP fuel samples were heated and exposed to various environments. In all cases, microcracking of the samples was evident. Leadon, et al.[8] reported strong hydrogen outgassing at all temperature levels above 800°C. The authors concluded that the hydrogen desorption rates were diffusion limited. Hedge, et al.[31] found that the dehydriding of the specimens in the temperature range 1550 to 2910°F could be given by a log time-reciprocal temperature plot (Figure 47 of Reference 31). The hydrogen loss was continuous with no tendency for disintegration of the samples. The time required for 90% loss of the hydrogen at the fuel melting temperature was given as about 50 sec.

In experimental tests which more closely simulate a reentry environment, Baughn[9] has characterized SNAP fuel behavior during reentry-type heating in a hyperthermal wind tunnel. This facility is a continuous-running wind tunnel which produces a nominal Mach-3 gas flow at high temperature by passing an electric arc through a gas and expanding it through a contoured nozzle to impinge on the test specimen. Two-in.-long SNAP 10A diameter fuel slugs were subjected to transient heating over a range of heating rates and for several different orientations, including cross-axial spinning. Post-test microstructural analyses revealed a fine network in the fuel interspersed with a few large cracks which seemed to originate from holes provided for thermocouples or tungsten holding rods. The material in the vicinity of a molten surface was always devoid of hydrogen. Hydrogen was lost such that discrete interfaces were formed between the phases present.

All of these experimental tests characterize the phenomena of fuel heating and dehydriding by a nonviolent and steady occurrence of microcracking at temperatures above 1500°F, accompanied by a graded step increase in hydrogen loss rates. There is no evidence to indicate that the hydrogen outflow is principally irregular, or that it occurs in "spurts". One may conclude that the evidence is compatible with the assumption that the hydrogen outflow is reasonably uniform and can be described by the diffusion process using an empirical diffusion coefficient. Such an effective diffusion coefficient, however, cannot be deduced from these tests.

In 1962, work was initiated at Atomics International, under the Aerospace Nuclear Safety Program, on a series of experiments designed to simulate the effects of severe temperature transients on SNAP fuel behavior. In these tests, pulse-heating techniques are used in which samples are directly heated by passing large electric currents through them. Such experiments are capable of providing continuous data on power input, electrical resistivity, heat capacity, temperature, and amount and

rate of hydrogen evolution for fuel samples heated to over 2000°F in a few tenths of a second. The results of the experiments performed to date are presented in References 28, 29, and 30.

In the pulse-heating experiments, quantitative data on the amount of hydrogen evolved were obtained as a function of time. Through differentiation of the hydrogen pressure vs time plots, it was possible to derive an effective diffusion coefficient for the outflowing hydrogen, appropriate for the particular pulse-heating conditions. Such calculations were made for transients with various heating rates. The results are shown in Figure 16, in which the effective diffusion coefficient is plotted as a function of inverse sample temperature. Near identical results were obtained for all transients considered, independent of the sample heat input.

From the pulse-heating data, then, the effective diffusion coefficient shown in Figure 16 was determined with which the observed hydrogen evolution could be described for all transients. Below about 1900°F, the hydrogen loss was meager, which was compatible with the standard diffusion rates in polycrystalline fuel material. Within the temperature range 1900 to 2300°F, the hydrogen loss rates increased markedly due to microcracking effects on the hydrogen mean free path. Data scatter was more pronounced in this temperature range. Above 2300°F, the data stabilized and showed a less drastic evolution rate increase with higher temperatures. Apparently, little or no further microcracking occurred above 2300°F, which resulted in a near-constant mean free path.

The effective diffusion coefficient shown in Figure 16 was used in the standard set of parameter values for the reentry and arc-jet analytical model calculations The underlying assumption of the applicability of this coefficient in a reentry environment, under reentry heating rates, was tested by subsequent correlation with the arc-jet test results. Such correlations are discussed in Section VII.

7. Thermal Conductivity

The thermal conductivity of the fuel material is not a highly influential parameter in reentry calculations. The influence of the thermal conductivity, k, upon the heat necessary to initiate melting of the fuel is shown in Section VIII-B. For values of k greater than about 12 Btu/ft-hr-°F, the influence upon the heat necessary to initiate melting is negligible, assuming standard values for all other parameters. The parameter becomes increasingly important as it becomes smaller. For fuel element reentry calculations, precise determinations of the thermal conductivity are not necessary unless the values prove to be lower than about 12 Btu/ft-hr-°F.

The available results of thermal conductivity measurements on actual fuel material are reported in References 31, 33, 34, and 35. Generally, in such measurements, only the data obtained for temperatures less than 1000°F can be considered as reliable. Measurements at higher temperatures are complicated by the movement of hydrogen. Results of analytical calculations show that for typical reentry hydrogen currents, migrating hydrogen is small (<6%) compared to the heat conducted through the fuel matrix material. Hydrogen dissociation effects, however, can strongly influence temperature measurements in a heated rod, generally in such a way as to increase the apparent (measured) thermal conductivity.

In evaluating available thermal conductivity values, relevant data have been restricted to two temperature regions (1) temperatures from 0 to about 1000°F and (2) temperatures near the melting point (3280°F) of the fuel. Temperatures between these two ranges correspond to the period of

hydrogen evolution. At the higher temperature range, most all hydrogen should be evolved. The properties of the fuel should then approach those of unhydrided Zr - 10 wt% U alloy, except for possible effects of microcracking and increased porosity caused by the rapid dehydriding.

Thermal conductivity data of interest in fuel element reentry studies are shown in Figure 18. Below 1000°F, the composition of the fuel remains constant so that the indicated data curves for the fully hydrided fuel would apply. Here, either the Armour data or the Atomics International data may be used with similar results.

Above 1000°F, one is guided by the corresponding data for the unhydrided Zr - 10 wt % U alloy. It is reasonable to assume that, up to the time that the fuel is depleted of hydrogen, the fuel thermal conductivity values will remain higher than those for the unhydrided material. Such values appear to be beyond the range of effectual thermal conductivity values and, as such, need not be determined exactly.

Near the melting point, the thermal conductivity of the dehydrided fuel may actually become less than that of the unhydrided alloy. As mentioned before, this could be caused by the formation of microcracks and voids. According to the Armour data, the thermal conductivity of the unhydrided alloy approaches a value of about 25 Btu/ft-hr-°F at the melting point. (Corresponding data for the hydrided material presented in Reference 31 are even higher. These measurements appear, however, to be influenced by reactions with the hydrogen atmosphere in the furnace.) It seems difficult to postulate that even excessive microcracking could reduce the thermal conductivity by more than a factor of two. Thus, the high-temperature thermal conductivity of the dehydrided fuel should be at least as great as 12 Btu/ft-hr-°F, the minimum value for no influence of the parameter.

In the standard set of parameter values, a constant thermal conductivity of 13.3 Btu/ft-hr-°F was assumed for the fuel material. It is recognized that some additional experimental data for the thermal conductivity is needed, especially at higher temperatures for rapidly dehydrided fuel material.

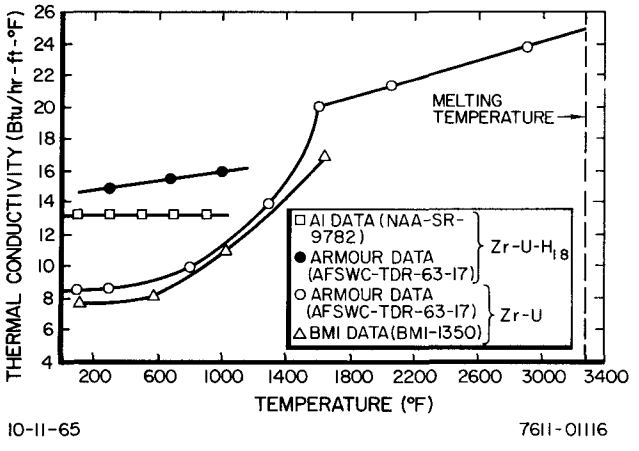

Figure 18. Thermal Conductivity as a Function of Temperature

8. Density

The density of SNAP fuel material is a well known quantity. Experimental density values are given in References 24, 33, 34, and 35. All of these values agree well. From Reference 35, a density value of 6.09 gm/cm^3 (380.2 lb/ft^2) was obtained, corresponding to H/Zr ratios in the range of 1.7 to 1.8. This constant value was used throughout the reentry calculations, commensurate with the assumption of fixed geometrical dimensions. (If the fuel element dimensions remain constant, then so also must the density if mass is to be conserved.) The density value used is believed accurate to within a few per cent.

9. Surface Catalytic Efficiency

The aerodynamic heating equations (see Section IV) for the continuum flow regime may be directly applied under the specific condition of an equilibrium boundary layer. A reentering SNAP reactor fuel element passes through regions of altitude and velocity, however, where the air behind the shock and in the boundary layer may not be in equilibrium. The equilibrium aerodynamic heating rate must then be adjusted to account for the chemical kinetics effects.

Nonequilibrium effects behind the shock, in the boundary layer, and on the surface have been studied by Chung[61] and by Inger.[62] In these studies, the reduction in heating is expressed as a function of altitude and the catalytic efficiency of the material surface. The catalytic efficiency is defined as:

$$\gamma_A = \frac{\text{Atomic collisions effective in recombination}}{\text{Total number of atomic collisions}} .$$

The actual value of the catalytic efficiency for the fuel element surface could not be found in the literature. Values for other materials, however, have been reported. The existing data suggest that a metal surface has a γ_A of about 5×10^{-2} and an oxide surface has a γ_A of about 1×10^{-2}.

The reduction in heating for a nonequilibrium boundary layer can be inferred from References 61 and 62 for the appropriate fuel element radius and range of catalytic efficiency values. The heating reduction is shown in Figure 19 as a function of altitude for different catalytic efficiency values. For values of γ_A in the range 1×10^{-2} to 5×10^{-2}, the reduction in heating to a SNAP 10A reactor fuel element varies from about 0.95 at higher altitudes to around 0.85 to 0.90 at an altitude of about 150,000 ft.

In the standard set of parameter values, a constant value of 0.95 was assumed (at all altitudes) for the aerodynamic heat reduction due to noncatalytic wall effects. It is recognized that experimental investigation is greatly needed to determine a more accurate surface catalytic efficiency value. With such a value, an accurate evaluation of the heating reduction can be made using the methods of References 61 and 62.

B. HASTELLOY-N CLADDING

SNAP fuel elements consist of cylindrical fuel-moderator (Zr - 10 wt % U hydride) rods canned in a Hastelloy-N cladding tube with a small fuel-cladding gap volume. The inside surfaces of the cladding tube and the end caps (the elements are sealed by means of welding in the end caps) are coated with a material which impairs hydrogen permeation of the cladding. The material properties of the cladding tube are cited in Reference 63, and those of interest here are listed in Table 4. For the values given, the coating material was not considered or included.

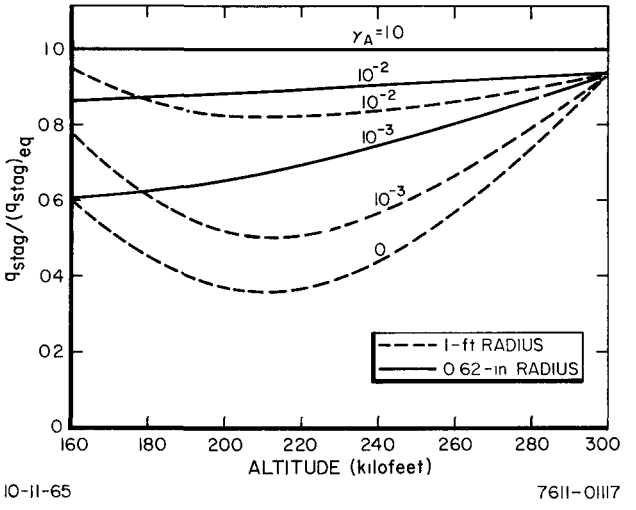

Figure 19. Catalytic Efficiency Effect on the Stagnation Point

TABLE 4

HASTELLOY-N CLADDING PROPERTIES[63]

Property	Value	Comment
Specific heat	0.13 Btu/lb-°F	Average high-temperature value
Density	0.317 lb/in.^{3}	-
Emissivity	0.3	Typical value for nickel alloys
Heat of fusion	133 Btu/lb	Typical value for nickel alloys
Melting point	2400 ± 30°F	-

VI METHOD OF SOLUTION

Beginning from the time of fuel element release, the heat and mass transfer Equations 1 through 8 are solved simultaneously by finite difference methods. These solutions are coupled with the iterative calculation of the net surface heat flux (Equation 9) through the fuel surface temperature and the hydrogen outflow. The solutions are achieved using the Thermal Analyzer Program (TAP-3), a digital code written for use on the IBM-7090 computer. Basically, this involves application of finite difference forms to each basic equation, relegation of these forms to the analogous TAP-3 admittance-capacitance circuit network, and the coupling of the equations by the available TAP-3 arithmetic functions

TAP-3 is a general digital computer code applicable to the solution of transient and steady-state problems involving heat transfer and analogous processes. The present code is an outgrowth of the Lockheed Thermal Analyzer Program.[64] A detailed description of the method by which this code is utilized in obtaining material response solutions is given in this section.

A. FINITE DIFFERENCE FORMS

In preparing a problem for solution with the code, it is first necessary to approximate the physical system with a lumped-geometry network. In this network, the total storage capacity of the physical system is assumed to be apportioned among a set of discrete lumps or increments. Each increment is assumed to be connected to each of its neighbors by one or more connecting paths, each having a value called the 'admittance' (reciprocal of the resistance). Each increment may be assigned a heat generation rate that is equivalent to the rate of heat generation in the element of volume of the physical system represented by the increment. The potential assigned to or calculated for each incremental node is defined as the potential at the centroid of the corresponding increment to which the node is assigned. Since we are considering the simultaneous transfer of heat and mass, we can consider a superimposed incremental representation where each increment may have more than one type of potential or node. For example, an increment may be characterized by a temperature and a concentration.

The following diagram illustrates the one-dimensional nodal scheme for calculations with uniform surface heating. The cylindrical fuel slug is broken up (usually) into six radial increments of equal thickness (0.101 in.). Nodes 1-6 represent the average increment temperatures, respectively, from the fuel center to the outside. Nodes 11-16 represent the average increment hydrogen concentrations Nodes 7 and 17 represent the surface temperature and surface concentration, respectively.

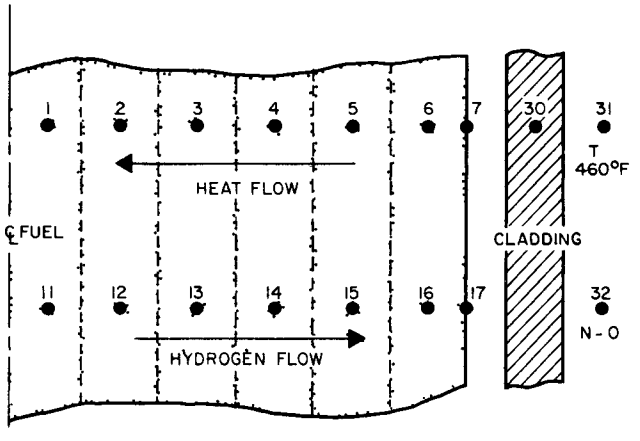

In the calculation process, aerodynamic heating is initially specified to the cladding node 30. A heat balance is computed for the cladding as explained before and the cladding temperature rises. The Hastelloy-N cladding reaches its

melting temperature at 2400°F, absorbs the heat of fusion (36 Btu), and is excluded from the calculation process. When this takes place, the net surface heating is put into the fuel surface node 7. Hydrogen then redistributes within the fuel (nodes 11-17) and is lost to the sink node 32. A heat and hydrogen balance is then applied to each respective fuel increment. Throughout these calculations, each fuel increment is programmed to change phase according to its own temperature and concentration and the phase diagram shown in Figure 13. In time, complete phase changes sweep across the rod from the outer to the inner regions.

As the fuel surface node 7 reaches the melting temperature of 3280°F, the net heating is transferred to the next node inward, node 6. With this net heating is added a constant radiation heat loss from an emitting temperature of 3280°F. As node 6 reaches 3280°F, the increment begins melting with a heat of fusion of 90 Btu/lb of fuel. When melting is complete, the net heating and radiation heat loss is then transferred to the next node towards the rod center. This process continues until all increments are fully ablated. Throughout the entire process, the variable material properties and parameters are calculated by means of the TAP-3 code arithmetic functions at each node, after each iteration.

The basic finite difference approximation equation applied by the computer code to each node with a non-zero capacitance is, at each iteration,

$$T_{i_{t+\Delta t}} = T_{i_t} + \frac{\Delta t}{C_i}\left\{Q_i + \sum_j \left[Y_{i,j}(T_j - T_i)\right]\right\}_t \quad . \qquad \ldots(39)$$

For nodes with a zero capacitance, such as surface nodes, the basic equation is, at each iteration,

$$T_{i_{t+\Delta t}} = \left[\frac{Q_i + \sum_j (Y_{i,j} T_j)}{\sum_j Y_{i,j}}\right]_t \quad . \qquad \ldots(40)$$

The maximum stable time step, Δt, is limited by the expression,

$$\Delta t \leq \left(\frac{C_i}{\sum_j Y_{i,j}}\right)_{\text{(least value for the set, } i)} \quad . \qquad \ldots(41)$$

The application of finite difference forms to the defining equations must result in a final expression form identical to Equation 39 or Equation 40. In the following, it is shown that the finite difference forms of both the heat and hydrogen continuity equations can be molded into identical expressions of the form of Equation 39. As such, they may be solved side-by-side by means of the TAP-3 code. For the present, it will be assumed that the equations in the second calculations stage (after cladding burnoff) apply. The finite difference forms of the equations in the first and third calculation stage are then discussed at the end of this section.

Consider an internal node, i, along the radius, r, in the following scheme:

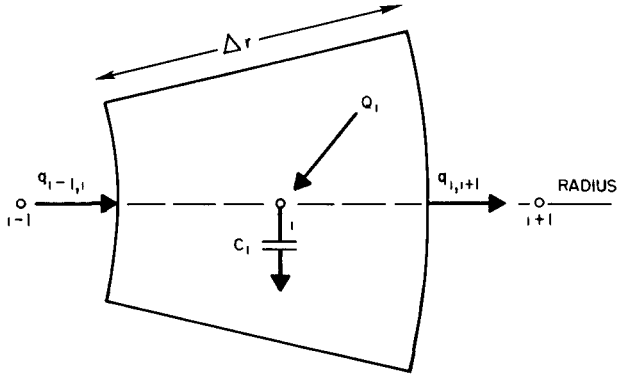

The finite difference form of Equation 6 is

$$\left(\rho C_p\right)_i \frac{T_{i_{t+\Delta t}} - T_{i_t}}{\Delta t} = \left[- \frac{q_{i+1,i} - q_{i,i-1}}{A \cdot \Delta r} - \frac{\left(\overline{C}_p \cdot Z\right)_i}{A} \cdot \frac{T_{i+1} - T_{i-1}}{2\Delta r} + \frac{Q_i}{\Delta V_i} \right]_t \quad . \qquad \ldots(42)$$

Here,

$$q = -k \cdot A \frac{\partial T}{\partial r}, \text{ and } Q_i = \left(H_{diss} \frac{\partial N}{\partial t} \cdot \Delta V \right)_i \quad ,$$

and the subscript, i, i + 1, indicates that the function is evaluated midway between nodes i and i + 1. Setting the identities,

$$C_i \equiv \left(\rho C_p \Delta V\right)_i \quad ,$$

and

$$\Delta V_i = \left(A \cdot \Delta r\right)_i \quad ,$$

into Equation 41, one gets, on rearranging,

$$T_{i_{t+\Delta t}} = T_{i_t} + \frac{\Delta t}{C_i} \left[q_{i,i-1} - q_{i+1,i} - \frac{\left(\overline{C}_p Z\right)_i}{2} (T_{i+1} - T_{i-1}) + Q_i \right]_t \quad .$$

Thus,

$$T_{i_{t+\Delta t}} = T_{i_t} + \frac{\Delta t}{C_i} \left[\left(\frac{-kA}{\Delta r} \right)_{i-1,i} (T_i - T_{i-1}) + \left(\frac{kA}{\Delta r} \right)_{i,i+1} (T_{i+1} - T_i) \right.$$

$$\left. - \left(\frac{\overline{C}_p Z}{2} \right)_i (T_{i+1} - T_{i-1} + T_i - T_i) + Q_i \right]_t \quad .$$

Finally,

$$T_{i_{t+\Delta t}} = T_{i_t} + \frac{\Delta t}{C_i}\left[Y_{i-1,i}(T_{i-1} - T_i) + Y_{i,i+1}(T_{i+1} - T_i) + Q_i\right]_t \quad , \qquad \ldots(43)$$

where

$$Y_{i-1,i} \equiv \left(\frac{kA}{\Delta r}\right)_{i-1,i} - \frac{1}{2}(\bar{C}_p Z)_i \quad ,$$

$$Y_{i,i+1} \equiv \left(\frac{kA}{\Delta r}\right)_{i,i+1} - \frac{1}{2}(\bar{C}_p Z)_i \quad ,$$

and

$$Q_i = H_{diss}\left(\frac{N_t - N_{t-\Delta t}}{\Delta t}\right)\Delta V \quad .$$

Equation 43 is of the same form as the basic TAP-3 finite difference equation. The basic paramters – heat capacity, C_i, total heat flow admittances, $Y_{i-1,i}$ and $Y_{i,i+1}$, and heat source, Q_i – are all functions of the hydrogen concentration change. As such, they depend upon the solution of the hydrogen transport equation as programmed in the analytical description.

For the same scheme as above, the finite difference form of Equation 7 is

$$\frac{N_{i_{t+\Delta t}} - N_{i_t}}{\Delta t} = \left[-\frac{\left(-DA\frac{\partial N}{\partial r}\right)_{i,i+1} + \left(DA\frac{\partial N}{\partial r}\right)_{i-1,i}}{A \cdot \Delta r}\right]_t \quad .$$

Proceeding as before, we get

$$N_{i_{t+\Delta t}} = N_{i_t} + \frac{\Delta t}{\Delta V_i}\left[Y_{i-1,i}(N_{i-1} - N_i) + Y_{i,i+1}(N_{i+1} - N_i)\right]_t \quad , \qquad \ldots(44)$$

where

$$Y_{i-1,i} = \left(\frac{DA}{\Delta r}\right)_{i-1,i}$$

and

$$Y_{i,i+1} = \left(\frac{DA}{\Delta r}\right)_{i,i+1} \quad .$$

Equations 43 and 44 are both of the identical form of the basic TAP-3 finite difference equation for nodes with non-zero capacitance. By specifying the proper network arrangement (nodal connections) and capacitance values (C_1 through C_6 and C_{11} through C_{16}), TAP-3 can be used to apply a heat and hydrogen balance at each of the six radial increments, at each iteration.

Nodes 7 and 17 are zero-capacitance, boundary nodes. They serve to couple the surface heating phenomena with the internal processes and to supply the appropriate boundary conditions. The boundary Equations 8 and 10 can be given in finite difference forms,

$$T_{7_{t+\Delta t}} = \left(\frac{Q_7 + Y_{7,31} T_{31} + Y_{6,7} T_6}{Y_{6,7} + Y_{7,31}} \right)_t \quad , \qquad \ldots(45)$$

where

$$Q_7 = q_{net} \cdot A_s \quad ,$$

$$Y_{6,7} = \left(\frac{kA}{\Delta r} \right)_{6,7} - \frac{1}{2} (\overline{C}_p \dot{Z})_7 \quad ,$$

$$Y_{7,31} = \sigma_1 \epsilon A_s (T_7 + 460)^3 \quad ,$$

and

$$N_{17_{t+\Delta t}} = \left(\frac{Y_{16,17} N_{16} + Y_{17,32} N_{32}}{Y_{16,17} + Y_{17,32}} \right)_t \quad , \qquad \ldots(46)$$

where

$$Y_{16,17} = \left(\frac{DA}{\Delta r} \right)_{16,17} \quad ,$$

and

$$Y_{17,32} = \frac{D_F A_s}{\Delta \tau_1} \quad .$$

Before cladding burnoff, the material response equations are simpler. Equations 3 and 4 can be expressed in finite difference form, and according to the same nodal scheme as before, as

$$T_{30_{t+\Delta t}} = T_{30_t} + \frac{\Delta t}{C_{30}} \left[Q_{30} + Y_{7,30} (T_7 - T_{30}) + Y_{30,31} (T_{31} - T_{30}) \right]_t \quad , \qquad \ldots(47)$$

where

$$C_{30} = V_c \cdot C_{p_c} \cdot \rho_c \quad ,$$

$$Q_{30} = q_{aero} \cdot A_s \quad ,$$

$$Y_{7,30} = \frac{\sigma_1 A_s (T_7 + T_{30} + 920) \left[(T_7 + 460)^2 + (T_{30} + 460)^2 \right]}{1/\epsilon_c + 1/\epsilon - 1} \quad , \text{ and}$$

$$Y_{30,31} = \sigma_1 A_s \epsilon_c (T_{30} + 460)^3 \quad .$$

In the third stage of calculation, the ablation period, the application of the equations of the second stage is continued, except for those nodes which have reached the melting temperature. These latter nodes are manipulated to simulate meltdown and ablation as explained previously.

A complete summary of the finite difference forms for each node, at any time, t, is given in Table 5.

B. INPUT TO THE TAP-3 CODE

Basic input data to the code are broken down into the following main categories:

1) *10 – network connections and nodal arrangement
2) *20 – initial and constant values
3) *30 – function specifications
4) *40 – tabular data
5) *50 – latent heat data
6) *70 – run control constants
7) *80 – printout specifications
8) *90 – running and print times.

The typical one-dimensional nodal scheme for reentry calculations is given in the previous section. This same scheme is utilized to describe the program input data throughout this section.

Initial values and program constants are specified under *20 data. Initial temperatures for the fuel nodes 1-7 and the cladding node 30 are given as 500°F in standard reentry calculations. For arc-jet calculations, initial temperatures of 80°F are appropriate. The space environmental temperature at node 31 is flagged and held constant at -459.69°F. (The corresponding environmental temperature for arc-jet calculations is 80°F.) Initial concentrations to nodes 11-16 are expressed as 6.61 lb of H_2/ft^3, corresponding to an H/Zr ratio of 1.8. The concentration of hydrogen in the boundary layer (node 32) is held constant and equal to zero. Also included under *20 data are the concentration node capacities which, through a comparison of Equation 39 with Equation 44, are seen to equal the respective incremental volumes. Finally, the cladding heat capacity, C_{30}, and the constants used in *30 arithmetic function specifications are given.

The basic activity of the *30 input data is to specify to the code the arithmetic computations necessary to compute the problem parameters which vary with time, temperature, or in any predictable manner. In addition to algebraic operations, use may be made of a repertory of conditional or "if" statements to perform "in-run" switching and transfer operations. A detailed understanding of the exact function of each *30 input statement requires a knowledge of the available code mathematical operations and the numbering or call system. To illustrate what is being performed by these *30 statements, a flow chart is presented in Figure 20, in which an outline is given of the principal *30 calculations made after each iteration in a typical reentry solution. The sequential order is consistent with the individual *30 statements used in actual computations.

Under *40 data, parameters which do not vary according to a simple mathematical law are specified in tabular form. Such parameters are H_s, the air stagnation enthalpy; F_c, the fraction of completion for hydrogen-oxygen reactions; and $\bar{q}_{cyl}$, the average cold wall aerodynamic heat rate. These three parameters are specified as functions of time under appropriate *40 tables. As explained in Section IV-A, such tables are compiled from RESTORE fuel element trajectory calculations.

Nodes	TAP-3 Iterative Equation	Admittance Expressions at Each Time, t		Source Term
1-6 (Fuel increment temperature nodes)	$T_{t+\Delta t_i} = T_{t_i} + \frac{\Delta t}{C_i}\left[Y_{i-1,i}(T_{i-1} - T_i) + Y_{i,i+1}(T_{i+1} - T_i) + Q_i\right]_t$	$Y_{i-1,i} = \left(\frac{kA}{\Delta r}\right)_{i-1,i} - \frac{1}{2}(\bar{C}_p Z)_i$ if $T_i \leq 3280$ $Y_{i-1,i} = 0$ if $T_i > 3280$	$Y_{i,i+1} = \left(\frac{kA}{\Delta r}\right)_{i,i+1} - \frac{1}{2}(\bar{C}_p Z)_i$ if $T_{i+1} \leq 3280$ $Y_{i,i+1} = 0$ if $T_{i+1} > 3280$	$Q_i = \frac{H_{diss}}{\Delta r}(N_{i,i+1} - N_{i-1,i})$ if $T_{i+1} \leq 3280$ $Q_i = (q_{net} - q_{rad})A_s$ if $T_{i+1} > 3280$
7 (Fuel surface temperature node)	$T_{t+\Delta t_7} = \left(\frac{Q_7 + Y_{7,31}T_{31} + Y_{6,7}T_6}{Y_{6,7} + Y_{7,31}}\right)_t$	$Y_{6,7} = \left(\frac{kA}{\Delta r}\right)_{6,7} - \frac{1}{2}(\bar{C}_p Z)_7$ if $T_7 < 3280$ $Y_{6,7} = 0$ if $T_7 \geq 3280$	$Y_{7,31} = \sigma_1 \epsilon A_s (T_7 + 460)^3$ if $T_{30} > 2400$ $Y_{7,31} = 0$ if $T_{30} \leq 2400$	$Q_7 = q_{net} A_s$ if $T_7 < 3280$ and $T_{30} > 2400$ $Q_7 = 0$ if $T_7 \geq 3280$
30 (Cladding node)	$T_{t+\Delta t_{30}} = T_{t_{30}} + \frac{\Delta t}{C_{30}}\left[Q_{30} + Y_{7,30}(T_7 - T_{30}) + Y_{30,31}(T_{31} - T_{30})\right]_t$	$Y_{30,31} = \sigma_1 \epsilon_c A_s (T_{30} + 460)^3$ if $T_{30} \leq 2400$ $Y_{30,31} = 0$ if $T_{30} > 2400$	$Y_{7,30} = \frac{\sigma_1 \epsilon A_s}{1/\epsilon_c + 1/\epsilon - 1}(T_7 + T_{30} + 920) \cdot \left[(T_7 + 460)^2 + (T_{30} + 460)^2\right]$ if $T_{30} \leq 2400$ $Y_{7,30} = 0$ if $T_{30} > 2400$	$Q_{30} = q_{aero} \cdot A_s$ if $T_{30} \leq 2400$ $Q_{30} = 0$ if $T_{30} > 2400$
11-16 (H_2 concentration increment nodes)	$N_{t+\Delta t_i} = N_{t_i} + \frac{\Delta t}{\Delta V_i}\left[Y_{i-1,i}(N_{i-1} - N_i) + Y_{i,i+1}(N_{i+1} - N_i)\right]_t$	$Y_{i-1,i} = \left(\frac{DA}{\Delta r}\right)_{i-1,i}$ at all times	$Y_{i,i+1} = \left(\frac{DA}{\Delta r}\right)_{i,i+1}$ at all times	$Q_i \equiv 0$
17 (H_2 concentration surface node)	$N_{t+\Delta t_{17}} = \left(\frac{Y_{16,17}N_{16} + Y_{17,32}N_{32}}{Y_{16,17} + Y_{17,32}}\right)_t$	$Y_{16,17} = \left(\frac{DA}{\Delta r}\right)_{16,17}$ at all times	$Y_{17,32} = \frac{D_F A_s}{\Delta r_1}$ if $T_{30} > 2400$ $Y_{17,32} = 0$ if $T_{30} \leq 2400$	$Q_i \equiv 0$

Table 5. Summary of Iterative TAP-3 Equations and Parameter Terms

BLANK

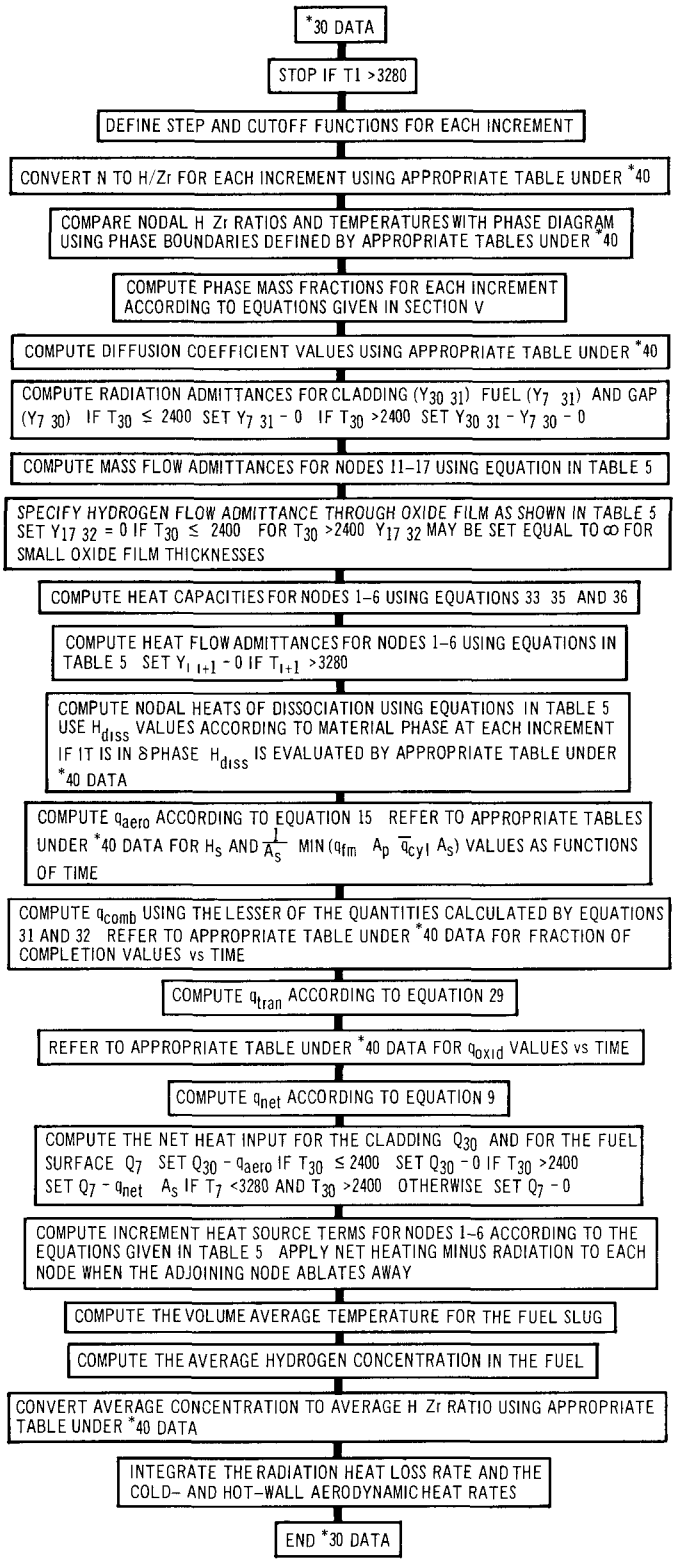

Figure 20. Analytical Model 30 Data Flow Chart for TAP-3 Code

Also under 40 data is a table converting N (lb of H_2/ft^3) to the H/Zr ratio, according to the equation,

$$N = \frac{0.9\rho(H/Zr)}{(H/Zr) + 91.22} \quad . \qquad \ldots (48)$$

The heat release due to fuel oxidation is given in the appropriate table under 40 data as a function of surface temperature according to Figure 10. Also under 40 data is a table used for evaluations of the diffusion coefficient as a function of inverse temperature as given in Figure 16. Other 40 tabular data represent the delta-beta + delta and the beta-beta + delta ZrH_x phase boundaries of the ZrH_x phase diagram (see Figure 13).

Latent heat input information is specified to the code under 50 data. Under the latent heat subroutine, the temperature of an increment is held constant at the melting point until a heat quantity equal to the incremental heat of fusion is absorbed by the increment. The TAP-3 code performs this operation automatically for each increment whose melting temperature and latent heat is specified under 50 data. In fuel element reentry calculations, the melting temperature is taken to be 3280°F and the heat of fusion is assumed to be 90 Btu/lb of fuel. The incremental latent heats are then obtained from the relationship,

$$(\Delta H_f)_1 = 90\rho\Delta V_1 \qquad \text{(Btu)} \quad .$$

The TAP-3 code computes, at each iteration, the maximum allowable iterative time step according to Equation 41. This maximum time step varies with changing capacity and admittance values. Under 70 data, it is possible to specify, to the code, a constant time step value which, throughout the run, must always be less than the maximum allowable value. For most reentry (and arc-jet) calculations, a constant time step of 0.2 sec was used.

Variables to be printed out at each scheduled printout time are specified under 80 data. The printout schedule throughout the run is put in under 90 data. For typical reentry calculations, printouts were made every second after fuel element release, except during a short "check period," in which printouts were made every iteration for five iterations. Computer machine time averaged about 2 min for each computer run, both for reentry calculations and arc-jet test simulations.

VII. RESULTS USING STANDARD SET OF PARAMETERS

The methods discussed in the previous sections by which the thermal history of a SNAP fuel element is calculated throughout reentry can be summarized by the following three-step procedure. Given a release altitude along the reference reactor vehicle trajectory and assuming a particular flight orientation, the independent fuel element trajectory transients (aerodynamic heating, stagnation enthalpy, velocity, altitude, etc.) are computed using the trajectory code RESTORE. Necessary initial conditions for the RESTORE code computation, such as velocity, flight angle, location, and heading, are obtained from the reference vehicle trajectory at the altitude of fuel element release.

In the second step, the appropriate heating factors are applied to RESTORE-computed heating rates to obtain tabular values of the average cold-wall aerodynamic heat rate to the element as a function of time. Also in the second step, tabular values of the stagnation enthalpy and the fraction of completion for hydrogen combustion are obtained as functions of time, based on the RESTORE code results.

In the final step, the tabular values obtained in step two are specified to the analytical, material response model. Calculations are then made, using the TAP-3 code as explained before, to determine the thermal behavior of the fuel element under the specified conditions.

The characteristic results of the material response calculations for a reentering SNAP 10A fuel element are presented in this section using the most current, standard set of parameter values listed in Section VIII. The purpose of these results is to define the conditions necessary for complete meltdown and ablation of the fuel material, based on up-to-date research regarding the processes and parameters involved.

Before these results are presented, the correlation of the analytical model with the first series of hyperthermal wind tunnel (arc-jet) experiments[9] is discussed.

A. ARC-JET TESTS

A brief description of the first series of arc-jet tests conducted on SNAP fuel material under the Aerospace Safety Program is given in Section V. The detailed experimental description and results of these tests were published in Reference 9. The tests of interest here involve those categorized in Reference 9 as Configuration I-B, in which the cylindrical specimens were exposed cross-axially to the jet and rotated at approximately 4 rps. The initial temperature of the fuel was 80°F and the initial hydrogen concentration was equal to that for a fully hydrided SNAP 10A fuel element (H/Zr = 1.8). Some of the specimens tested were clad, while others were unclad. Heating rates and stagnation enthalpies varied from test run to test run but remained constant throughout each run.

The experimental data obtained from these tests are not to be regarded as rigorously precise, although the accuracy was relatively good for tests of this kind. Nevertheless, the tests do provide a measure of comparison for the analytical description.

The analytical fuel element model discussed previously was adapted to simulate the conditions of the arc-jet tests. The initial temperature of the fuel and cladding was specified as 80°F, as was

the ambient temperature for radiation. The fraction of completion for hydrogen combustion was evaluated from test condition boundary layer pressures and temperatures. For the test runs considered, the fraction of completion was calculated to be about 0.15, constant throughout each run. The hole drilled through the axial center of the specimens to accommodate the tungsten support rod was simulated by a void space in the analytical model geometry for most calculations, although some trial calculations were made without this void. The average-to-stagnation-point heating factor, F_Q, used for the cross-axial, rotating specimens was 0.375 instead of 0.36 as used in reentry calculations. The value 0.375 was based on the experimental calibrations for the 2-in.-long specimens given in pages 50 and 51 of Reference 9. The higher value results from the fact that the specimens are of insufficient length to approximate cross-axial flow on an infinitely long cylinder.

Typical results of the analytical model calculations of the fuel surface temperatures are shown and compared with the experimental data in Figures 21 through 23. These calculations were obtained using the most current, standard set of parameter values listed in Section VIII. The agreement with the experimental data is shown to be good, both for times of initial fuel melting and for times of complete ablation. For the calculated time to initial ablation, the standard mean deviation (defined in Section VIII) for each of these cross-axial runs is about 15 to 17 sec, depending on the exact heating rate. (The standard mean deviation, σ, calculated in Section VIII for cross-axial flow is 1450 Btu/ft^2. This deviation can be expressed in units of time, for a constant heat rate, by dividing by the heat rate.) As can be seen from the figures, the experimental data fall, in all of these cases, within the standard mean deviation.

For the clad runs, the times of calculated cladding burnoff were found to reasonably approximate those actually observed. That is, the cladding material was calculated to ablate in a few seconds following specimen insertion into the jet.

In the arc-jet test analysis, the opportunity was taken to vary some of the procedures of the analytical model to test the results. One such procedure varied was the simulation of microcracking within the fuel material increments. The standard procedure of the analytical model assumes simultaneous microcracking of all increments with equal hydrogen diffusion rates for all increments according to Figure 16. The reference temperature for these diffusion rates is taken to be the temperature of the outermost increment. This is equivalent to the assumption of instantaneous microcrack propagation throughout the fuel.

An alternative method would be to treat each increment independently of the others, so that a gradual progression of microcracking would be simulated across the radial increments. In this procedure, the hydrogen diffusion rate of any particular increment is given by Figure 16 as a function of the temperature of that increment. With surface heating, the outermost increment undergoes a sharp increase in diffusion rates when the temperature of that increment reaches about 1900°F (see Figure 16). The adjoining increment, however, does not experience this sharp increase until its own temperature reaches 1900°F, and so on. The nodal progression of microcracking and increased diffusion rates across the fuel proceeds slowly over a relatively long period of time in this simulation. This slowness is due to the near total absorption of the heat input into the fuel by the outermost increment, which is not devoid of hydrogen, to counteract the energy loss in this increment due to hydrogen dissociation. That is, the outermost increment reaches 1900°F, undergoes

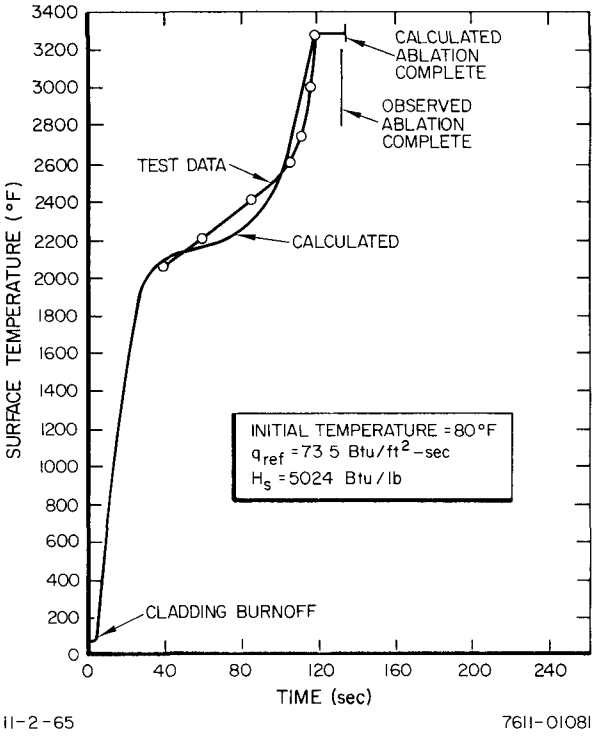

Figure 21. Arc-Jet Run No. 3.12 — Clad Fuel Surface Temperature vs Time

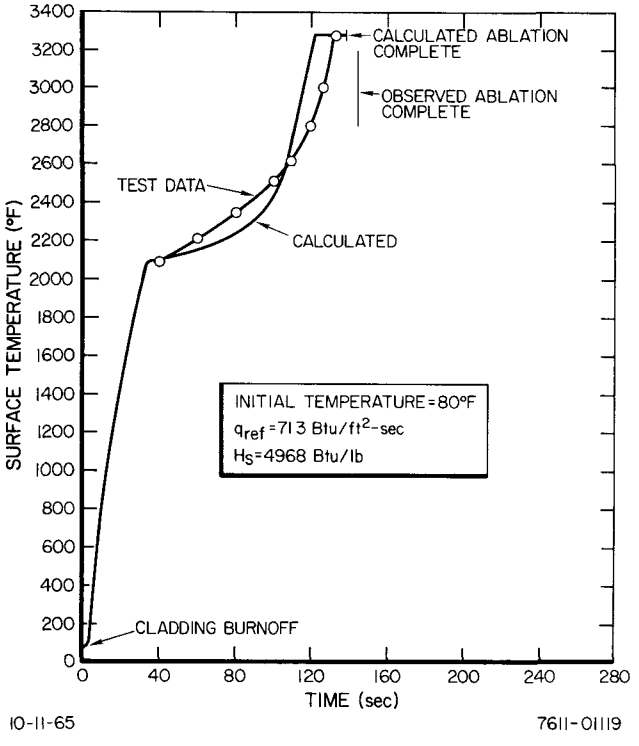

Figure 22. Arc-Jet Run No. 3.8 — Clad Fuel Surface Temperature vs Time

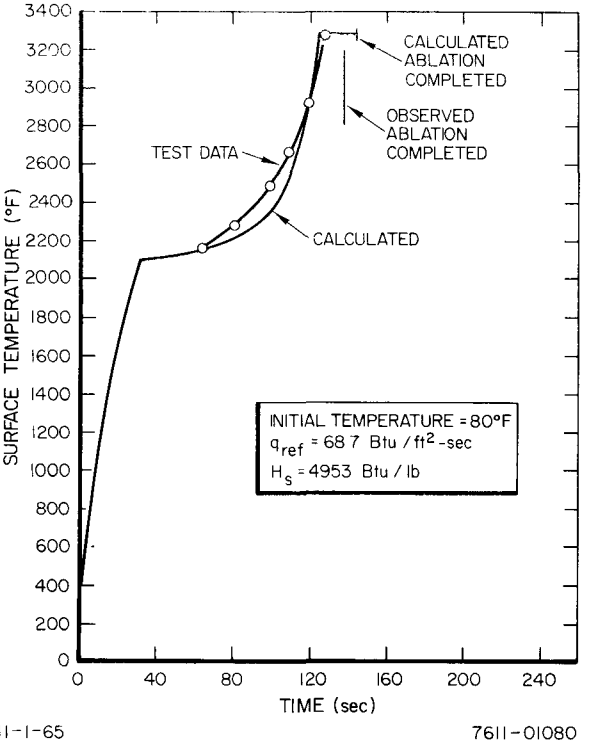

Figure 23. Arc-Jet Run No. 4.16 — Unclad Fuel Surface Temperature vs Time

microcracking and rapid hydrogen evolution at near-constant temperatures, and becomes practically devoid of hydrogen before the same thing occurs at the adjoining increment.

The result of a typical arc-jet test calculation using this procedure is shown in Figure 24. All parameters used in this calculation were identical to those used above. Examination of the resulting surface temperature trace and comparison with the experimental data indicates that the overall hydrogen loss from the fuel was slower in the calculations than that which would explain the measured data. Use of even greater rates of increase in the diffusion coefficient $[-\partial \ell n\, D/\partial(1/T)]$, after microcracking, was found, by actual calculations, to result in no alleviation of disparity. [Use of a near-infinite value of $-\partial \ell n\, D/\partial(1/T)$ results in a model similar to the preliminary fuel behavior model presented in References 1 and 9. That is, for large values of $-\partial \ell n\, D/d(1/T)$, the process of hydrogen dissociation approaches that characteristic of an isothermal phase change.]

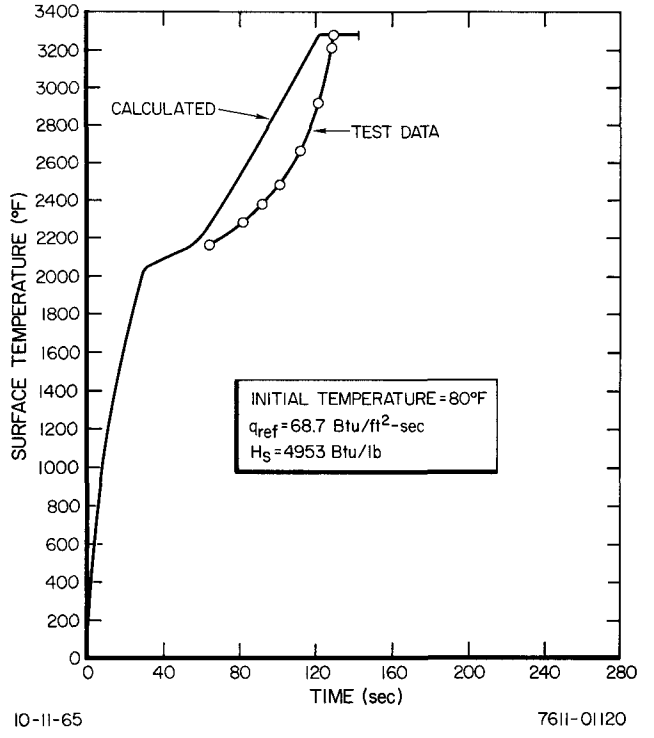

Figure 24. Arc-Jet Run No. 4.16 — Unclad Fuel Surface Temperature vs Time (assuming gradual microcrack propagation)

Trial calculations were also made to evaluate the effect of the hole provided for the tungsten rod holder. The results of these calculations showed that little deviation could be noted between calculations made with and without simulation of the center hole.

From the correlation of the arc-jet test calculations with the experimental data, it is concluded that use of the standard analytical model with the latest, standard set of parameter values can be made for reentry behavior calculations with some degree of confidence. It is recommended that future arc-jet experiments on SNAP fuel material employ methods for evaluating hydrogen loss rates. If this is done, a more complete measure of correlation with the analytical description is afforded. Further, the use of the tungsten rod holder in these tests has not been found to introduce undue uncertainties in the results.

B. REENTRY RESULTS

Material response calculations have been made using the standard analytical model with the latest, standard set of parameter values (listed in Section VIII) for a reentering SNAP 10A fuel element in cross-axial-spinning, random-tumbling, and end-over-end flight orientations. Typical results of these calculations are presented in Figures 25 through 28, in which the transient behavior of the fuel surface temperature, average fuel temperature, average hydrogen content, and the cold-wall, average aerodynamic heat rate are shown.

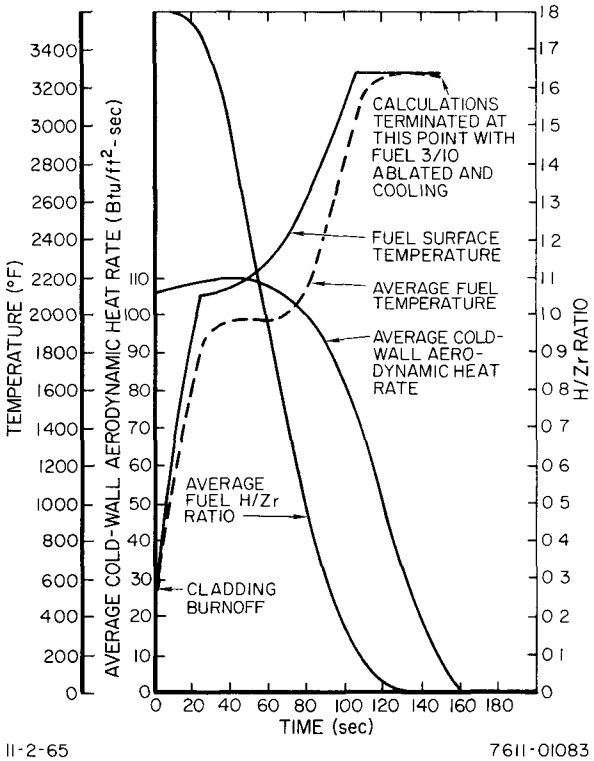

Figure 25. Reentry Behavior of a SNAP 10A Fuel Element Tumbling at Random After Release From 232,000 ft

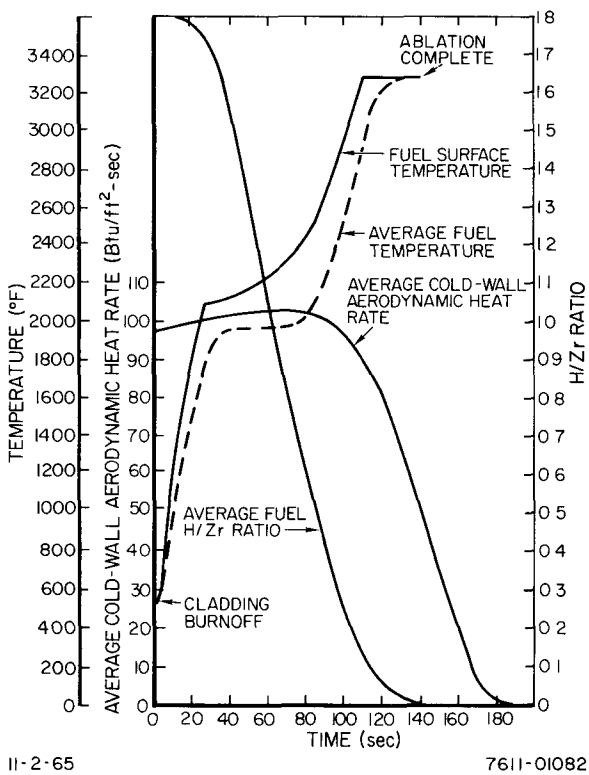

Figure 26. Reentry Behavior of a SNAP 10A Fuel Element Spinning Cross Axially After Release From 250,000 ft

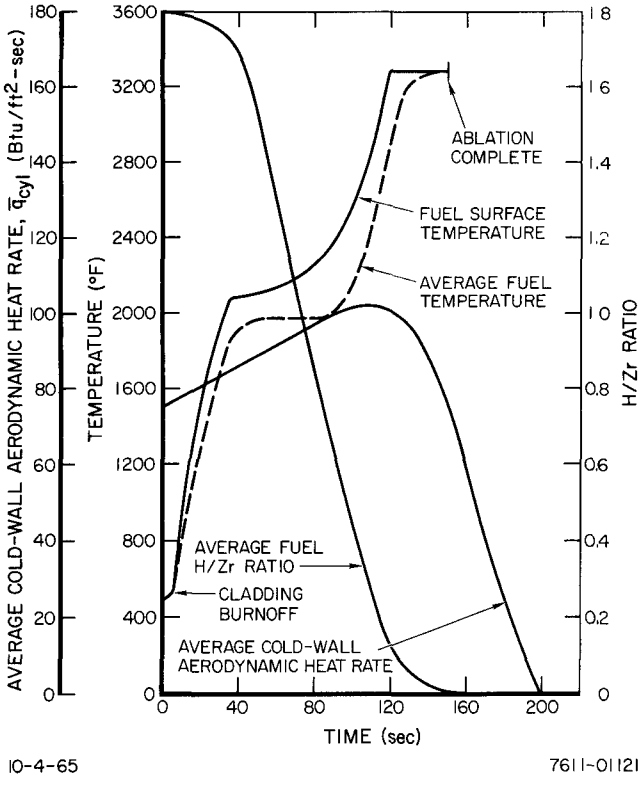

Figure 27. Reentry Behavior of a SNAP 10A Fuel Element Tumbling at Random After Release From 250,000 ft

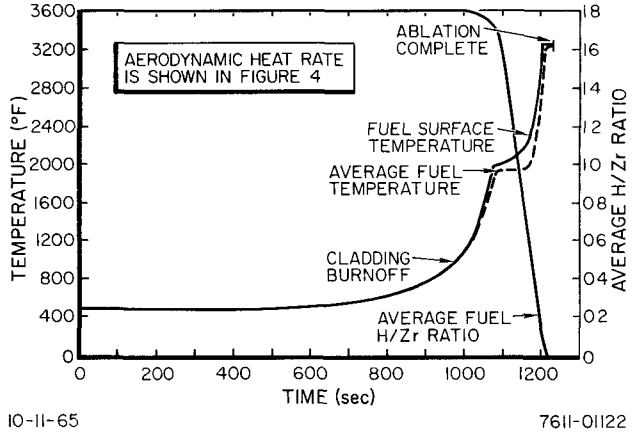

Figure 28. Reentry Behavior of a SNAP 10A Fuel Element Tumbling at Random After Release From 400,000 ft

A set of calculations was performed for various release altitudes and initial temperatures to define the minimum release altitudes for which complete ablation of the fuel material is attained. Curves of these minimum release altitudes as functions of initial temperature are shown in Figure 29 for all flight orientations considered. These results indicate that the ranges of initial release altitude that are just sufficient to attain complete burnup, assuming correct input parameter values, can be given as:

1) 245,000 to 252,000 ft for cross-axial spinning

2) 238,000 to 245,000 ft for end-over-end tumbling

3) 234,000 to 241,000 ft for random tumbling.

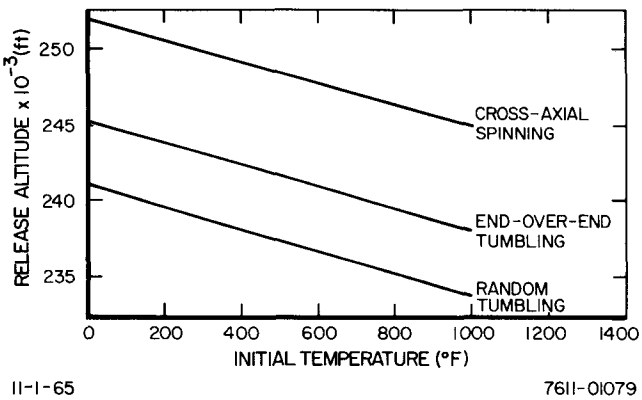

Figure 29. Minimum Fuel Element Release Altitude to Attain Burnup vs Initial Temperature

These ranges are appropriate for a 0 to 1000°F range in initial temperatures. Further, they reflect the approximate procedure for simulation of the ablation process. As such, they are considered to be preliminary and subject to further refinement following improved analytical methods and factoring-in of subsequent experimental data.

The trajectory parameters and conditions of the fuel element at the time of initial ablation are of interest for analytical and experimental investigations of fuel particle behavior. Such conditions include the flight angle, altitude, and velocity. For fuel element behavior calculations in which the latest, standard set of parameter values was used, the conditions at the time of initial ablation are listed in Table 6 for various release altitudes for a cross-axial, spinning orientation. The corresponding conditions for a random-tumbling orientation are given in Table 7. It was found that, for all release altitudes in which melting is attained, the fuel element altitudes at the time of initial melting range from 174,000 to 230,000 ft for a cross-axial, spinning orientation and from 162,000 to 230,000 ft for elements tumbling at random. For a typical, probable case (release altitude = 242,000 ft; random-tumbling orientation), the fuel begins to melt at about 185,000 ft and is completely ablated at about 155,000 ft.

From planned experimental and analytical investigations of the ablation process (shearing forces, flow-off mechanism, etc.), information will be sought regarding the sizes of the ablated particles. With such information to supplement data on the conditions at the time of melting, fuel particle behavior studies can be put on a quantitative basis.

TABLE 6

CONDITIONS AT TIME OF INITIAL MELTING FOR A SNAP 10A FUEL ELEMENT SPINNING CROSS-AXIALLY

Release Altitude (ft)	Time After Release (sec)	Velocity (ft/sec)	Altitude (ft)	Flight Angle (degrees of arc)
400,000	1,105.0	22,407	221,849	-1.96
350,000	578.7	21,340	221,566	-2.04
300,000	278.7	21,912	229,380	-1.89
275,000	160.5	21,617	228,110	-1.84
260,000	123.8	19,776	213,024	-2.35
250,000	109.6	17,550	197,560	-3.06
245,000	108.8	15,627	186,192	-3.77

TABLE 7

CONDITIONS AT TIME OF INITIAL MELTING FOR A SNAP 10A FUEL ELEMENT TUMBLING AT RANDOM

Release Altitude (ft)	Time After Release (sec)	Velocity (ft/sec)	Altitude (ft)	Flight Angle (degrees of arc)
400,000	1,199.7	22,504	221,620	-1.66
350,000	647.0	22,732	224,959	-1.63
300,000	315.4	22,959	229,950	-1.58
275,000	184.5	22,343	223,402	-1.71
260,000	138.9	21,075	209,588	-2.08
250,000	119.4	19,494	196,124	-2.58
242,000	109.6	17,929	184,916	-3.08
232,000	105.6	14,825	166,223	-4.22

VIII. STATISTICAL ANALYSIS

A. OUTLINE AND METHOD

As the development of the analytical model became complete, reentry computations were made for a variety of initial conditions and parameter values. To organize and categorize the results, a program of statistical analysis was undertaken. In this program, the integrated aerodynamic heat necessary to initiate fuel ablation and the integrated aerodynamic heat available in the fuel element trajectory are evaluated and compared. The evaluations are made for the entire range of reasonable (within 95% probable) parameter values and initial conditions. The comparisons are made for various release altitudes and flight orientations.

The specific objectives of the overall statistical program are numerous, and can be listed as follows:

1) Determine the change in the resulting analytical solution due to a perturbation in any given input parameter

2) Tabulate those parameters which most strongly influence the analytical solutions

3) Define the parameters which are requisite of further experimental refinement according to the criterion of effective elimination of uncertainties in the analytical solutions

4) Calculate the composite range of deviation in the integrated aerodynamic heat necessary to initiate ablation due to the range of deviation in each input parameter

5) For each release altitude, calculate the composite range of deviation in the integrated aerodynamic heat available in the fuel element trajectory due to the range of deviation in each trajectory parameter

6) Utilizing the results achieved from objectives 4 and 5, calculate the probabilities of initial fuel melting for various release altitudes and modes of reentry.

The overall statistical program is outlined in flow-chart form in Figure 30. The focal point of the program is shown in Figure 30 to be the calculation of the probability of initial fuel ablation for each release altitude, although the other objectives listed above are also of interest. Such probabilities are presented in this report based on present available parameter data. Preliminary probabilities are calculated in paragraph B of this section for a preliminary set of input parameters and for a cross-axial, spinning, fuel element flight orientation. A more complete and refined set of input parameters was then used to generate probabilities in Paragraph C for both cross-axial-spinning and random-tumbling reentry modes. Future extensions of this statistical program are planned to encompass probabilities of complete fuel element ablation based on supplementary experimental and analytical investigations of the ablation process

The method employed in the statistical analysis is based on the Law of Propagation of Errors.[65] In deriving this law, one defines

$$Y = F(X_1, X_2, \ldots, X_i, \ldots, X_m)$$

as the functional relationship between the quantity Y to be calculated and the m other quantities upon whose values the calculated value of Y depends.

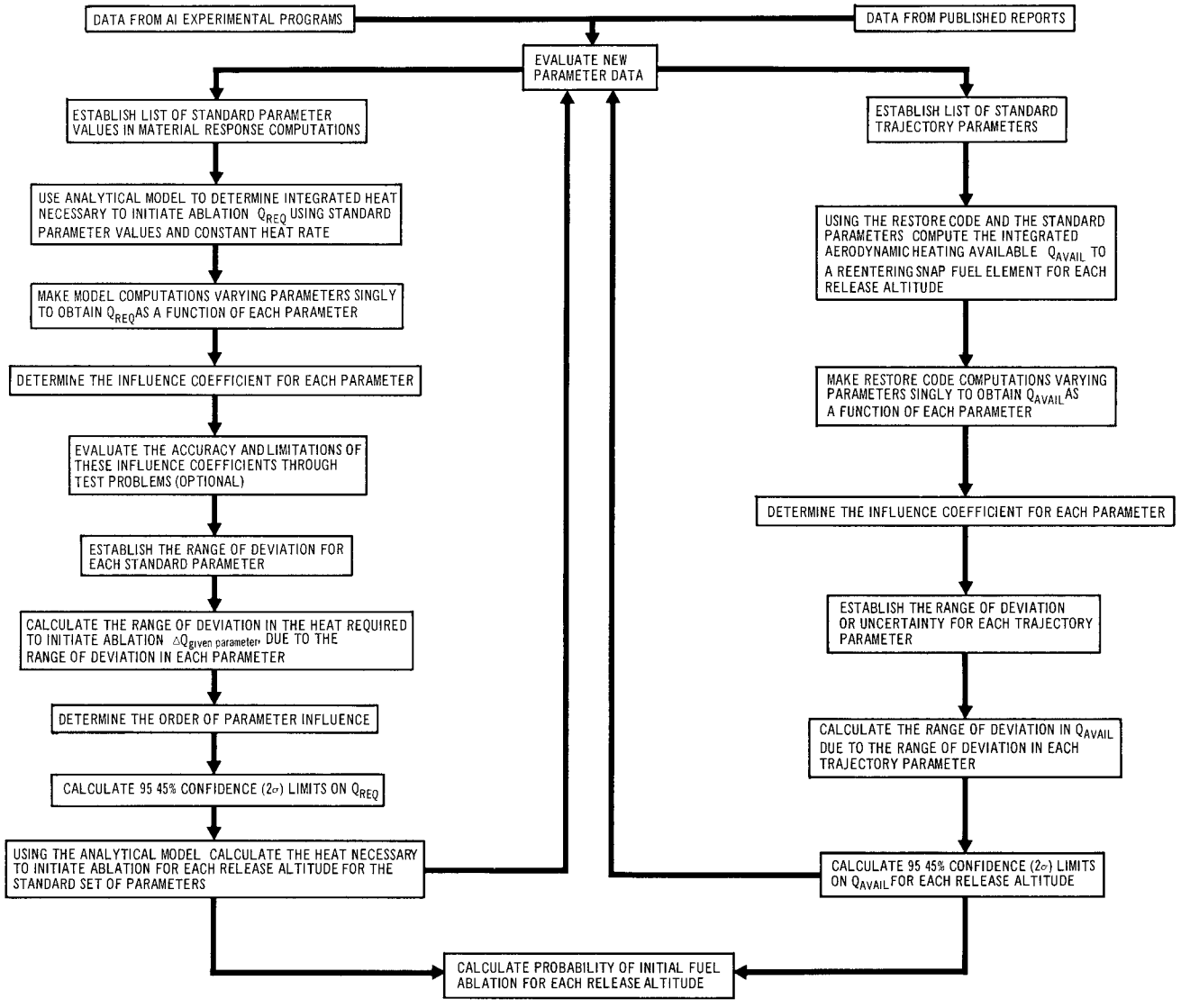

11-22-65 7611-01123

Figure 30. Program of Statistical Analysis

Assuming that F can be expanded in a Taylor's series and neglecting products of errors in comparison with the errors themselves we have:

$$dY = \frac{\partial F}{\partial X_1} dX_1 + \frac{\partial F}{\partial X_2} dX_2 + \ldots + \frac{\partial F}{\partial X_m} dX_m \quad . \qquad \ldots(49)$$

For small finite increments about a particular reference case, $\Delta Y = \overline{Y} - Y$ and $\Delta X_i = \overline{X}_i - X_i$, Equation 49 may be written as follows:

$$\Delta Y = \frac{\partial F}{\partial X_1} \Delta X_1 + \frac{\partial F}{\partial X_2} \Delta X_2 + \ldots + \frac{\partial F}{\partial X_m} \Delta X_m \quad , \qquad \ldots(50)$$

where

$$\overline{Y} = F(\overline{X}_1, \overline{X}_2, \ldots, \overline{X}_m) \quad ,$$

the mean or reference value of Y calculated using the complete set of mean or most probable parameter values, $\overline{X}_i$.

If σ_i is the standard deviation of the measurement of X_i, then the standard deviation of the calculated value of Y is given by

$$\sigma_y = \sqrt{A_1^2 \sigma_1^2 + A_2^2 \sigma_2^2 + \ldots + A_m^2 \sigma_m^2} \quad , \qquad \ldots(51)$$

where

$$A_i = \frac{\partial F}{\partial X_i} \quad ,$$

the influence coefficient of the parameter, X_i. The standard deviation, σ_i, is defined by the equation

$$\sigma_i = \sqrt{\frac{\sum_{j=1}^{m} (X_j - \overline{X})_i^2}{m}} \quad .$$

Equation (51) is called the general law for propagation of errors, and gives us the determination of the effect of deviations of measurement in each of the m quantities upon the standard deviation of the calculated values of Y. For a normal distribution of all possible values of Y, 68.27% of all values are included between $\overline{Y} - \sigma_y$ and $\overline{Y} + \sigma_y$. Likewise, 95.45% of the values are included between $\overline{Y} - 2\sigma_y$ and $\overline{Y} + 2\sigma_y$ and 99.73% of the values are included between $\overline{Y} - 3\sigma_y$ and $\overline{Y} + 3\sigma_y$.[66]

For the following statistical analysis, calculation of the standard deviations of the input parameters, according to the defining expression was prohibitive; consequently, an indirect approach was taken in which an upper and a lower bound was assigned to all measurements of a particular parameter so that these bounds would embrace 95.45% of all the available measurements. The range within these bounds is then equivalent to a normal distribution with $\pm 2\sigma_i$ limits on the standard mean value. The standard deviation, σ_i, can then be calculated knowing this range.

B. PRELIMINARY ANALYSIS

1. Determination of Q_{REQ} and Corresponding Confidence Limits

A preliminary analysis was made to develop the methods discussed and to obtain a first-cut realization of the objectives listed previously. A preliminary set of standard reference parameter

values and initial conditions was used for the analytical model to give each subsequent case investigated a common basis of comparison.

Using the Law of Propagation of Errors, influence coefficients were developed for specific heat, heat of hydrogen dissociation, emissivity, initial temperature, initial hydrogen concentration, diffusion coefficient, heat of oxidation, thermal conductivity, aerodynamic heating, outside fuel element radius, and air-stream stagnation enthalpy.

The initial reference parameter values with 2σ deviations (twice the standard deviations) are given in Table 8.

TABLE 8

STANDARD SET OF PARAMETERS WITH 2σ CONFIDENCE LIMITS FOR THE PRELIMINARY ANALYSIS

q_{ox}	= f(t) (see Figure 8) ± factor of 1
ϵ	= 0.4 ± 0.15
H/Zr_1	= 1 8 ± 0.05
T_1	= 300 ± 300°F
k	= 13.3 ± 5.0 Btu/hr-ft-°F
H_{diss}	= -36,000 ± 3600 Btu/lb of H_2 for the delta-epsilon phase region
	= -45,900 ± 4590 Btu/lb of H_2 for the $\beta + \delta$ phase region
	= -36,000 ± 3600 Btu/lb of H_2 for the beta phase region
R_o	= 0.625 ± 0.005 in.
H_s	= 10,000 ± 2500 Btu/lb of air
D	= f(T) (see Figure 16) ± factor of 10
C_p	= f(H/Zr, T) (see Figure 14) ±10%

These values were considered to be the most appropriate, at the beginning of this study, for a SNAP fuel element under reentry conditions.

To make the influence coefficients independent of trajectory, a constant cold-wall average aerodynamic heat rate, q_{cyl} = 100.0 Btu/ft^2-sec, was used. The integrated heat necessary to initiate ablation, Q_{REQ}, for the analytical model with the reference (standard set) parameter values was found to be 12,100 Btu/ft^2. That is, for a constant q_{cyl} = 100 Btu/ft^2-sec, the fuel begins melting at 121 sec

The regions in which the various parameters affect the heat necessary for ablation are schematically shown in Figure 31.

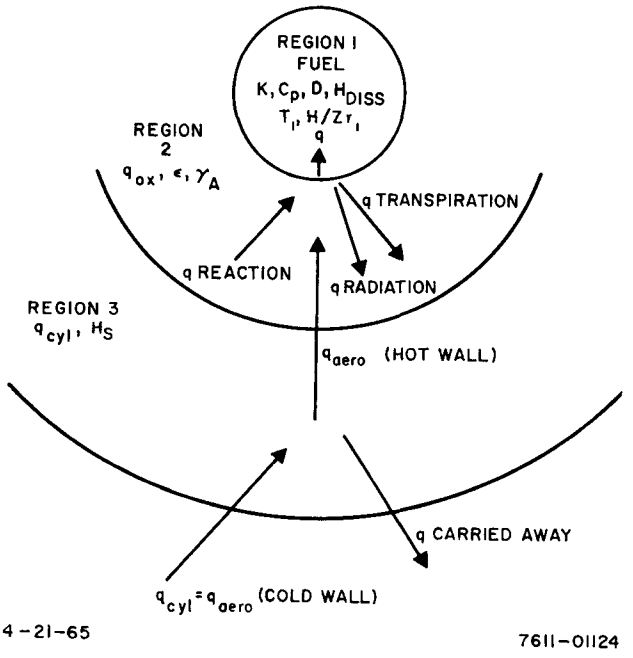

Figure 31. Regions of Influence on Reentering Fuel Element of Parameters Investigated

According to the Law of Propagation of Errors, let

$$Q_{REQ} = f(q_{ox},\ \epsilon,\ H/Zr_1,\ T_1,\ k,\ H_{diss},\ D,\ C_p,\ R_o,\ H_s) \qquad \ldots(52)$$

be the functional relationship between Q_{REQ} and the parameters upon whose measurements the calculated value of Q_{REQ} depends.

Assuming that f can be expanded in a Taylor's series and by neglecting products of errors in comparison with the errors themselves, it follows that its differential is

$$dQ_{REQ} = \left(\frac{\partial Q_{REQ}}{\partial q_{ox}}\right)dq_{ox} + \left(\frac{\partial Q_{REQ}}{\partial \epsilon}\right)d\epsilon + \left(\frac{\partial Q_{REQ}}{\partial (H/Zr)_1}\right)d(H/Zr)_1 + \ldots, \qquad \ldots(53)$$

where $\partial Q_{REQ}/\partial q_{ox}$, etc., are the differentials of $Q_{REQ} = f$.

The standard deviation of Q_{REQ} may be calculated by

$$\sigma_{Q_{REQ}} = \sqrt{\left(\frac{\partial Q_{REQ}}{\partial q_{ox}}\right)^2 \sigma_{q_{ox}}^{\ 2} + \left(\frac{\partial Q_{REQ}}{\partial \epsilon}\right)^2 \sigma_{\epsilon}^{\ 2} + \left(\frac{\partial Q_{REQ}}{\partial (H/Zr)_1}\right)^2 \sigma^2_{(H/Zr)_1} + \ldots}, \qquad \ldots(54)$$

where $\sigma_{q_{ox}}$, σ_{ϵ}, $\sigma_{(H/Zr)_1}$, etc., are the standard deviations of the given parameters.

In Equations 53 and 54, $\partial Q_{REQ}/\partial q_{ox}$, $\partial Q_{REQ}/\partial \epsilon$, etc., are the influence coefficients for the given parameters. For each parameter, several computer runs were made varying the given parameter over a range of probable values, holding all other parameters the same as in the standard case. From the results of the various computer runs in which the parameters were

varied singly, it was possible to obtain an equation for the heat necessary to initiate ablation as a function of the individual parameters, i.e., Q_{REQ} = f (given parameter). The influence coefficient for the given parameter is then simply the derivative of this relationship.

In order to find the influence coefficient for the radius of the fuel element, it was necessary to approximate cladding thicknesses for fuel elements other than SNAP 8 and SNAP 10A. Unclad fuel elements of radii 0.1, 0.265, 0.3125, and 0.606 in were analyzed to obtain the general shape of a curve representing Q_{REQ} = f (radius). By comparing this curve to the difference in heat required to initiate ablation of clad and unclad SNAP 8 and 10A fuel elements and extrapolating to zero, it was possible to approximate the value of Q_{REQ} for clad fuel elements of fuel radii 0.1 and 0.3125 in The approximate cladding thicknesses for the 0.1-in. and 0.3125-in. radius fuel rods are 0 005 and 0.012 in., respectively.

In the cases of q_{ox}, C_p, and D, the internally computed values were increased or decreased by a given percentage to establish the influence on Q_{REQ}. In essence, this was the same as raising or lowering the plots of q_{ox}, C_p, and D (see Figures 8, 14, and 16) by the given percentage. Since the values of q_{ox}, C_p, and D are not constant, it was necessary to use ratios when calculating these influence coefficients. The ratios used were the percentage of the standard value for each case to the standard value which was taken as one. For example, if C_p were lowered 10%, the ratio for that given case would be 0.90/1.00.

To maintain consistency in Equations 53 and 54, ratios or factors were used for all properties and calculated values of Q_{REQ} The factor for a given parameter is defined as

$$F_{(\text{given parameter})} = \frac{\text{given parameter's value for each case}}{\text{standard parameter value}} .$$

In terms of parameter ratios, Q_{REQ} = f (given parameter) becomes FQ_{REQ} = f (factor of given parameter). The latter equation is then differentiated with respect to the parameter ratio in question to obtain the influence coefficients to be substituted into Equation 54.

Figure 32 shows FQ_{REQ} as a function of the ratio of each parameter investigated to its corresponding standard value.

The influence coefficients for the various parameters, in terms of parameter factors, are given in Table 9.

Equation 53, in terms of the parameter ratios, was then integrated from $F_{standard}$ to the value of F of the parameter in question to obtain the general influence equation for all parameters The influence coefficient equation, after integration becomes

Term in Equation	Corresponding Parameter
$FQ_{REQ} - 1.0 = +0.245\ (F_{\epsilon} - 1.0)$	Fuel emissivity
$-0.0648\ (Fq_{ox} - 1.0)$	Heat of oxidation
$+0.3785\ (F_{C_p} - 1.0)$	Fuel specific heat
$-0.03189\ (FT_1 - 1.0)$	Initial temperature
$+0.5775\ (F_{H_{diss}} - 1.0)$	Hydrogen heat of dissociation

Term in Equation	Corresponding Parameter
$+1.0\ (F_{R_o}-1.0)$	Outside fuel element radius
$+1.63\ (e^{-6.426}-e^{-6.426\ F_k})$	Fuel thermal conductivity
$+0.472\ (e^{-5.86}-e^{-5.86\ F_D})$	Hydrogen diffusion coefficient
$-0.32\ (F_{H_s}-1.0)+0.16(F_{H_s}^2-1.0)$	Air-stream stagnation enthalpy.

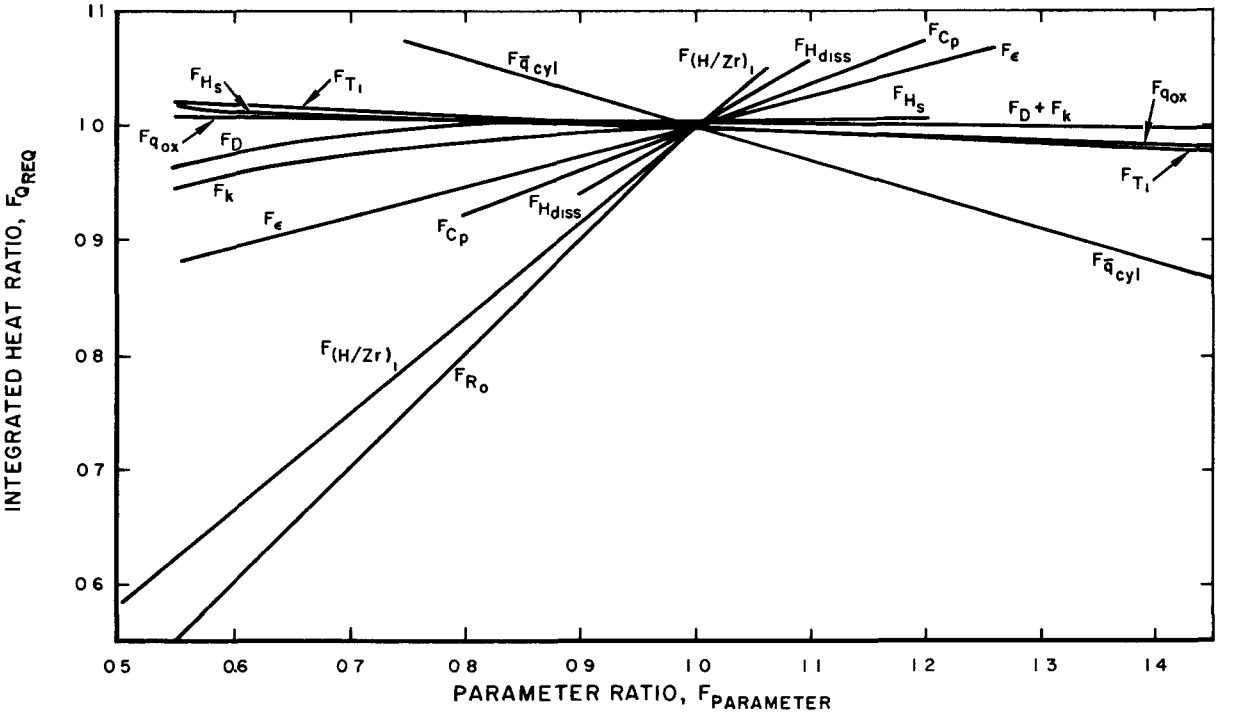

4-21-65

7611-01125

Figure 32. Parameter Ratio vs Integrated Heat Ratio

TABLE 9

INFLUENCE COEFFICIENTS FOR PARAMETERS IN PRELIMINARY CALCULATION OF Q_{REQ}

Parameter	Influence Coefficient
Fuel emissivity	+0.245
Heat of oxidation	-0.0648
Fuel specific heat	+0.3785
Initial temperature	-0.03198
Initial hydrogen concentration	+0.845
Hydrogen heat of dissociation	+0.5775
Outside radius of fuel element	+1.0
Fuel thermal conductivity	$+10.474\ e^{-6.426\ F_k}$
Hydrogen diffusion coefficient	$+2.762\ e^{-5.86\ F_D}$
Air-stream stagnation enthalpy	$-0.32 + 0.32\ F_{H_s}$

Two series of test problems were made to determine the accuracy of the influence coefficients and to investigate cross-coupling effects. In both series, two parameters were varied simultaneously and the influence coefficients were used to predict the corresponding value of Q_{REQ}. To predict a value of Q_{REQ} for a given change in one or two parameters, the values of the parameter factors, $\frac{\text{given parameter value}}{\text{standard parameter value}}$, must be substituted into the corresponding terms in the general influence equation. All other terms, on the right side of the general equation, become zero and may be neglected. FQ_{REQ} is then evaluated. The heat necessary to initiate ablation, for the given case, is (FQ_{REQ}) (12,100) Btu/ft^2. The parameter values used in each test problem were substituted into the analytical model to determine the actual value of Q_{REQ} for that test problem. The percentage error of prediction given for each test problem is defined as:

$$\text{Percentage error of prediction} = \frac{\text{Predicted } Q_{REQ} - \text{Calculated } Q_{REQ}}{\text{Calculated } Q_{REQ}}.$$

The first series of test problems was designed to determine the accuracy of the influence coefficients when wide variations of parameters were used. Table 10 gives the parameters changed, the values of the changed parameters, predicted and calculated Q_{REQ}, and per cent error of prediction for each test problem in the first series.

TABLE 10

RESULTS OF THE FIRST SERIES OF TEST PROBLEMS

Problem	Parameters Varied and Values Used	Predicted Q_{REQ} (Btu/ft^2)	Calculated Q_{REQ} (Btu/ft^2)	Error of Prediction (%)
1	$H/Zr_i = 1.6$ $k = 11.0$ Btu/hr-ft-°F	10,254.0	10,148.8	1.035
2	$H/Zr_i = 1.6$ $T_i = 500.0$°F	10,064.0	10,057.3	0.07
3	$\epsilon = 0.3$ $D = 0.75$ (standard value)	10,634.0	10,448.4	1.78
4	$\epsilon = 0.3$ $C_p = 0.80$ (standard value)	9,823.0	9,862.0	0.395
5	$k = 11.0$ Btu/hr-ft-°F $D = 0.75$ (standard value)	11,269.0	11,177.6	0.815
6	$H_{diss} = 0.90$ (standard value) $C_p = 1.2$ (standard value)	11,586.0	11,485.0	0.863
7	$R_o = 0.280$ in. $H/Zr_i = 1.7$	4,564.0	4,714.0	3.16

In Table 10, all parameters in addition to those varied in a given test problem are the same as the reference values listed in Table 8.

Since values of q_{ox}, D, C_p, and H_{diss} are internally computed by means of the TAP-3 analytical model, they are varied by multiplying the computed value by a given fraction. In all cases investigated in the first series, calculated and predicted values of Q_{REQ} were lower than the reference value of Q_{REQ} (12,100 Btu/ft^2). The variations in the Q_{REQ} for the first series ranged from 0.38 to 0.95 times the reference value of Q_{REQ}. From Table 10 it can be seen that in almost all cases, the highest error of prediction occurred in those test problems with the largest reduction of Q_{REQ}.

It is felt that if there are wide variations of parameters or if three or more parameters are varied at a given time, then cross influence between parameters will become appreciable and introduce large errors into the predicted value of Q_{REQ} for that case.

A second series of test problems was devised and analyzed to determine the accuracy of the influence coefficients around the reference case. Changes were made in the standard parameter values such that the variations in the ratios of integrated heats, FQ_{REQ}, were from 0.9865 to 1.0135 for each parameter. Parameters were varied in such a manner that one parameter change increased the required integrated heat ratio and the second parameter change lowered the ratio by approximately the same amount.

Since the parameters were varied in this way, the predicted value of Q_{REQ} for each test problem would be the same as that of the standard case, 12,100 Btu/ft^2. Table 11 gives the parameters changed, the values of the changed parameters, predicted and calculated Q_{REQ}, and the percent of error between the predicted and calculated values of Q_{REQ} for each test problem in the second series.

TABLE 11

RESULTS OF THE SECOND SERIES OF TEST PROBLEMS

Test Problem	Parameter Varied and Values Used	Predicted Q_{REQ} (Btu/hr2)	Calculated Q_{REQ} (Btu/hr2)	Error of Prediction (%)
1	ϵ = 0.422 C_p = 0.9670 (standard value)	12,100	12,140	0.33
2	k = 10.64 Btu/hr-ft-°F H/Zr_i = 1.826	12,100	12,140	0.33
3	T_i = 412.9°F H/Zr_i = 1.826	12,100	12,140	0.33
4	D = 0.68 (standard value) ϵ = 0.422	12,100	12,040	0.495
5	H_{diss} = 0.977 (standard value) C_p = 1.036 (standard value)	12,100	12,140	0.33
6	H_s = 7500.0 Btu/lb	12,100	12,040	0.495

A test problem was not analyzed in which both thermal conductivity and the hydrogen diffusion coefficient were varied, since neither parameter can be changed in such a way as to increase Q_{REQ}. (See Section V for a discussion of the variance of Q_{REQ} as a function of thermal conductivity.)

From Table 11 it can be seen that for all cases investigated, the error between the predicted and calculated values of Q_{REQ} was less than 0.5%. Test problems 4 and 6 had the largest error. This may be attributed to the large change necessary in the parameter values used in these problems to change the heat required by a relatively small amount.

The range of deviation in Q_{REQ} was evaluated from estimated uncertainties in the corresponding individual parameters and the calculated influence coefficients of the parameters. The 2σ confidence limits which were chosen for each parameter are given in Table 8. These confidence limits are assumed to encompass 95.45% of all probable values for each parameter. Maximum and minimum values of the uncertainty range for each parameter were substituted into the corresponding term in the integrated influence equation given previously. One-half of the difference between the values of Q_{REQ} for the maximum and minimum parameter values for each parameter is (ΔQ_{REQ}) given parameter. This is the range of error in the heat necessary to initiate ablation due to the range of error in a particular parameter. The 2σ confidence limits for Q_{REQ}, in terms of the ΔQ_{REQ} values of the parameters involved, are

$$2\sigma_{Q_{REQ}} = \sqrt{\left(\Delta Q_{REQ}\right)^2_{q_{ox}} + \left(\Delta Q_{REQ}\right)^2_{\epsilon} + \left(\Delta Q_{REQ}\right)^2_{H/Zr_i} + \ldots .} \quad . \qquad \ldots(55)$$

Values of ΔQ_{REQ} for each parameter are given in Table 12.

TABLE 12

DEVIATIONS IN Q_{REQ} DUE TO $\pm 2\sigma$ DEVIATIONS IN THE PRELIMINARY SET OF STANDARD PARAMETER VALUES

Parameter	ΔQ_{REQ} (Btu/ft^2)
D	1575
ϵ	1112
q_{ox}	784
H_{diss}	699
C_p	458
T_i	386
H/Zr_i	282
k	161
R_o	97
H_s	61

Parameters in Table 12 are listed in order of the largest effect upon Q_{REQ}. The values of ΔQ_{REQ} for the various parameters reflect the combination of the parameter's influence upon Q_{REQ} and the confidence with which the parameter values are known. These values were substituted into Equation 54, which was then solved to obtain the value of $2\sigma_{Q_{REQ}} = 2300$ Btu/ft^2. The standard deviation is then half of this value. For the preliminary reference case, $Q_{REQ} \pm \sigma_{Q_{REQ}}$ is then 12,100 ± 1150 Btu/ft^2.

The confidence limits for Q_{REQ} are constant for all release altitudes since they are independent of heat input. The integrated heat necessary to initiate ablation for the reference model will vary with release altitude and with the mode of reentry for any given release altitude. This is due to the influence of the heating rate upon Q_{REQ}. The influence coefficient for $\bar{q}_{cyl}$ has been calculated to be $+0.0505 - 0.6222\ F_{q_{cyl}} + 0.263\ F^2_{q_{cyl}}$, and is shown in Figure 32.

Aerodynamic heating rates obtained from the RESTORE trajectory code (see Section IV) were substituted into the analytical fuel element model to determine the value of Q_{REQ} for various release altitudes from 200,000 to 400,000 ft.

The total available heat over the trajectory, Q_{AVAIL}, obtained from each run is the cold-wall heat rate ($\bar{q}_{cyl}$) integrated from the instant of release to the time at which it reached a value of 52 Btu/ft^2-sec. This value was used since it approximates a point when the heating rate is balanced by the radiation loss from the surface of the fuel element.

Values of Q_{REQ} and $\sigma_{Q_{REQ}}$ for each release altitude considered are given in Paragraph B.3 of this section.

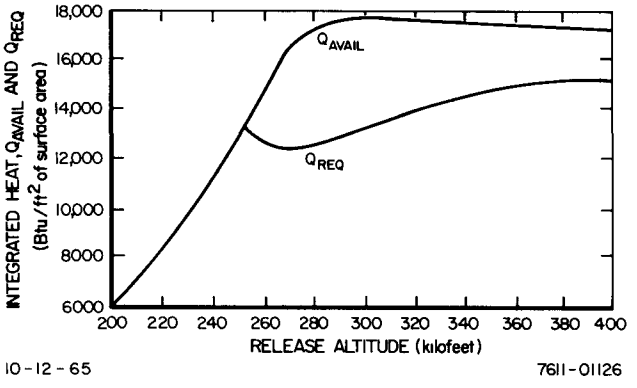

Figure 33. Q_{AVAIL} and Q_{REQ} vs Release Altitude for a SNAP 10A Fuel Element Spinning Cross-Axially, Using the Preliminary Set of Reference Parameters

Figure 33 shows Q_{AVAIL} and Q_{REQ} as a function of release altitude for the analytical model, using the preliminary set of reference values for a cross-axial-spinning mode of reentry.

2. Determination of Confidence Limits for Q_{AVAIL}

The second phase of the preliminary analysis was to determine the influence of certain trajectory parameters on the integrated aerodynamic heat available (Q_{AVAIL}) to a reentering SNAP 10A fuel element. The trajectory parameters of significant influence were the ballistic coefficient (W/C_DA_p), velocity (v), and flight-path angle (γ).

Using the trajectory code RESTORE, a series of computer runs was made to determine the influence coefficients for the above parameters. Fuel element release altitudes from 200,000 to 400,000 ft were considered. The parameters (W/C_DA_p, v, and γ) were varied, at each altitude, above and below reference or standard values taken from the reference parent vehicle trajectory.

A constant deviation of ±3 lb/ft^2, from the standard ballistic coefficient value, was used as the most probable range of values. This 2σ deviation was arrived at after assigning a ±15% deviation to the standard drag coefficient values calculated in Appendix A.

In order to determine probable deviations in the release velocity and flight angle, the Lockheed report[5] on SNAP 10A Agena reentry trajectories was surveyed. By comparing parent vehicle velocities and flight angles for different altitudes presented in Reference 5 with corresponding standard (see Figure 1) values, probable ranges of deviation were obtained for fuel element release velocities and flight angles. These deviations are shown in Table 13 for selected release altitudes.

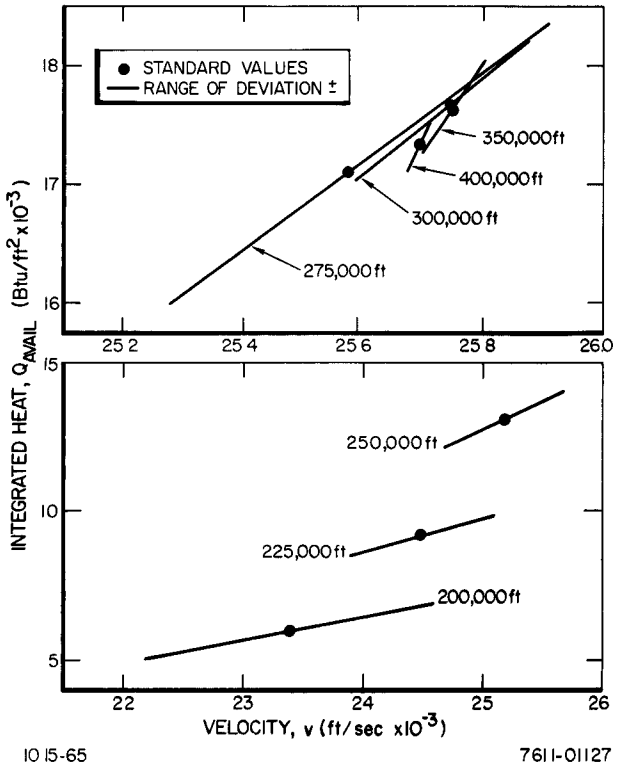

Figure 34. Influence of Velocity on Heat Available to Reentering SNAP 10A Fuel Element in Cross-Axial Flow

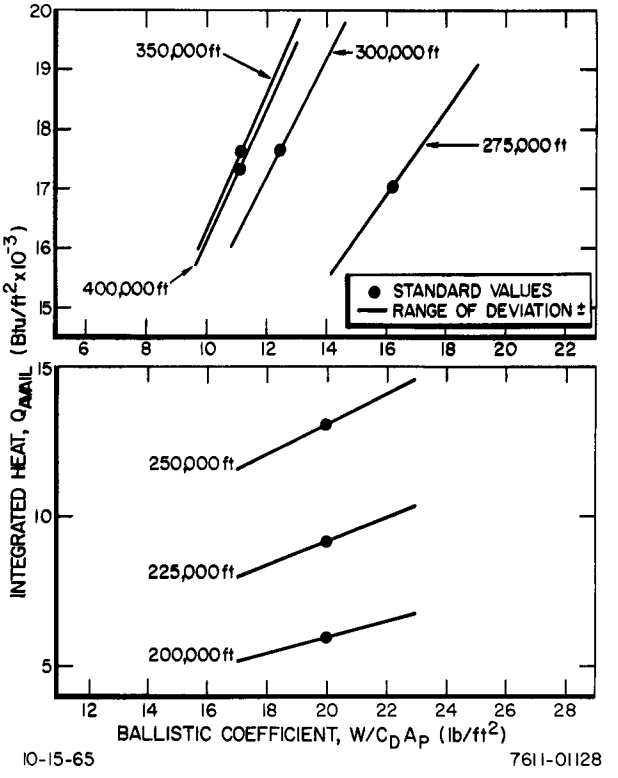

Figure 35. Influence of Ballistic Coefficient on Heat Available to Reentering SNAP 10A Fuel Element in Cross-Axial Flow

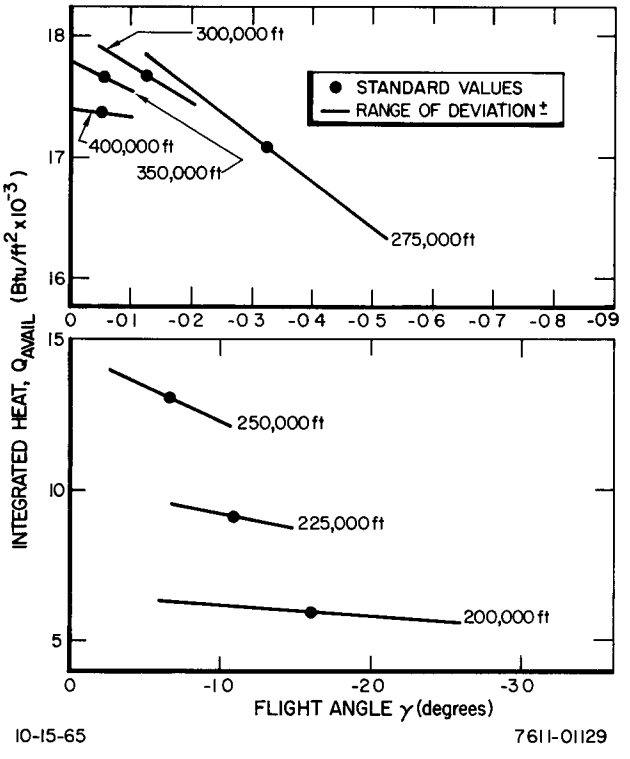

Figure 36. Influence of Flight Path Angle on Heat Available to Reentering SNAP 10A Fuel Element in Cross-Axial Flow

TABLE 13

RESULTS OF THE PARAMETER SURVEY FOR Q_{AVAIL} FOR CROSS-AXIAL, SPINNING SNAP 10A FUEL ELEMENTS

Release Altitude (ft)	Influence Coefficients			Deviations (2σ)			Standard Values		
	$\frac{\partial Q_{AVAIL}}{\partial v}$	$\frac{\partial Q_{AVAIL}}{\partial (W/C_D A_p)}$	$\frac{\partial Q_{AVAIL}}{\partial \gamma}$	v (ft/sec)	$W/C_D A_p$ (lb/ft^2)	γ (degrees)	v (ft/sec)	$W/C_D A_p$ (ft/sec^2)	γ (degrees)
200,000	0.753	266.6	-370.4	±1200	±3.0	±1.0	23,379	20	-1.6030
225,000	1.138	391.5	-962.0	±600	±3.0	±0.4	24,487	20	-1.0831
250,000	1.818	507.0	-2940.0	±500	±3.0	±0.4	25,179	20	-0.6621
275,000	3.55	710.0	-3850.0	±300	±2.44	±0.2	25,578	16.3*	-0.3240
300,000	3.89	981.0	-3000.0	±160	±1.87	±0.08	25,746	12.5*	-0.1252
350,000	7.45	1140.0	-2380.0	±50	±1.68	±0.05	25,749	11.2*	-0.0531
400,000	11.11	1100.0	-862.5	±20	±1.67	±0.05	25,694	11.1*	-0.05

*Initial value

The influence of the three parameters, v, $W/C_D A_p$, and γ, on the integrated heat, Q_{AVAIL}, is shown in Figures 34 through 36. The differential of the heat available as a function of these parameters has the same form as Equation 52:

$$dQ_{AVAIL} = \frac{\partial Q_{AVAIL}}{\partial v} dv + \frac{\partial Q_{AVAIL}}{\partial (W/C_D A_p)} d(W/C_D A_p) + \frac{\partial Q_{AVAIL}}{\partial \gamma} d\gamma \quad , \qquad \ldots(56)$$

where $(\partial Q_{AVAIL}/\partial v)$ is the influence coefficient of the velocity (for example), holding all the other parameters at the standard value, and dv is the change in the velocity which is multiplied by its influence coefficient. Within the limits of the deviation in the parameters at each altitude, influence coefficients were determined and are listed in Table 13.

The ranges of deviation in Q_{AVAIL} were evaluated from estimated uncertainties in the corresponding individual parameters and the calculated influence coefficients of the parameters.

The maximum and minimum values within the uncertainty range for each parameter were substituted into the corresponding term in the influence equation. One-half of the difference between the values of Q_{AVAIL} for the maximum and minimum values for each parameter is (ΔQ_{AVAIL}) given parameter. This is the range of deviation in the heat available at each release altitude due to the range of deviation in a particular parameter.

The confidence limits of the heat available for a given release altitude, in terms of the standard deviations of the parameters involved, may be written as:

$$2\sigma Q_{AVAIL} = \sqrt{(\Delta Q_{AVAIL})_v^2 + (\Delta Q_{AVAIL})_{W/C_D A_p}^2 + (\Delta Q_{AVAIL})_\gamma^2} \quad . \qquad \ldots(57)$$

The values of ΔQ_{AVAIL} for v, $W/C_D A_p$, and γ, in Equation 57, for each release altitude, are given in Table 14. Applying Equation 57, the overall 2σ limit for Q_{AVAIL} can then be obtained. The mean standard deviation, σ, for Q_{AVAIL} is then one-half of this value.

Values of $Q_{AVAIL} \pm \sigma_{Q_{AVAIL}}$ for each release altitude considered between 200,000 and 400,000 ft are given in Table 15.

TABLE 14

DEVIATIONS IN Q_{AVAIL} DUE TO $\pm 2\sigma$ DEVIATIONS IN THE TRAJECTORY PARAMETERS FOR CROSS-AXIAL, SPINNING SNAP 10A FUEL ELEMENTS

Release Altitude (ft)	$\left(\Delta Q_{AVAIL}\right)_v$ (Btu/ft^2)	$\left(\Delta Q_{AVAIL}\right)_{W/C_D A_p}$ (Btu/ft^2)	$\left(\Delta Q_{AVAIL}\right)_\gamma$ (Btu/ft^2)
200,000	904.0	799.8	-370.4
225,000	682.8	1174.5	-384.8
250,000	909.0	1521.0	-1176.0
275,000	1065.0	1733.0	-770.0
300,000	622.4	1838.4	-240.0
350,000	372.5	1914.0	-119.0
400,000	222.2	1835.0	-43.1

TABLE 15

Q_{REQ} AND Q_{AVAIL} WITH STANDARD DEVIATIONS AND PROBABILITIES OF INITIAL ABLATION FOR CROSS-AXIAL REENTRY USING THE PRELIMINARY SET OF REFERENCE PARAMETERS

Release Altitude (ft)	Q_{AVAIL} (Btu/ft^2)	$\sigma_{Q_{AVAIL}}$ (Btu/ft^2)	Q_{REQ} (Btu/ft^2)	$\sigma_{Q_{REQ}}$ (Btu/ft^2)	Probability of Initial Ablation
200,000	5951	±632	-	±1150	$>1.0 \times 10^{-7}$
225,000	9145	±706	-	±1150	0.003
250,000	13,065	±1064	-	±1150	0.33
253,000	13,625	±1075	13,625	±1150	0.50
275,000	17,025	±1087	12,447	±1150	0.998
275,000	17,025	±859	12,447	±1150	0.99925*
300,000	17,662	±978	13,110	±1150	0.9987
350,000	17,632	±977	14,830	±1150	0.968
400,000	17,346	±925	15,240	±1150	0.922

*Values used to calculate probability of initial ablation used in graphical approximation of probabilities for release altitudes below 253,000 ft. (See next section.)

3. Calculation of the Probabilities of Initial Ablation

With the determination of standard values of $Q_{AVAIL} \pm \sigma Q_{AVAIL}$ and $Q_{REQ} \pm \sigma Q_{REQ}$ normal frequency distributions for the integrated heat required to initiate ablation and the integrated heat available can be obtained using the equation,

$$G = \frac{h}{\sqrt{\pi}} \exp(-z^2 h^2) \quad ,$$

where $h = 1/\sigma\sqrt{2}$, and z = any arbitrary deviation from the mean or standard integrated heat Such frequency distributions are plotted in Figure 37 for a 275,000-ft release altitude. The fraction of overlapping area between these curves is a measure of the probability of initial ablation.

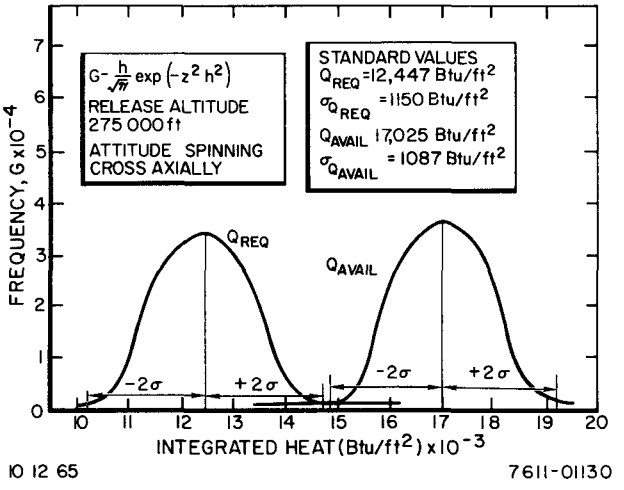

Figure 37. Normal Frequency Distribution for Q_{REQ} and Q_{AVAIL} for a SNAP 10A Fuel Element, Using the Preliminary Set of Reference Parameters

Given the standard values of $Q_{AVAIL} \pm \sigma Q_{AVAIL}$ and $Q_{REQ} \pm \sigma Q_{REQ}$, the probabilities of initial ablation for release altitudes considered can be calculated by means of the method discussed in Reference 67. Since this reference is not readily available, a brief description of the method used will be given. Let

$X = Q_{AVAIL}$,

$f(X)$ = the normal distribution of $Q_{AVAIL} \pm \sigma Q_{AVAIL}$

$Y = Q_{REQ}$, and

$f(Y)$ = the normal distribution of $Q_{REQ} \pm \sigma Q_{AVAIL}$.

Since $f(X)$ and $g(Y)$ are normal distributions, they will overlap. For each release altitude there is a distinct possibility that certain values of Q_{REQ} will exceed corresponding values of Q_{AVAIL} such that there is a probability that the fuel element will not ablate.

Simply stated, this probability is

$$P(\text{nonablation}) = P(Y>X) \quad .$$

From the theory of "linear combinations," it is found that

$$P(Y>X) = P(Y - X>0) \quad .$$

This suggests a new variable, $d = Y - X$, which has a mean value, $\mu_d = \mu_Y - \mu_X$ and variance,

$$\sigma_d^2 = \sigma_Y^2 + \sigma_X^2 \quad .$$

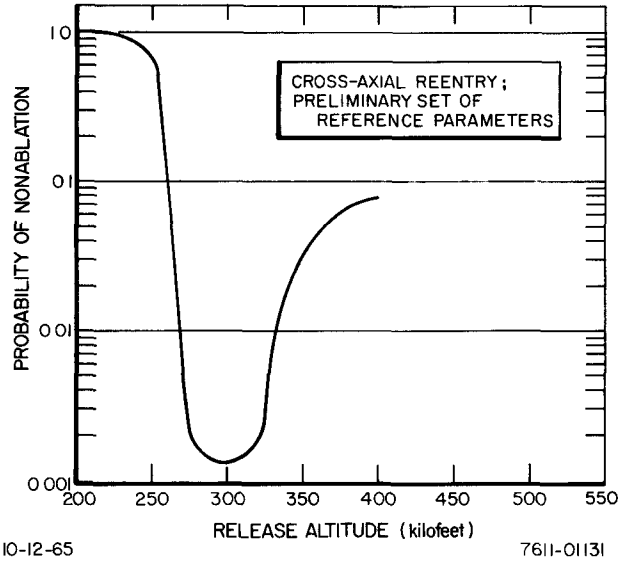

Figure 38. Probability of Survival (Nonablation) of a SNAP 10A Fuel Element vs Release Altitude

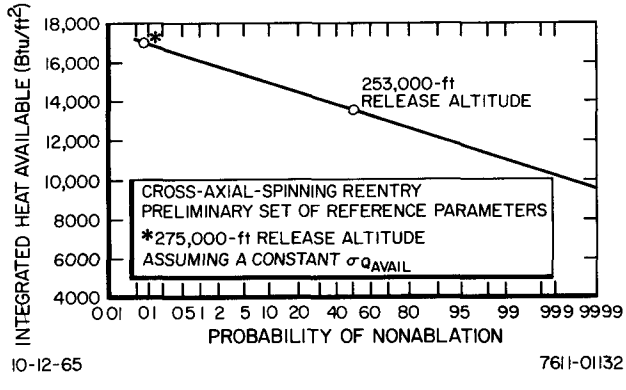

Figure 39. Approximate Probability of Initial Ablation for Release Altitudes Below 253,000 ft

Due to the fact that X and Y are independently and normally distributed, d is also normally distributed. In this case, the probability of nonablation is easily calculated, since μ_X, μ_Y, σ_X, and σ_Y are known.

In summary:

$$P(\text{nonablation}) = P(Y>X) = P(Y - X>0) = P(d>0),$$

$$P(d>0) = \text{the area of } f(d)>0,$$

$$P(\text{initial ablation}) = 1 - P(d>0).$$

By extrapolating the Q_{REQ} trace in Figure 33 from 255,000 ft to lower release altitudes, Q_{REQ} was found to equal Q_{AVAIL} at approximately 253,000 ft. Below this altitude, it is impossible to calculate a probability of initial ablation, since the heat required to initiate ablation cannot be obtained from the analytical model. This is obvious from Figure 33 which shows that melting is not predicted for release altitudes below 253,000 ft.

If the confidence limits on Q_{AVAIL} are assumed to be constant below 253,000 ft, it is possible to graphically approximate probabilities of initial ablation for release altitudes from 200,000 to 253,000 ft. From probability theory, it is known that a normal distribution with a constant σ limit will be a straight line when plotted on probability paper. A constant value of ±848.0 Btu/ft^2 was used for $\sigma_{Q_{AVAIL}}$ for release altitudes from 200,000 to 250,000 ft. This value is the average between $\sigma_{Q_{AVAIL}}$ at 200,000 ft and the value of $\sigma_{Q_{AVAIL}}$ for 250,000 ft. Since $\sigma_{Q_{REQ}}$ is a constant equal to ±1150.0 Btu/ft^2, and since $\sigma_d^2 = \sigma^2_{Q_{AVAIL}} + \sigma^2_{Q_{REQ}}$, σ_d is a constant equal to ±1022.5 Btu/ft^2.

Using this value of σ_d, the probability of initial ablation was calculated for a release altitude of 275,000 ft. The fact that the probability of initial ablation, where $Q_{REQ} = Q_{AVAIL}$, is 0.50 establishes a second point through which a straight line can be drawn on probability paper and extended to a release altitude of 200,000 ft.

The above calculation of the probability of initial ablation at 275,000-ft release altitude was only used to obtain a first point for the graphical approximation of probabilities below 253,000 ft. The probability at 275,000 ft quoted in Table 15 was calculated from actual values of $Q_{AVAIL} \pm \sigma_{Q_{AVAIL}}$ and $Q_{REQ} \pm \sigma_{Q_{REQ}}$ for that release altitude.

Values of Q_{AVAIL}, $\sigma_{Q_{AVAIL}}$, Q_{REQ}, $\sigma_{Q_{REQ}}$, graphically approximated probabilities of initial ablation for release altitudes from 200,000 to 253,000 ft, and calculated probabilities of initial ablation for release altitudes from 253,000 to 400,000 ft are all given in Table 15.

Figure 38 illustrates the probability of survival or nonablation (one minus the probability of ablation) of a SNAP 10A fuel element as a function of release altitude. Probabilities for release altitudes other than those given in Table 15 were calculated using interpolated $Q_{AVAIL} \pm \sigma_{Q_{AVAIL}}$ and $Q_{REQ} \pm \sigma_{Q_{REQ}}$ values. From Figure 38, it is evident that, based on the preceding calculations, the optimum release altitude for fuel ablation lies around 300,000 ft. Probabilities for survival rise sharply for release altitudes below 275,000 ft.

Figure 39 shows the graphical approximation used to obtain probabilities of initial ablation as a function of Q_{AVAIL} for release altitudes below 253,000 ft.

TABLE 16

DEVIATIONS IN Q_{REQ} DUE TO $\pm 2\sigma$ DEVIATIONS IN THE SECOND SET OF STANDARD PARAMETER VALUES

Parameter and Standard Value of Parameter	2σ Uncertainty Limit	ΔQ_{REQ} (Btu/ft^2)
D = 1.0	± factor of 10	1804
q_{oxid} = 1.0	± factor of 1	1403
*R_{γ_A} = 0.95	+0.05 -0.10	1021
ϵ = 0.4	±0.15	830
H_{diss} = 1.0	±10%	693
T_i = 500°F	±500°F	606
T_M = 3280°F	±200°F	462
C_p = 1.0	±10%	360
H/Zr_i = 1.80	±0.05	272
k = 13.3 Btu/hr-ft-°F	±5.0 Btu/hr-ft-°F	258
Analytical Solution	±6%	326
R_o = 0.625 in.	±0.005 in.	97
H_s = 10,000 Btu/lb	±2500 Btu/lb	38

*R_{γ_A} is defined as the ratio of the hot-wall aerodynamic heat rate for a noncatalytic surface (γ_A<1) to the corresponding heat rate for a fully catalytic surface (γ_A = 1).

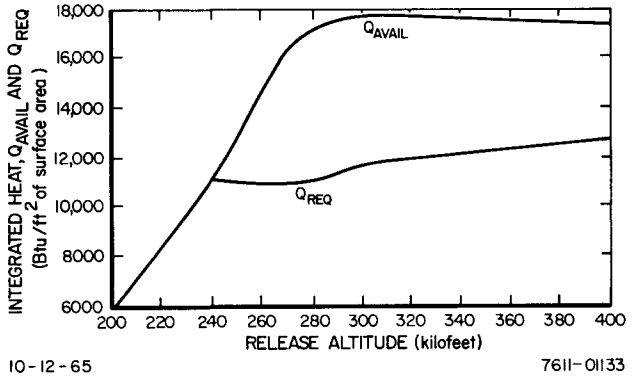

Figure 40. Q_{AVAIL} and Q_{REQ} vs Release Altitude for a SNAP 10A Fuel Element Spinning Cross-Axially, Using the Second Set of Reference Parameters

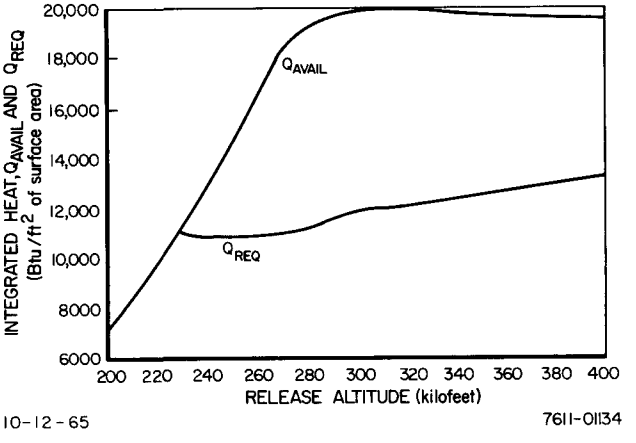

Figure 41. Q_{AVAIL} and Q_{REQ} vs Release Altitude for a SNAP 10A Fuel Element Tumbling at Random, Using the Second Set of Reference Parameters

C. EXTENDED STATISTICAL ANALYSIS

The preliminary set of reference parameters was enlarged as the study progressed and standard values therein were altered as more precise data became available. A second set of reference values which includes three additional parameters and the latest values of all the other parameters was used in the analytical model prior to the publication of this report. The additional parameters investigated are fuel melting temperature, catalytic efficiency of the fuel element surface, and an approximation of the error inherent in the analytical solution. Three of the parameter values used in the preliminary analysis were changed when they were incorporated into the second set of reference parameters. These parameters are initial fuel element temperature, the heat of oxidation, and the hydrogen heat of dissociation for the fuel in the delta phase. The initial fuel temperature was increased to more closely approximate predicted temperatures of the fuel rods upon release from the reactor. (See Section IV for a detailed discussion of the refined value of the heat of oxidation.) Figure 15 shows the value of the hydrogen heat of dissociation for the delta phase fuel used in the second set of reference parameters. All other parameter values used in the second reference set are the same as those used in the preliminary analysis.

As with the preliminary set of reference values, a constant aerodynamic heat input rate of 100.0 Btu/ft^2-sec was used to evaluate Q_{REQ} using the second set of reference parameters. This value of Q_{REQ} was found to be 10,855.0 Btu/ft^2.

The same method that was used previously to evaluate the range of deviation in Q_{REQ} due to the range of deviation in a particular parameter was also used to obtain $(\Delta Q_{REQ})_{\text{given parameter}}$ values for each parameter in the second set of reference values.

The standard values and the estimated uncertainty ranges for the second set of reference parameters are listed in Table 16. Also given in Table 16 are the values of ΔQ_{REQ} for each parameter. Parameters in Table 16 are listed according to their effect upon Q_{REQ}.

Those parameters that are given a standard value of 1.0 in Table 16 are discussed in detail in Section V. Values of ΔQ_{REQ} for each parameter in the second set of reference values were also substituted into Equation 55 to obtain $2\sigma_{Q_{REQ}} = 2900$ Btu/ft^2.

Thus, Q_{REQ} for the analytical model, using the second set of reference parameters, was found to be 10,855 $\pm$1450 Btu/ft^2.

Aerodynamic heating rates were substituted into the analytical model using the second set of reference parameters to determine the value of Q_{REQ} for simulated cross-axial-spinning and random-tumbling modes of reentry. Various release altitudes from 200,000 to 400,000 ft were considered. Figure 40 shows Q_{AVAIL} and Q_{REQ} as a function of release altitude for a cross-axial mode of reentry. Figure 41 gives Q_{AVAIL} and Q_{REQ} vs altitude for random-tumbling reentry.

Since no change was made in the standard reference trajectory parameters, previously determined values of $Q_{AVAIL} \pm \sigma_{Q_{AVAIL}}$ could be applied in the extended analysis for a cross-axial, spinning mode of reentry. For a random-tumbling mode, it was necessary to conduct a separate parameter survey to reestablish parameter variation effects. For this case, 2σ deviations in the

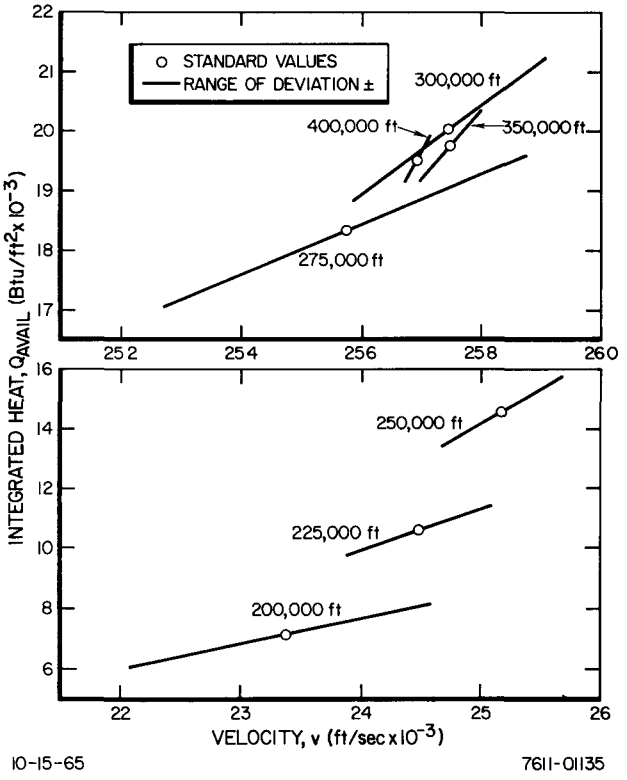

Figure 42. Influence of Velocity on Heat Available to Reentering SNAP 10A Fuel Element Tumbling at Random

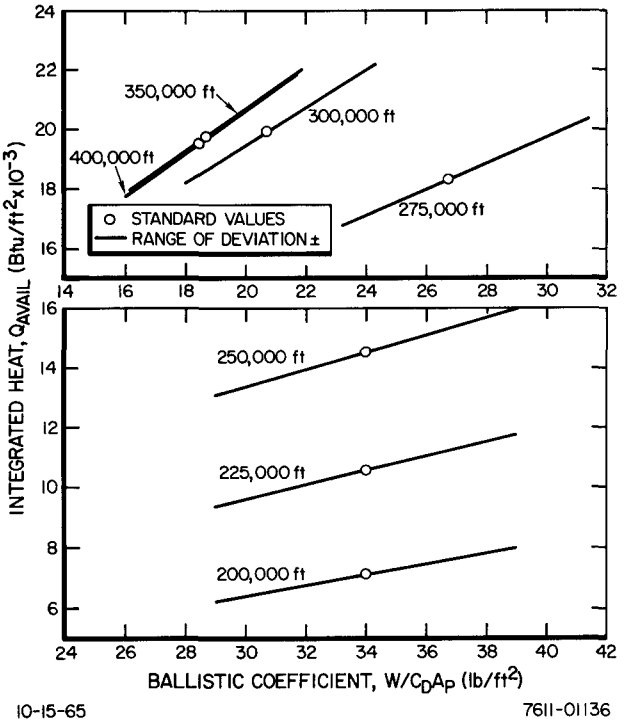

Figure 43. Influence of Ballistic Coefficient on Heat Available to Reentering SNAP 10A Fuel Element Tumbling at Random

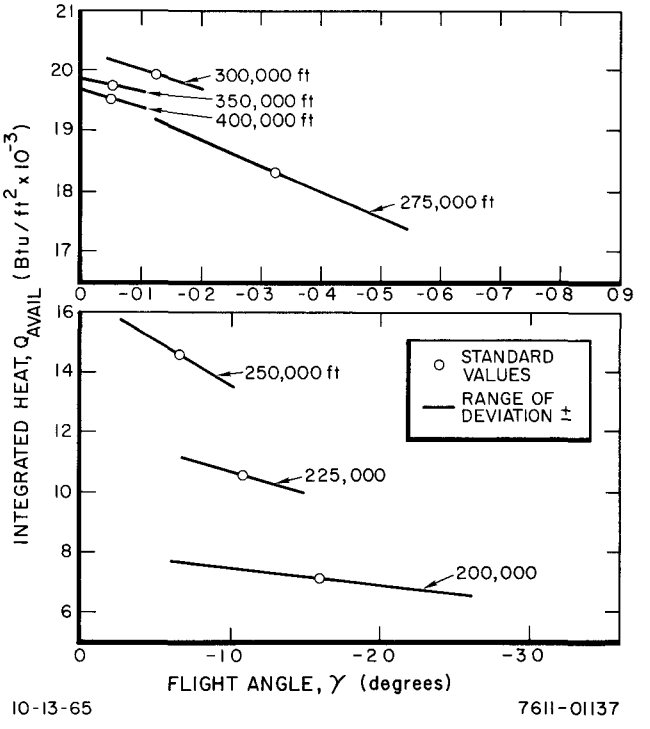

Figure 44. Influence of Flight Path Angle on Heat Available to Reentering SNAP 10A Fuel Element Tumbling at Random

individual trajectory parameters were chosen identical to those in the cross-axial case. Calculations were made varying each parameter separately to obtain influence coefficients. The deviations in Q_{AVAIL} were then determined, using the methods discussed previously, for 2σ deviations in each trajectory parameter.

The resulting influence coefficients and the parameter confidence limits and standard values used in this parameter survey are summarized for the release altitudes considered in Table 17 and in Figures 42 through 44. The deviations in Q_{AVAIL}, resulting from 2σ variation of each trajectory parameter, are shown in Table 18. Using these values, overall 2σ confidence limits and, thus, standard deviations were calculated for the random-tumbling case at each release altitude. Finally, probabilities of initial ablation were then determined for both modes of reentry considered, according to the procedure discussed previously.

TABLE 17

RESULTS OF THE PARAMETER SURVEY FOR Q_{AVAIL} FOR SNAP 10A FUEL ELEMENTS TUMBLING AT RANDOM

Release Altitude (ft)	Influence Coefficients			Deviations (2σ)			Standard Values		
	$\frac{\partial Q_{AVAIL}}{\partial v}$	$\frac{\partial Q_{AVAIL}}{\partial (W/C_D A_p)}$	$\frac{\partial Q_{AVAIL}}{\partial \gamma}$	v (ft/sec)	$W/C_D A_p$ (lb/ft^2)	γ (degrees)	v (ft/sec)	$W/C_D A_p$ (lb/ft^2)	γ (degrees)
200,000	0.875	177.42	-562.5	±1200	±5.0	±1.0	23,379	34.0	-1.6030
225,000	1.357	242.19	-1410.3	±600	±5.0	±0.4	24,487	34.0	-1.0831
250,000	2.313	291.67	-3000.0	±500	±5.0	±0.4	25,179	34.0	-0.6621
275,000	4.380	440.0	-4282.0	±300	±4.11	±0.2	25,578	26.76*	-0.3240
300,000	7.500	631.80	-3077.0	±160	±3.18	±0.08	25,746	20.70*	-0.1252
350,000	11.580	706.0	-2083.0	±50	±2.86	±0.05	25,749	18.69*	-0.0531
400,000	18.00	721.0	-2702.0	±20	±2.84	±0.05	25,694	18.48*	-0.05

*Initial value

Values of Q_{AVAIL}, $\sigma_{Q_{AVAIL}}$, Q_{REQ}, $\sigma_{Q_{REQ}}$, and probabilities of initial ablation at each release altitude are summarized for cross-axial and random-tumbling reentry in Tables 19 and 20, respectively.

Probabilities of survival (nonablation) for random-tumbling reentry are presented graphically as a function of release altitude in Figure 45. Corresponding probabilities for a cross-axial, spinning mode of reentry are plotted in Figure 46. Figures 47 and 48 show the graphical approximation used to calculate probabilities below the release altitude at which $Q_{REQ} = Q_{AVAIL}$ for random-tumbling and cross-axial-spinning orientations, respectively.

D. SUMMARY

In summarizing the results of the statistical analyses performed, one qualifying statement should be made. The probabilities presented in Tables 15, 19, and 20, and in Figures 38, 45, and 46 are based upon, and strongly influenced by, the values assigned to the various initial conditions, thermophysical properties, and trajectory parameters involved in the computation of Q_{AVAIL} and Q_{REQ}. At the time that each investigation was made, the parameter values and corresponding confidence limits used were believed to be the most appropriate for reentry conditions. Several parameters

TABLE 18

DEVIATIONS IN Q_{AVAIL} DUE TO $\pm 2\sigma$ DEVIATIONS IN THE TRAJECTORY PARAMETERS FOR SNAP 10A FUEL ELEMENTS TUMBLING AT RANDOM

Release Altitude (ft)	$(\Delta Q_{AVAIL})_V$ (Btu/ft^2)	$(\Delta Q_{AVAIL})_{W/C_D A_p}$ (Btu/ft^2)	$(\Delta Q_{AVAIL})_\gamma$ (Btu/ft^2)
200,000	1050.0	887.10	-562.50
225,000	814.2	1210.95	-564.12
250,000	1156.5	1458.35	-1200.0
275,000	1314.0	1807.08	-856.40
300,000	1200.0	2007.86	-246.16
350,000	579.0	2015.63	-104.15
400,000	360.0	2044.80	-135.10

TABLE 19

Q_{REQ} AND Q_{AVAIL} WITH STANDARD DEVIATIONS AND PROBABILITIES OF INITIAL ABLATION FOR CROSS-AXIAL REENTRY USING THE SECOND SET OF REFERENCE PARAMETERS

Release Altitude (ft)	Q_{AVAIL} (Btu/ft^2)	$\sigma_{Q_{AVAIL}}$ (Btu/ft^2)	Q_{REQ} (Btu/ft^2)	$\sigma_{Q_{REQ}}$ (Btu/ft^2)	Probability of Initial Ablation
200,000	5,951	±632	-	±1450	0.0006
225,000	9,145	±706	-	±1450	0.105
239,500	11,185	±830	11,185	±1450	0.50
250,000	13,065	±1064	11,050	±1450	0.8698
250,000	13,065	±848	11,050	±1450	0.885*
275,000	17,025	±1087	11,043	±1450	0.9995
300,000	17,662	±978	11,717	±1450	0.99955
350,000	17,632	±977	12,310	±1450	0.9988
400,000	17,346	±925	12,845	±1450	0.9956

*Values used to calculate probability of initial ablation used in graphical approximation of probabilities for release altitudes below 239,500 ft (see Figure 48)

TABLE 20

Q_{REQ} AND Q_{AVAIL} WITH STANDARD DEVIATIONS AND PROBABILITIES OF INITIAL ABLATION FOR RANDOM-TUMBLING REENTRY USING THE SECOND SET OF REFERENCE PARAMETERS

Release Altitude (ft)	Q_{AVAIL} (Btu/ft^2)	$\sigma_{Q_{AVAIL}}$ (Btu/ft^2)	Q_{REQ} (Btu/ft^2)	$\sigma_{Q_{REQ}}$ (Btu/ft^2)	Probability of Initial Ablation
200,000	7,116	±743	-	±1450	0.0053
225,000	10,577	±782	-	±1450	0.35
229,000	11,110	-	11,110	±1450	0.50
250,000	14,554	±1108	10,862	±1450	0.978
250,000	14,554	±925	10,862	±1450	0.982*
275,000	18,332	±1197	11,093	±1450	0.99994
300,000	19,938	±1176	11,882	±1450	0.999992
350,000	19,749	±1050	12,570	±1450	0.99997
400,000	19,508	±1040	13,251	±1450	0.99977

*Values used to calculate probability of initial ablation used in graphical approximations of probabilities for release altitudes below 229,000 ft (see Figure 47)

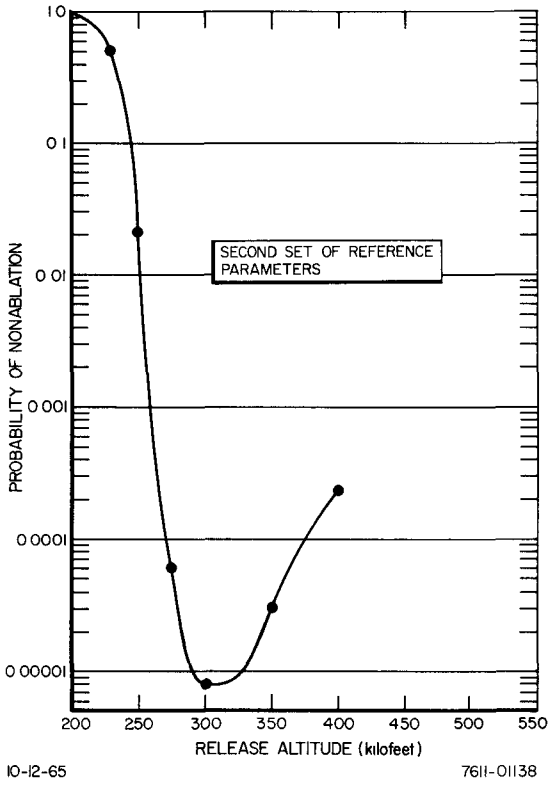

Figure 45. Probability of Survival (Non-ablation) of a SNAP 10A Fuel Element Tumbling at Random vs Release Altitude

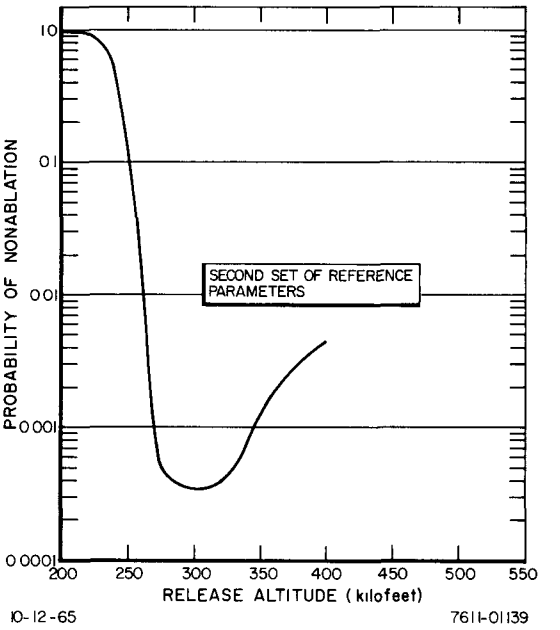

Figure 46. Probability of Survival (Non-ablation) of a SNAP 10A Fuel Element Spinning Cross-Axially vs Release Altitude

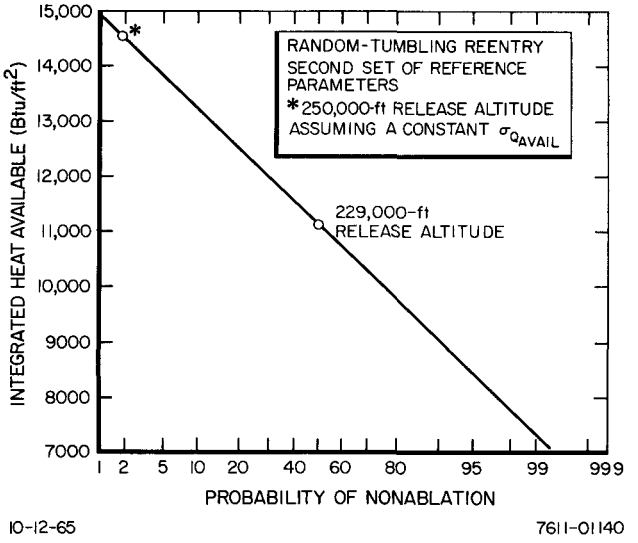

Figure 47. Approximate Probability of Initial Ablation for Release Altitudes Below 229,000 ft

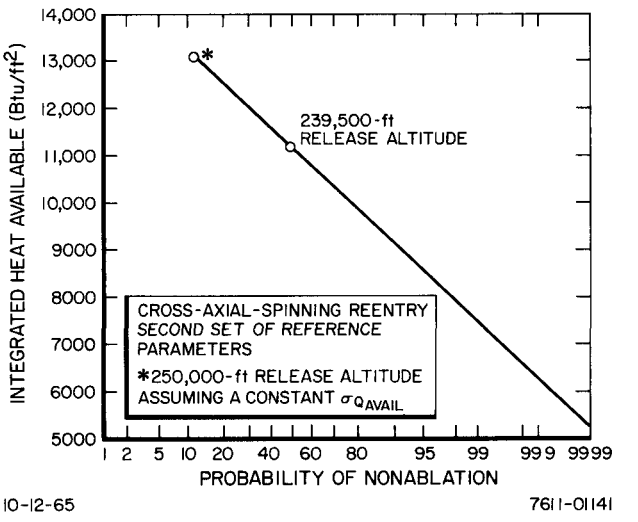

Figure 48. Approximate Probability of Initial Ablation for Release Altitudes Below 239,500 ft

which strongly affect Q_{REQ} are not well defined as to the correct value or to the degree of confidence. Included among these are D, ϵ, q_{oxid}, and k. At the time of this report, an experimental program designed to obtain precise values for these parameters was in progress under the Aerospace Nuclear Safety Program at Atomics International. Once these data are available, it will be necessary to recalculate the probabilities of initial ablation using the same method as outlined in this report.

Both the preliminary and the extended statistical analyses indicate that the optimum release altitude to attain melting and ablation of a SNAP 10A fuel element lies around 300,000 ft. Further, probabilities of initial ablation are enhanced if the fuel element tumbles at random rather than spinning about a stabilized, cross-axial orientation. The maximum probability that a SNAP 10A fuel element will initially ablate is about 0.999992 for an element tumbling at random (see Figure 45) compared to about 0.99966 for an element spinning cross axially (see Figure 46).

Results of the parameter surveys for Q_{REQ} and Q_{AVAIL} have shown the comparative influence of the various parameters and initial conditions on the integrated heats. It was found that cross-coupling effects exist between some parameters so that deviations in the integrated heat due to deviations in these parameters are dependent on the choice of reference parameter values.

Extension of the methods given in this report for calculating the probabilities of complete fuel melting, ablation, and dispersal is planned in future studies.

IX. NOMENCLATURE

A = cross sectional area perpendicular to flow (ft^2)

A_P = projected area of the reentering body (ft^2)

A_S = surface area (ft^2)

C_D = drag coefficient

C_p = specific heat of the fuel material (Btu/lb-°F)

C_{p_c} = specific heat of the cladding material (Btu/lb-°F)

$\overline{C}_p$ = specific heat of hydrogen (Btu/lb-°F)

C_s = concentration of oxygen in the normal shock (lb of O_2/ft^3)

C_w = concentration of oxygen at the fuel surface (lb of O_2/ft^3)

D = hydrogen diffusion coefficient in the fuel material (ft^2/sec)

D_F = hydrogen diffusion coefficient through the oxide film (ft^2/sec)

D_O = diffusivity of oxygen across the boundary layer (ft^2/sec)

F_c = fraction of completion for the hydrogen-oxygen chemical reaction

$F_{\text{given parameter}} = \dfrac{\text{given parameter value}}{\text{standard parameter value}}$

F_s = geometrical shape factor

F_Q = ratio of the average surface heat rate to the stagnation point heat rate

h = heat transfer coefficient for heat flow across the boundary layer (Btu/ft^2-°F)

H_{diss} = heat of hydrogen dissociation (Btu/lb of H_2)

H_s = enthalpy of the air in the stagnation region (Btu/lb of air)

H_w = enthalpy of the air at the wall or surface (specific heat of air times T_s)(Btu/lb of air)

$H_{300°K}$ = enthalpy of the air at a cold (300°K) surface (Btu/lb of air)

ΔH = activation energy for hydrogen diffusion (kcal/mole of H_2)

ΔH_{oxid} = heat of reaction for zirconium oxidation (Btu/lb of O_2)

ΔH_{comb} = heat of reaction for hydrogen combustion (Btu/lb of limiting reactant)

J_O = molecular flux of oxygen diffusing through the boundary layer (lb of O_2/ft^2-sec)

$J_H = \left(D\frac{\partial N}{\partial r}\right)_{r=R_f}$, the net flux of hydrogen injected into the boundary (lb of H_2/ft^2-sec)

J = radial flux of hydrogen diffusing through the fuel material (lb of H_2/ft^2-sec)

K_p = parabolic oxidation rate constant (mg^2/cm^4-sec) or (lb of O_2/ft^4-sec)

L = length of the fuel element (ft)

M = air-to-hydrogen molecular weight ratio

m = mass of reacted oxygen per unit surface area (lb of O_2/ft^2)

$\frac{dm}{dt}$ = rate of mass addition due to fuel oxidation (lb of O_2/ft^2-sec)

M_β = beta phase mass fraction

M_δ = delta phase mass fraction

N = hydrogen concentration (lb of H_2/ft^3)

N_s = hydrogen concentration at the surface (lb of H_2/ft^3)

q_{cyl} = average aerodynamic heat flux to the fuel element for a cold wall (Btu/ft^2-sec)

q_{aero} = average aerodynamic heat flux to the fuel element for a hot wall (Btu/ft^2-sec)

q_{comb} = heat of hydrogen combustion (Btu/ft^2-sec)

q_{ox}, q_{oxid} = heat of fuel oxidation (Btu/ft^2-sec)

q_{tran} = transpiration cooling (Btu/ft^2-sec)

q_{rad} = heat of radiation (Btu/ft^2-sec)

q_{ref} = stagnation point aerodynamic heat flux to the cold wall of a 1-ft radius sphere in continuum flow (Btu/ft^2-sec)

q_{stag} = hot wall stagnation point aerodynamic heat flux to a 1-ft-radius sphere in continuum flow (Btu/ft^2-sec)

q_{net} = $q_{aero} + q_{comb} + q_{oxid} + q_{tran}$, the net surface heat rate (Btu/ft^2-sec)

q_{fm} = free-molecular, stagnation point aerodynamic heat flux to a cold wall (Btu/ft^2-sec)

Q_{AVAIL} = integrated, average aerodynamic heat flux (for a cold wall) available in the fuel element trajectory (Btu/ft^2)

Q_{REQ} = integrated, average aerodynamic heat flux (for a cold wall) necessary to initiate ablation (Btu/ft^2)

R = gas constant (kcal/mole-°F)

R_f = radius of the fuel (ft)

R_o = outer radius of the fuel elements (ft)

T = temperature (°F)

T_c = cladding temperature (°R)

T_M = melting temperature (°F)

T_s = surface temperature of the fuel (°R)

t = time

V = volume (ft^3)

v = velocity (ft/sec)

W = fuel element weight (lb)

W/C_DA_p = ballistic coefficient, mass-to-drag area ratio (lb/ft^2)

ΔX = cladding thickness (ft)

α_A = diffusivity of heat across the boundary layer (ft^2/sec)

γ = flight angle (degrees)

γ_A = catalytic efficiency of the fuel surface

ϵ = emissivity of the fuel

ϵ_c = emissivity of the cladding material

σ = standard deviation

σ_1 = Stephan-Boltzman constant ($Btu/ft^2\text{-}sec\text{-}°R^4$)

$\Delta\tau_1$ = thickness of the oxide film (ft)

ρ = density of the fuel material (lb/ft^3)

ρ_c = density of the cladding material (lb/ft^3)

ρ_A = air density (lb/ft^3)

ρ_{SL} = air density at sea level (lb/ft^3)

BLANK

X. REFERENCES

1. R. D. Elliott, "Aerospace Safety Reentry Analytical and Experimental Program, SNAP 2 and 10A," NAA-SR-8303 (September 30, 1963)

2. R. D. Elliott, "Aerospace Safety Program SNAP 10A Reentry Flight Demonstration (RFD-1) — Analysis of Flight Test Data," NAA-SR-9479 (July 15, 1964)

3. D. K. Nelson, "Behavior of SNAP 10A During Orbital Reentry," NAA-SR-9723 (July 15, 1964)

4. R. D. Elliott, "Disintegration and Dispersion of the SNAP 10A Reactor Upon Return from Satellite Orbit," NAA-SR-11103 (September 1, 1965)

5. Lockheed Missiles and Space Co., "SNAP 10A/Agena Reentry Dynamics for Aerospace Nuclear Safety," LMSC/A735412 (February 15, 1965)

6. AVCO Corporation, Research and Advanced Development Division, "Investigation of the Reentry Destruction of a Nuclear Auxiliary Power Plant," AFSWC-TR-61-69 (October 1961)

7. H. M. Childers, et al., "Reentry Burnup Model for a Hydrided Zirconium-Uranium Fuel Element," WL-TDR-64-15 (February 1964)

8. B. M. Leadon, et al., "A Preliminary Thermal Degradation Computer Model for Reentering Nuclear Auxiliary Power Systems," WL-TDR-64-80 (October 1964)

9. J. W. Baughn, "SNAP Fuel Reentry Burnup Experiment in a Hyperthermal Wind Tunnel," NAA-SR-9779 (October 15, 1964)

10. A. R. Dayes, W. A. Flynn, and J. P. Hawley, "SNAP 10A Reactor Nuclear Analysis," NAA-SR-9754 (Secret RD)(January 15, 1965)

11. J. A. Fay and F. R. Riddell, "Theory of Stagnation Point Heat Transfer in Dissociated Air," J. of the Aeronautical Sciences, 25, (1958) p 75

12. N. H. Kemp and F. R. Riddell, "Heat Transfer to Satellite Vehicles Reentering the Atmosphere," AVCO Research Report 2 (October 1956)

13. R. W. Detra and H. Hidalgo, "Generalized Heat Transfer Formulas and Graphs for Nose Cone Reentry into the Atmosphere," ARS Journal, 31, (March 1961) p 318

14. G. J. Maslach and S. A. Schaaf, "Cylinder Drag in the Transition from Continuum to Free-Molecule Flow," The Physics of Fluids, Vol 6, No. 3 (March 1963)

15. D. Cubicciotti, "The Oxidation of Zirconium at High Temperatures," J. Am. Chem. Soc., 72, (September 1958) p 4138

16. S. D. Harkness, "The Oxidation Kinetics of SNAP Fuel," NAA-SR-MEMO-10914 (Confidential RD)(January 18, 1965)

17. C. D. Hogman, Handbook of Chemistry and Physics, 41st Edition, (Chemical Rubber Publishing Co., Cleveland, Ohio)

18. N. A. Bethe and M. C. Adams, "A Theory for the Ablation of Glassy Materials," AVCO Research Report 38 (November 1958)

19. S. Georgiev, "Hypersonic Ablation and Interpretation of Test Results," AVCO Research Report 99 (October 1960)

20. R. G. Fowler, "A Theoretical Study of the Hydrogen-Air Reaction for Application to the Field of Supersonic Combustion," Proceedings of the 1962 Heat Transfer and Fluid Mechanics Institute, (Stanford University Press) p 279

21. A. W. Barsell, L. D. Montgomery, and J. T. Roberts, "Bibliographical Survey of SNAP Fuel Materials: Zirconium-Uranium-Hydride and Related Zirconium and Uranium Systems," NAA-SR-9525, Vol I (July 15, 1964) and Vol II (Secret RD)(June 26, 1964)

22. L. D. La Grange, et al., "A Study of the Zirconium-Hydrogen and the Zirconium-Uranium-Hydrogen Systems Between 600 and 800°C," J. of Phys. Chem., 63, (December 1959) p 2035

23. D. F. Atkins, "Dissociation Pressures of Hydrided Zirconium-Uranium Alloys," NAA-SR-4245 (February 15, 1960)

24. S. M. Toy and J. B. Vetrano, "Properties of Zirconium Hydride and Zirconium-Uranium Alloy Hydrides," NAA-SR-4244 (February 1, 1960)

25. H. E. Bigony, et al., "Reaction of Hydrogen with Zirconium-1 and -25 Weight Percent Uranium Alloys," BMI-1359 (July 1959)

26. J. H. Singleton, et al., "The Reaction of Hydrogen with a 50 Weight Percent Alloy of Uranium and Zirconium Between 542 and 798°C," AECU-3630 (November 16, 1956)

27. T. B. Douglas, "High-Temperature Thermodynamic Functions for Zirconium and Unsaturated Zirconium Hydrides," J. of Research, NBS, 67A (September-October 1963) p 403

28. R. E. Taylor, et al., "Pulse Heating of Zirconium-Uranium Hydrides," NAA-SR-7398 (December 30, 1962)

29. R. E. Taylor, "Pulse Heating of Modified Zirconium-Uranium Hydrides," NAA-SR-7736 (February 15, 1963)

30. R. A. Finch, "Rapid Pulse Heating of Modified Zirconium-Uranium Hydrides to Destruction," NAA-SR-10482 (July 24, 1965)

31. J. C. Hedge, et al., "High Temperature Property Study for Reentering NAP Systems," AFSWC-TDR-63-17 (June 1963)

32. A. A. Bauer, "An Evaluation of the Properties and Behavior of Zirconium-Uranium Alloys," BMI-1350 (September 28, 1959)

33. S. G. Nelson, "High-Temperature Thermal Properties of SNAP 10A Fuel Material," BMI-1714 (Confidential)(February 11, 1965)

34. R. E. Taylor and C. J. Ambrose, "Thermophysical Properties of SNAP Fuels," NAA-SR-9782 (Confidential RD)(June 26, 1964)

35. A. C. Crawford, "Thermophysical Properties of SNAP Fuels," NAA-SR-MEMO-10521 (September 18, 1964)

36. T. B. Douglas and A. C. Victor, "Heat Content of Zirconium and of Five Compositions of Zirconium Hydride from 0 to 900°C," WADC-TR-1374, Part II (1958)

37. R. K. Edwards, P. Levesque, and D. Cubicciotti, "Solid Solution Equilibria in the Zirconium-Hydrogen System," J. of Am. Chem. Soc., 77 (1955) p 1307

38. J. W. Droege, "Thermal Diffusion in a Solid Solution of Hydrogen in Beta Zirconium," BMI-1502 (February 24, 1961)

39. T. R. P. Gibb, Jr., "Primary Solid Hydrides," Progress in Inorganic Chemistry, Vol III (Interscience Publishing, 1962)

40. J. W. Raymond, "Equilibrium Dissociation Pressures of the Delta and Epsilon Phases in the Zirconium-Hydrogen System," NAA-SR-9374 (May 31, 1964)

41. P. Gilbert, "Dissociation Pressure of Zirconium Hydride," Part II, General Chemistry Quarterly Progress Report, January-March 1954, NAA-SR-1026 (September 1, 1954)

42. H. E. Johnson, "Hydrogen Dissociation Pressures of Modified SNAP Fuels," NAA-SR-9295 (Confidential RD)(March 15, 1964)

43. D. G. Westlake, "Enthalpy Data for the Zirconium-Hydrogen System," J. of Nuclear Materials, 7 (1962) p 346

44. C. E. Ells and A. D. McQuillan, "A Study of the Hydrogen-Pressure Relationships in the Zirconium-Hydrogen System," J. of the Institute of Metals, 85 (1956) p 89

45. V. V. Sofina and N. G. Pavlovskaya, "Equilibrium States of the Ti-H and Zr-H Systems at Low Pressures," Zhur. Fiz. Khim., 34 (May 1960) p 1104 (In Russian)

46. T. B. Douglas, "The Zirconium-Hydrogen System: Some Thermodynamic Properties from a Heat Content Study," J. of the Am. Chem. Soc., 80 (1958) p 5040

47. G. G. Libowitz, "The Zirconium-Hydrogen System at High Hydrogen Contents," NAA-SR-5015 (August 1, 1959)

48. G. G. Libowitz, "A P-C-T Study of the Zirconium-Hydrogen System at High Hydrogen Contents," J. of Nuclear Materials, 5 (1962) p 228

49. Denver Research Institute Staff, "Research and Development of Metal Hydrides," NP-6836 (April-July 1958)

50. L. A. Girifalco, Atomic Migration in Crystals (Blaisdell Publishing Co., New York, 1964)

51. W. M. Albrecht and W. D. Goode, "The Diffusion of Hydrogen in Beta Zirconium," BMI-1373 (August 1959)

52. W. M. Albrecht and W. D. Goode, "The Diffusion of Hydrogen in Zirconium Hydride," BMI-1426 (March 1960)

53. V. L. Gelezunas, et al., "The Diffusion Coefficients for Hydrogen in Beta Zirconium," J. of the Electrochem. Soc., 110 (July 1963) p 799

54. E. A. Gulbransen and K. F. Andrew, "Diffusion of Hydrogen and Deuterium in High Purity Zirconium," J. of the Electrochem. Soc., 101 (1954) p 560

55. M. W. Mallett and W. M. Albrecht, "Low-Pressure Solubility and Diffusion of Hydrogen in Zirconium," J. of the Electrochem. Soc., 104 (1957) p 142

56. M. Someno, "Solubility and Diffusion of Hydrogen in Zirconium," Japan Institute of Metals Journ., 24 (April 1960) p 249

57. SNAP Aerospace Safety Program, "Quarterly Technical Progress Report, October-December 1963," NAA-SR-9297 (Secret RD)(February 14, 1964)

58. A. Sawatzky, "The Diffusion and Solubility of Hydrogen in the Alpha-Phase Zircaloy-2," CRMet-826 (February 1959)

59. J. F. Hon, "Nuclear Magnetic Resonance Study of the Diffusion of Hydrogen in Zirconium Hydride," J. of Chem. Physics, 36 (1962) p 759

60. E. L. Foster, Jr., et al., "Second Quarterly Progress Report, Phase I: High Temperature Thermal Property Study of U-ZrH_x," SC-DC-64-1019X(Confidential)(May 12, 1964)

61. P. M. Chung, "Hypersonic Viscous Shock Layer of Nonequilibrium Dissociating Gas," Technical Report R-109, Ames Research Center, Moffett Field, California (May 1961)

62. G. R. Inger, "Nonequilibrium Hypersonic Stagnation Flow at Low Reynolds Numbers," SSD-TDR-64-118 (September 1964)

63. G. Burdi, "SNAP Technology Handbook, Vol II, Hydride Fuels and Claddings," NAA-SR-8617 (Confidential RD)(November 15, 1964)

64. R. S. Abrahams and J. L. Fick, Engineering Utilization Manual – Thermal Network Analyzer Program – IBM-709-7090 Computer, Lockheed Missiles and Space Co., TM-59-24-1 (April 28, 1961)

65. T. K. Sherwood and C. E. Reed, Applied Mathematics in Chemical Engineering, (McGraw-Hill Book Co., Inc., New York, 1939)

66. M. R. Spiegel, Statistics, Schaum's Outline Series (Schaum Publishing Co., New York, 1961)

67. B. Ostle, "Notes on Statistics Course Presented by Dr. Bernard Ostle, Rocketdyne" (May 12, 1964)

APPENDIX A
BALLISTIC COEFFICIENT ($W/C_D A_p$) CALCULATIONS FOR A SNAP 10A FUEL ELEMENT

1. Fuel Element Weight

a. Fuel

Density	= 6.09 gm/cc (H/Zr = 1.8)
	= 0.2197 lb/in.^{3}
Radius	= 0.606 in.
Length	= 12.25 in.
Volume	= $\pi(0.606)^2(12.25)$ = 14.12 in.^{3}
Fuel weight	= 3.10 lb

b. Cladding

Density	= 0.317 lb/in.^{3}
Outside radius	= 0.625 in.
Inside radius	= 0.610 in.
Length	= 12.25 in.
End caps:	
Diameter	= 1.25 in.
Thickness	= 0.1 in.
Diameter of Pins	= 0.243 and 0.181 in.
Length of pins	= 0.1875 in.
Tube volume	= $\pi(0.3905 - 0.372)12.25$ = 0.714 in.^{3}
Total end cap volume	= 0.2651 in.^{3}
Cladding weight	= 0.3069 lb

c. Barrier

Density	= 0.092 lb/in.^{3}
Outside radius	= 0.610 in.
Inside radius	= 0.607 in.
Length	= 12.25 in.
Volume	= $\pi(0.0038)12.25$ = 0.1461 in.^{3}
Barrier weight	= 0.0132 lb
Total Element Weight: W	= 3.420 lb

2. Ballistic Coefficients

a. Circular Cylinder in Cross-Axial Flow

For the case of a cylinder in cross-axial flow, the drag coefficient was determined from data[A1]* which discusses cylinder drag in the transition region. The drag coefficient was found to be highly dependent on the Knudsen number, K, at altitudes corresponding to the transition region. Near the continuum flow regime, however, the effect of the Knudsen number on C_D is relatively small.

*Refer to the References listed at the end of Appendix A.

Figure A-1 presents the measured cylinder (any diameter) drag coefficient with Knudsen number at a flow Mach number of approximately 6.0. At large values of Mach number in the continuum regime, C_D becomes essentially independent of the Mach number.

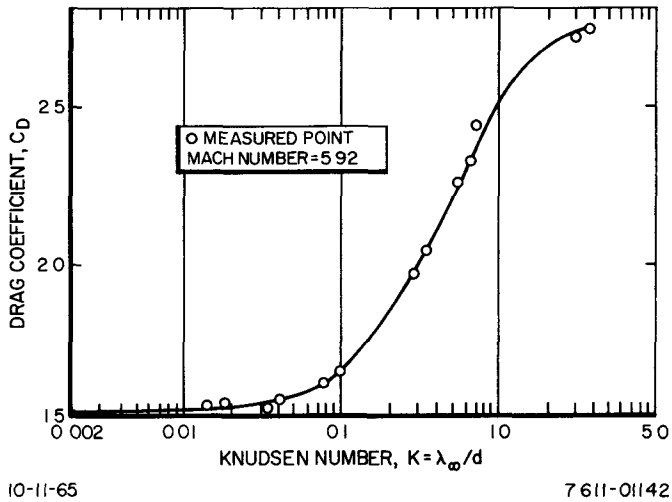

Figure A-1. Cylinder Drag as a Function of Knudsen Number[A1]

In order to incorporate variable cylinder drag in the fuel element trajectory calculations the equation[A1] for the drag coefficient of a unit diameter sphere, from free-molecule to the continuum flow regime, was used. This equation is programmed into the code RESTORE and is

$$C_D = 0.92 + (1.08)\exp\left(-\frac{\rho_\infty d}{10\rho_s\lambda_s}\right), \qquad \ldots(A\text{-}1)$$

where ρ_∞/ρ_s is the density ratio across a normal shock wave and d/λ_s is the reciprocal of the Knudsen number behind the shock wave. The exponential function in Equation A-1 can easily be modified for any diameter by changing the constant, d/10. The free-molecule value of cylinder drag (see Figure A-1) is 2.85 and the approximate continuum flow limit is 1.55. With these upper and lower limit constants, Equation A-1 was modified to fit the data for the drag coefficient of a cylinder. The equation can be written as follows

$$C_{D_{CYL}} = 1.55 + (2.85 - 1.55)\exp\left(-\frac{\rho_\infty d}{A\rho_s\lambda_s}\right), \qquad \ldots(A\text{-}2)$$

leaving only the value of the constant, A, to be determined. Figure A-2 presents the mean free path, λ_∞, and the Knudsen number, λ_∞/d, for a diameter of 1.25 in. as a function of altitude. Using this value of K at specific altitudes, the drag coefficient of a cylinder in cross flow was determined from Figure A-1 and plotted versus altitude in Figure A-3. Applying the values of C_D from Figure A-3 and the calculated values of $\rho_\infty/\rho_s\lambda_s$ from RESTORE computations for a 1-ft sphere, a suitable value for A was calculated to be 1.5 for the SNAP 10A fuel element. Therefore, Equation A-2 becomes

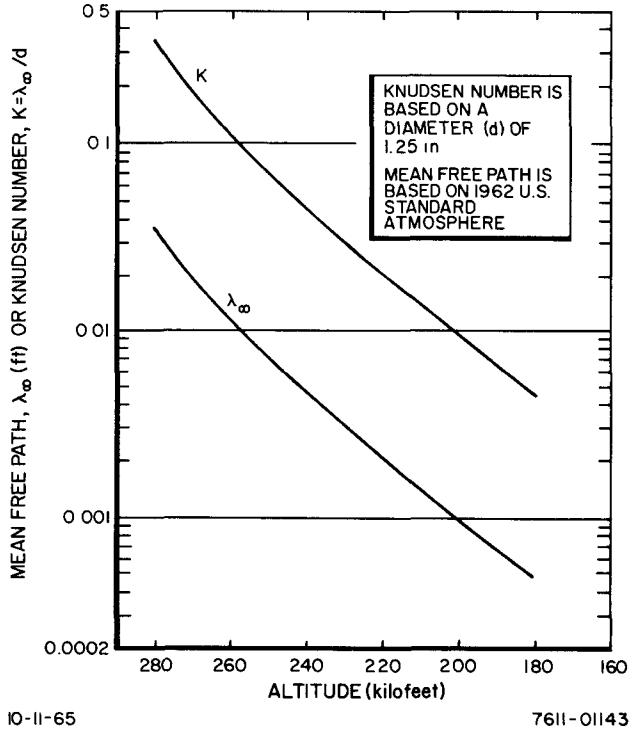

Figure A-2. Mean Free Path and Knudsen Number vs Altitude

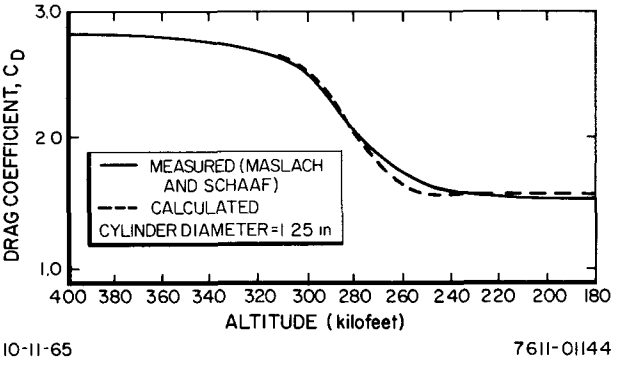

Figure A-3. Drag Coefficient for a Circular Cylinder vs Altitude

$$C_{D_{CYL}} = 1.55 + (1.3)\exp\left(-\frac{\rho_\infty}{1.5\,\rho_s\,\lambda_s}\right) . \qquad \ldots(A\text{-}3)$$

The calculated crossflow drag coefficient from Equation A-3 is shown in Figure A-3 with the curve of measured drag.

Using Equation A-3 for the drag coefficient, the ballistic coefficient for a SNAP 10A element can be computed. At altitudes corresponding to continuum flow, $\overline{C}_{D_{CYL}}$ is, from Figure A-3, 1.55. Then,

$$A_p = d\ell = 0.1080 \text{ ft}^2,$$
$$\overline{C}_D A_p = 0.1674 \text{ ft}^2,$$
$$W/C_D A_p = 20.4 \text{ lb/ft}^2$$

in the continuum regime (altitudes at or below 260,000 ft) for this average drag value.

b. End-Over-End Tumbling

The drag coefficient of a circular cylinder as a function of the angle of attack, α, is

$$C_D = C_N \sin\alpha + C_A \cos\alpha \quad , \qquad \ldots(A\text{-}4)$$

where C_N is the normal force coefficient and C_A is the axial force coefficient. The normal and axial force coefficients are calculated [A2] for a cylinder as

$$C_N = \frac{2d\ell}{3A_{ref}} C_{P_s} \sin^2 \alpha \quad ,$$

and

$$C_A = \frac{\pi d^2}{4A_{ref}} C_{P_s} \cos^2 \alpha \quad ,$$

where A_{ref} is the reference area (cross sectional) and C_{P_s} is the stagnation pressure coefficient based on modified Newtonian theory which relates the local pressure coefficient to Mach number by C_{P_s}; i.e., $C_P = C_{P_s} \sin^2 \delta$ (δ is the angle the body surface makes with the free-stream direction). Therefore, Equation A-4 becomes

$$C_D = B \sin^3 \alpha + E \cos^3 \alpha \quad , \qquad \ldots(A\text{-}5)$$

where B and E are the parameters $(2d\ell C_{P_s}/3A_{ref})$ and $(\pi d^2 C_{P_s}/4A_{ref})$, respectively. The average drag coefficient for one cycle of an end-over-end tumbling cylinder is

$$\overline{C}_D = \frac{\int_0^{\pi/2} B \sin^3 \alpha d\alpha + \int_0^{\pi/2} E \cos^3 \alpha d\alpha}{\int_0^{\pi/2} d\alpha} \quad , \qquad \ldots(A\text{-}6)$$

assuming that orientations of the cylinder at all angles of attack are equally probably; that is, the probability of the rod being at a specified angle of attack is a constant. Integration of Equation A-6 yields (setting $A_{ref} = A_p$)

$$\overline{C}_D = \frac{4}{3\pi}\left(\frac{2d\ell C_{P_s}}{3A_p} + \frac{\pi d^2 C_{P_s}}{4A_p}\right) .$$

Thus,

$$\overline{C}_D A_p = \frac{4}{3\pi}\left(C_{D_{CYL}} d\ell + \frac{\pi d^2}{4} C_{P_s}\right) \quad . \qquad \ldots(A\text{-}7)$$

The term, $C_{D_{CYL}} d\ell$, is that for cross-axial flow and, as given above, has the value 0.1674 in the continuum regime. Therefore, in continuum flow,

$$\overline{C}_D A_p = 0.425 \left[0.1674 + 0.00852(1.94)\right] \quad , \qquad \ldots(A\text{-}8)$$

since $\pi d^2/4 = 0.00852$ ft^2 and $C_{P_s} = 1.94$.

Finally,

$$C_L A_p = 0.0781$$

and the corresponding ballistic coefficient value based on this average drag is $W/C_D A_p = 43.8$ lb/ft (end-over-end tumbling) in the continuum regime.

The ballistic coefficient for end-over-end tumbling at altitudes where $C_{D_{CYL}}$ is not constant is obtained from Equations A-7 and A-3 and can be expressed as

$$W/C_D A_p = \frac{3\pi W}{4}\left(C_{D_{CYL}}\, d\ell + 0.01653\right)^{-1}$$

(end-over-end tumbling) based on an average drag coefficient.

c. Random Tumbling

For the case of a circular cylinder tumbling at random, assuming that orientations of the cylinder at all spherical angles are equally probable, the angle-of-attack probability function, $P(\alpha)$, is equal to $\sin \alpha$. This can be shown by considering the angle of attack, α, at any time during descent according to the following diagram

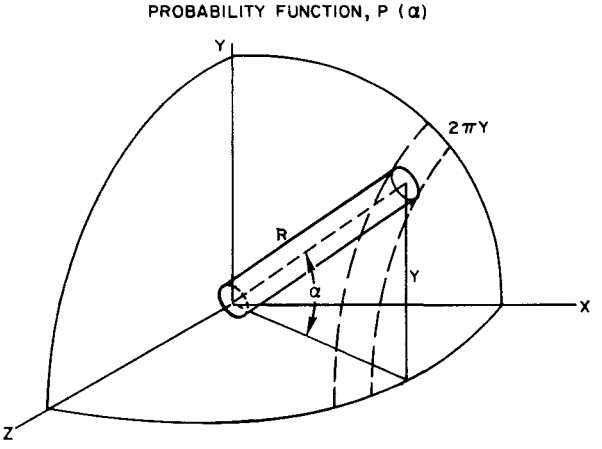

Let the probability of a unit solid angle be the same for all solid angles. Therefore, the relative probability of a given angle of attack, α, to that at $\alpha = 90$ degrees is the ratio of solid unit angles to that at $\alpha = 90$ degrees. The circumference of one cycle through the solid angles is $2\pi Y$, where $Y = R \sin \alpha$. Hence, the relative probability is

$$P(\alpha)_{rel} = \frac{2\pi R \sin \alpha}{\sin 90^\circ}$$

or

$$P(\alpha) = K_1(2\pi R) \sin \alpha = K_2 \sin \alpha \quad ,$$

where K_1 and K_2 are constants. If orientations at all spherical angles are assumed equally probable, i.e.,

$$\int P(\alpha)d\alpha = \int_0^{\pi/2} K_2 \sin \alpha d\alpha = 1 \quad ,$$

then

$K_2 = 1$, and

$$P(\alpha) = \sin \alpha \quad .$$

The average drag for random tumbling is then

$$\overline{C}_D = \frac{\int_0^{\pi/2} P(\alpha)(C_N \sin\alpha + C_A \cos\alpha)d\alpha}{\int_0^{\pi/2} P(\alpha)d\alpha} ,$$

which yields

$$\overline{C}_D = \frac{\int_0^{\pi/2} B \sin^4\alpha d\alpha + \int_0^{\pi/2} E \sin\alpha \cos^3\alpha d\alpha}{\int_0^{\pi/2} \sin\alpha d\alpha} .$$

Integration of the above expression gives

$$\overline{C}_D = \frac{3\pi}{16}B + \frac{1}{4}E ,$$

or

$$\overline{C}_D = \frac{3\pi}{16}\left(\frac{2d\ell C_{P_s}}{3A_p}\right) + \frac{1}{4}\left(\frac{\pi d^2}{4A_p}C_{P_s}\right) ,$$

or

$$\overline{C}_D A_p = 0.589\left(C_{D_{CYL}} d\ell\right) + 0.25\left(\frac{\pi d^2}{4}C_{P_s}\right) .$$

From the values given for $C_{D_{CYL}} d\ell$ and $\frac{\pi d^2}{4}C_{P_s}$ in the continuum regime,

$$\overline{C}_D A_p = 0.589(0.1674) + 0.25(0.0165)$$

or

$$\overline{C}_D A_p = 0.1025 \text{ in continuum flow} .$$

Therefore, using this value,

$$W/C_D A_p = 33.5 \text{ lb/ft}^2 \text{ in continuum flow (random tumbling)} .$$

For altitudes at which $C_{D_{CYL}}$ is not constant, and for an average drag,

$$W/C_D A_p = \frac{W}{0.589}\left(C_{D_{CYL}} d\ell\right)^{-1} + 242.4\, W \text{ (random tumbling)} .$$

References

A1. G. J. Maslach and S. A. Schaaf, "Cylinder Drag in the Transition from Continuum to Free-Molecule Flow," The Physics of Fluids, Vol 6, No. 3 (March 1963)

A2. A. C. Bustamante, "Aerodynamic Analysis and Characteristics of the SNAP 10A Reentry Test Vehicle for the RFD-1 Reentry Flight Test," SC-4927 (RR) (October 1963)

APPENDIX B
MULTI-DIMENSIONAL HEAT AND HYDROGEN TRANSPORT

For several modes of reentry, such as stabilized end-on and nonrotating cross-axial reentry orientations, the one-dimensional analytical model described in the body of this report cannot be applied. In these cases, recourse must be made to two- or three-dimensional models which can be constructed through a logical compounding of methods used in the one-dimensional model. Up to the present time, such multi-dimension models have enabled a description of the fuel element behavior up to the time of initial fuel ablation. Since such ablation begins relatively soon after fuel element release, the usefulness of the present multi-dimensional models is limited. It should be remembered, however, that modes of reentry which effect a nonuniform surface heating around the circumference of the fuel element have not been deemed most probable.

For a reentering SNAP fuel element which remains in a nonrotating cross-axial flight orientation, the aerodynamic reference heat rate, the air stagnation enthalpy, and trajectory properties are identical to those for a cross-axial, spinning element. The aerodynamic heating cannot be averaged around the circumference, however, and a high localized heat rate will be concentrated along the stagnation line. Away from the stagnation line toward the backside of the fuel element, the heating rate will taper off rapidly. The ratio of the local heat rate to the stagnation point heat rate is shown in Figure B-1 as a function of degrees of arc measured from the stagnation line. The heat flux profile in Figure B-1 is obtained from experimental data given in Reference B1.* A similar profile was determined by Baughn(B2)* through experimental calibrations with a calorimeter assembly.

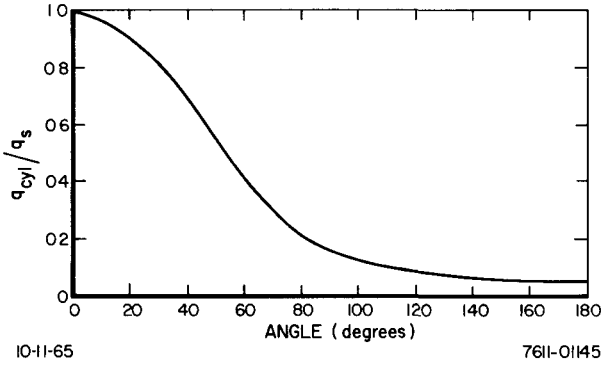

Figure B-1. Heat Flux Distribution Around Periphery of a Nonspinning, Cross-Axial SNAP 10A Fuel Element

Using this heat rate distribution profile shown in Figure B-1 and applying the RESTORE-computed reference heating and stagnation enthalpy transients previously employed (see Figures 3 through 6), a preliminary analysis was made of the fuel element behavior up to initial ablation for a nonrotating, cross-axial configuration. Some simplifications and assumptions were made in this analysis, and these can be listed as follows:

1) End effects were neglected; a uniform heating was assumed along the element axis.

2) The reactions (fuel oxidation, hydrogen combustion and transpiration cooling) at the fuel surface were assumed to produce a net negligible effect.

3) The fuel element is assumed to be unclad at the time of its release from the parent vehicle.

The first of these assumptions is usual procedure which was also adopted in the one-dimensional analysis. The second represents a conservative approach which can be partially justified if one

*Refer to the References listed at the end of Appendix B.

considers the relatively (compared to the one-dimensional case) short time period between release and initial fuel melting. The minor net contribution of the surface reactions toward the total heat input to the element is also a justifying factor The third assumption is justified on the basis of the fact that the cladding portion along the stagnation line of a nonrotating element melts almost immediately after release for release altitudes within the continuum regime.

An analytical model was constructed to describe the fuel material response for the above conditions. The incremental arrangement and typical nodal network for either the heat transfer or the hydrogen transport simulation is shown in Figure B-2 in a cross sectional view. The fuel element

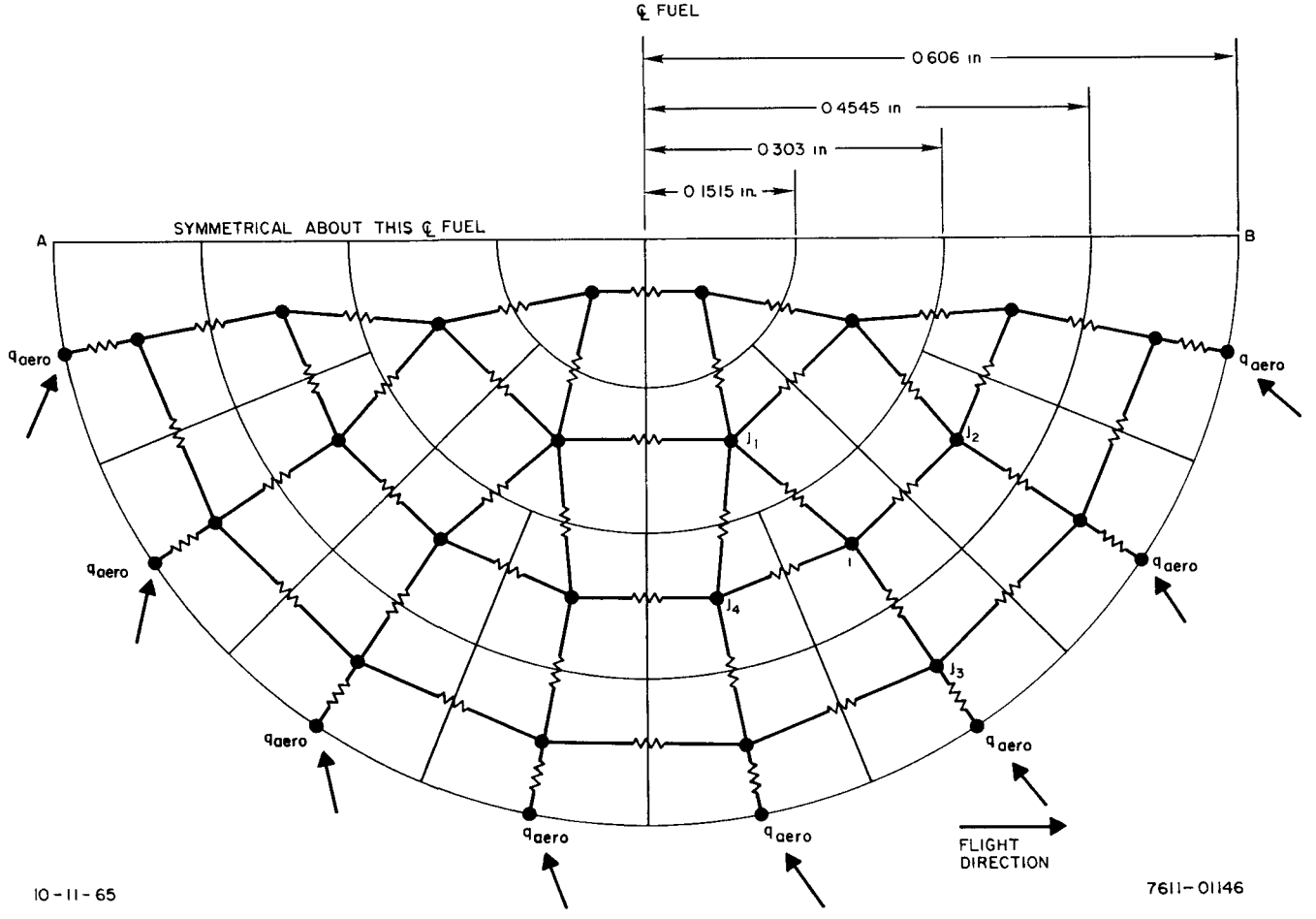

Figure B-2. Two-Dimensional Model for a Nonspinning SNAP 10A Fuel Element Oriented Cross Axially

is broken up into four radial increments with 4, 8, and 16 increments, respectively, in the concentric cylindrical rings. For reasons of symmetry, a half-slice need only be considered in the analysis. In the diagram in Figure B-2, this half-slice is shown to be along the line from point A to point B, where point B represents the stagnation point and point A is 180 degrees removed from B. The direction of flight is along the line from point A to point B.

Flow paths are considered between all increments in this half-slice with nonzero adjoining interfaces. Aerodynamic heating is put into each zero-capacity, surface node in the heat transfer simulation network according to Figure B-1 and the angle formed by point B, the fuel center, and the point represented by the surface node. Hydrogen concentrations at the surface nodes in the hydrogen transport network are held constant and equal to zero throughout the computations. Material properties and initial conditions are consistent with those in calculations made for cross-axial, spinning elements.

The heat and hydrogen continuity equations for pluri-dimensional flow are similar to Equations 6 and 7 except that partial derivaties with respect to radius are replaced by vector gradient operators to account for angular heat flow. The TAP-3 code iterative equations for nonzero capacity nodes are exemplified for a typical node, i, in the incremental arrangement in Figure B-2 by the expressions,

$$T_{i_{t+\Delta t}} = T_{i_t} + \frac{\Delta t}{C_i}\left[Y_{j_1,i}(T_{j_1} - T_i) + Y_{j_2,i}(T_{j_2} - T_i) + Y_{j_3,i}(T_{j_3} - T_i) + Y_{j_4,i}(T_{j_4} - T_i) + Q_i\right]_t , \quad \ldots(B\text{-}1)$$

where

$$Y_{j_1,i} = \left(\frac{kA}{\Delta X}\right)_{j_1,i} - \frac{1}{2}(\bar{C}_p \cdot \vec{Z})_i$$

etc., and

$$Q_i = \frac{H_{diss}}{\Delta t}\left(N_{i_t} - N_{i_{t-\Delta t}}\right)\Delta V$$

for heat transfer, and

$$N_{i_{t+\Delta t}} = N_{t_i} + \frac{\Delta t}{\Delta V}\left[Y_{j_1,i}(N_{j_1} - N_i) + Y_{j_2,i}(N_{j_2} - N_i) + Y_{j_3,i}(N_{j_3} - N_i) + Y_{j_4,i}(N_{j_4} - N_i)\right]_t , \quad \ldots(B\text{-}2)$$

where

$$Y_{j_1,} = \left(\frac{DA}{\Delta X}\right)_{j_1,i}, \quad \text{etc.},$$

for hydrogen transport.

Results of a typical calculation using this two-dimensional model for a cross-axial, nonrotating SNAP 10A fuel element released from 245,000 ft is presented in Figure B-3. The temperature of the fuel near the stagnation point is shown to increase rapidly immediately after release. Initial melting is achieved at 24 sec. As expected, the temperature distribution around the surface follows the general profile in Figure B-1. The minimum surface temperature, at the backside of the element, is about 1400°F at the time of initial melting. The volumetric average temperature of the fuel at this time is about 1750°F. Hydrogen loss within the first 24 sec amounted to about 12%, the hydrogen content decreasing from an initial H/Zr = 1.80 to H/Zr = 1.58 at t = 24 sec.

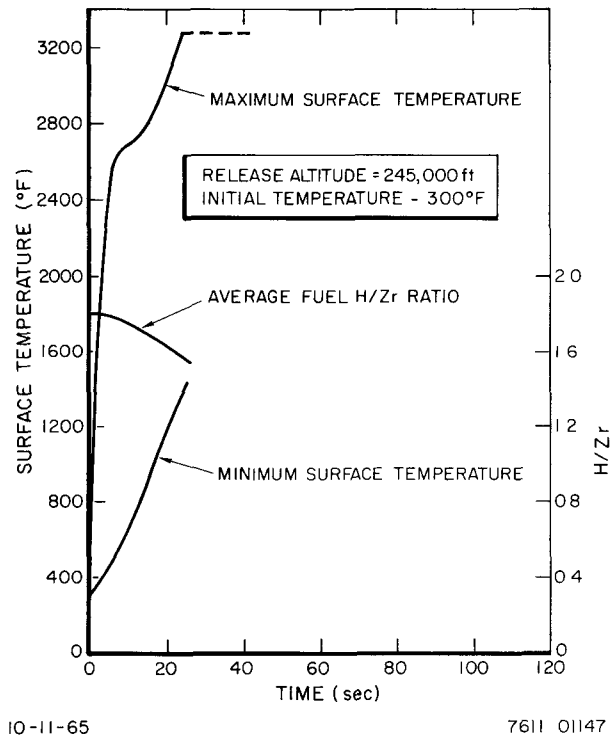

Figure B-3. Calculated Behavior of a Nonspinning SNAP 10A Fuel Element Oriented Cross-Axially

The results show that the time period between release and initial fuel ablation is short for a nonspinning rod in cross-axial flow as compared to a spinning rod (24 sec compared to about 110 sec for a 245,000-ft release altitude). The fuel temperatures up to initial ablation can be accurately computed using the two-dimensional model presented here. After ablation begins, however, uncertainties exist in the manner of variation of the surface heating distribution as the surface contour changes. For this reason, no attempt was made to simulate the ablation process for this case. Further investigations aimed at arriving at better data on particle shear-off and heating variations during ablation are therefore recommended.

References

B1. W. Hagis, "SNAP Programs Upper Atmosphere Experimental Reentry Study," MND-P-2686 (Secret)(March 1962)

B2. J. W. Baughn, "SNAP Fuel Reentry Burnup Experiment in a Hyperthermal Wind Tunnel," NAA-SR-9779 (October 15, 1964)

APPENDIX C
THE HYDROGEN DIFFUSION EQUATION

1. The General Equation

The diffusion of hydrogen out of a SNAP fuel element under reentry heating has a strong bearing on the thermal history of the element. One of the primary objectives, therefore, of the analytical model developed in this report is to describe the hydrogen redistribution throughout the fuel at all times during descent. To achieve this, the model is capable of solving the general diffusion equation, using an empirical diffusion coefficient, with the appropriate boundary conditions.

The fundamental differential equation for the diffusion of atoms or molecules in a homogeneous solid material is, for three dimensional flow,[C1]

$$\frac{\partial N}{\partial t} = -\frac{1}{A_x}\frac{\partial}{\partial x}(A_x J_x) - \frac{1}{A_y}\frac{\partial}{\partial y}(A_y J_y) - \frac{1}{A_z}\frac{\partial}{\partial z}(A_z J_z) \quad , \qquad \ldots(C\text{-}1)$$

where J_x, J_y, and J_z are the net hydrogen fluxes along the x, y, and z axes, respectively. Each of these fluxes may be given as the sum of the individual flows under the respective driving forces of a concentration gradient and a thermal gradient. Thus,

$$J_x = -D\left(\frac{\partial N}{\partial x} + \frac{Q}{RT^2} \cdot N \cdot \frac{\partial T}{\partial x} \cdot C_F\right) \qquad \ldots(C\text{-}2)$$

and similarly for J_y and J_z. In this expression, Q is the heat of transport, a heat quantity on the order of 6 to 12 kcal/mole of H_2.[C2] The quantity, C_F, is a concentration factor which accounts for the reduction in thermal diffusion due to the nonavailability of hydrogen sites in a concentrated solution. In dilute solutions, C_F may be set equal to unity since essentially all sites are unfilled. In the high-concentration phases of the ZrH_x system, C_F can be given by $C_F = (2 - H/Zr)/2$ (see following derivation).

Equation C-1 is the most general form of the hydrogen continuity equation for the migration of hydrogen in nonstoichiometric hydrides. The equation is valid over all phases of the zirconium-hydrogen system since hydrogen in zirconium is known to act as a thermodynamic solution[C3-C5] in any phase. Note that this system must be treated differently than one in which the diffusing substance becomes immobilized or captured by chemical reaction (see, for example, Reference C1, Chapter VIII). Indeed, the experimental studies of Hon[C6] and Stalinski et al.[C7] have shown that the hydrogen atoms in such nonstoichiometric mixtures possess a distinct, continuous activity dependent solely on temperature and hydrogen content. It follows that the net hydrogen flux in such mixtures can always be expressed in terms of the total number of hydrogen atoms and the distribution of these atoms throughout the material. Stated simply, all hydrogen atoms are available to diffuse in such mixtures, there is no immobilizing chemical reaction.

Equation C-1 has been applied, in its one-dimensional form, to hydrogen redistribution in zirconium alloys by Gulbransen,[C3] Sawatzky and Vogt,[C8] and Markowitz,[C9 and C10] among others.

Refer to the References listed at the end of Appendix C.

Generally, these authors discuss analytical closed-form solutions to transient and steady-state hydrogen redistributions under fixed temperature distributions. Further background information on metal-gas solutions in general is contained in References C11 and C12, and on nonstoichiometric hydrides in particular in References C13 and C14.

In the analytical fuel element reentry model, iterative solutions to Equation C-1 were initially achieved using the complete form of the hydrogen flux Equation C-2. This was done by considering the thermal diffusion term in Equation C-2 as a concentration "source," and defining,

$$Q' = -\frac{1}{A}\frac{\partial}{\partial x}\left(-DA\frac{Q}{RT^2}N\frac{\partial T}{\partial x}C_F\right)dV$$

or

$$Q = \frac{\partial}{\partial x}\left(DA\frac{Q}{RT^2}N\frac{\partial T}{\partial x}C_F\right)dx \quad .$$

Applying finite difference forms to the one-dimensional form of the continuity Equation C-1, one then gets,

$$N_{i_{t+\Delta t}} = N_{i_t} + \frac{\Delta t}{\Delta V_i}\left[Y_{i-1,i}(N_{i-1} - N_i) + Y_{i,i+1}(N_{i+1} - N_i) + Q_i\right]_t \quad ,$$

where

$$Y_{i-1,i} = \left(\frac{DA}{\Delta x}\right)_{i-1,i} \quad ,$$

$$Y_{i,i+1} = \left(\frac{DA}{\Delta x}\right)_{i,i+1} \quad , \text{ and}$$

$$Q_i = \frac{-Q}{R}\left[\left(\frac{DA}{T^2}NC_F\right)_{i-1,i}\cdot\left(T_{i-1} - T_i\right) + \left(\frac{DA}{T^2}NC_F\right)_{i,i+1}\cdot\left(T_{i+1} - T_i\right)\right] .$$

This equation has the form of the basic TAP-3 iterative equation for nodes with nonzero capacitances. Evaluating the admittances, $Y_{i,i+1}$, and the nodal source terms, Q_i, at each iteration, the transient hydrogen redistribution equation can be solved by means of the TAP-3 code for the appropriate boundary conditions. Summing up all nodal iterative equations for nonzero capacities and including the boundary Equation 10, one can demonstrate that hydrogen is conserved in the system as a whole. That is, the concentration at time t + Δt can be equated with the concentration at time t minus the hydrogen loss from the surface during the time increment, Δt.

For typical reentry temperature and concentration gradients, it was found by means of direct solution that the contribution of the thermal diffusion term in acting against the hydrogen out-flow was indeed negligible. It was concluded that reentry solutions based on the elimination ($Q_i = 0$) of the hydrogen thermal diffusion term can be deemed satisfactory.

For cases of transient hydrogen redistribution in hydrogen-contained fuel elements, during normal reactor operation, for example, use of the analytical model developed in this report with the application of the appropriate boundary conditions is recommended. In these cases, the thermal hydrogen diffusion effects can be simulated using the hydrogen source terms in the TAP-3 simulation network as explained previously.

2. Jump Frequencies and Activated Hydrogen

Possible interstitial positions for hydrogen atoms in a face-centered (f.c.) unit cell of a metal hydride are shown in Figure C-1. Most transition metal hydrides exhibit this face-centered lattice structure in some phase or another. Delta phase ZrH_x possesses a cubic f.c. crystal structure (c/a = 1). Epsilon phase ZrH_x is a tetrahedral f.c. phase with a variable c/a ratio less than one. The c/a ratio decreases with increasing hydrogen concentration in this phase. The functional decrease is nonlinear and approaches a value of about 0.893[C15] for $H/Zr \longrightarrow 2$. Recent studies[C6, C7, C16] using Nuclear Magnetic Resonance (NMR) have shown that hydrogen atoms occupy only the tetrahedral sites in the hydride phases of zirconium and titanium. Further, the nonstoichiometry of these compounds is attributed to hydrogen vacancies in these tetrahedral sites. It has been observed that the cubic f.c. crystal structure of δ-phase ZrH_x breaks down into one of the two zirconium allotropic phase structures (α, β). This is true for an average hydrogen vacancy concentration of 2.5 or more tetrahedral sites per cubic cell, each cell containing 8 hydrogen sites. Thus, about one out of every four tetrahedral hydrogen sites is vacant for the composition $ZrH_{1.5}$. A further decrease in vacancy concentration leads to a phase transformation at about $ZrH_{1.4}$, according to the phase diagram. The relationship between hydrogen content, N (moles H/unit volume), and hydrogen vacancy concentration is given by[C7]

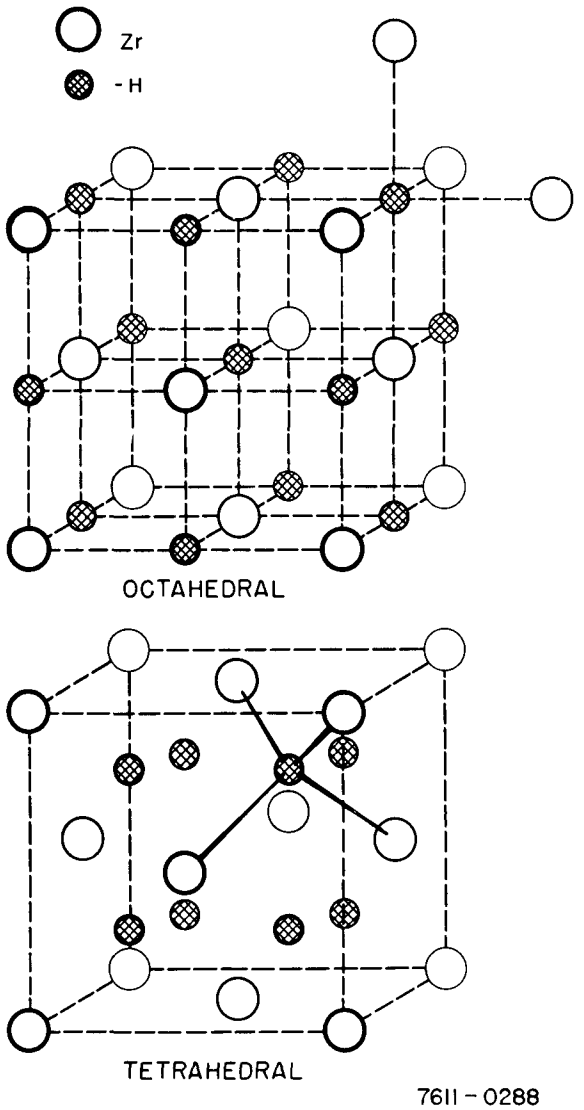

Figure C-1. Possible Interstitial Positions for Hydrogen Atoms in a Metal Hydride Lattice Structure

$$\text{vacancy concentration} = (S - N)$$

$$= C(s - H/Zr) \quad ,$$

where

s = the maximum H/Zr ratio possible (~2)

C = the conversion factor from H/Zr to N (moles/unit volume)

S = s(C), the maximum hydrogen concentration (stoichiometry).

The vacancy concentration decreases slightly for small amounts of foreign atoms in the interstitial positions of the lattice structure. An average sample of ZrH_x (supposedly pure) contains impurities amounting to about 5 foreign atoms for every 100 zirconium atoms. For such a sample, s = 1.95; however, samples of greater purity, up to $ZrH_{1.99}$, have been obtained.

Nonstoichiometric hydrides are characterized by hydrogen motion from vacancy to vacancy, even in the absence of macroscopic concentration gradients. This motion or activation is observed to increase with increasing temperature and decrease with increasing H/Zr ratio. Stalinski, Coogan, and Gutowsky[C7, C16] have expressed the "jump frequency" (the number of times an average atom participates in a diffusion step per sec) in terms of vacancy concentration and temperature according to the relationship,

$$\nu = \frac{k_1}{\Delta\tau} \frac{(S - N)}{S} e^{-\frac{\Delta H}{RT}} \qquad (\text{sec}^{-1}) \qquad \ldots(C\text{-}3)$$

for $1.5 \leq H/Zr \leq 2$ and where

$\Delta\tau$ = length of time for a jump $\approx 10^{-12}$ sec, and

k_1 = dimensionless constant (see Nomenclature at the end of Appendix C).

The composition limits shown confine Equation C-3 to the δ and ϵ phases of the Zr-H system. The equation has been experimentally verified[C7] and can be easily derived. The relationship states simply that the jump frequency is proportional to the product of the probability of an atom having an activation energy, ΔH, and the probability of an adjacent site being vacant. This latter probability has been more correctly formulated by Hon[C6] to be $1 - (N/S)^P$ rather than the $P(S - N)/S$ used in the derivation of Equation C-3. Here, P is the number of neighboring hydrogen sites to which an atom can diffuse. A value of P = 4 has been given by Coogan and Gutowsky for the f.c.c. lattice structure, assuming a diffusion path along the body diagonals of the unit cells. For either formulation of the vacant site probability, similar results are obtained.

Using Equation C-3, then,we can define the concentration of activated hydrogen in the δ and ϵ phases of the Zr-H system as

$$N_A = k_1 \frac{(S - N)}{S} N \cdot e^{-\frac{\Delta H}{RT}} \qquad (\text{moles H/unit vol}) \qquad \ldots(C\text{-}4)$$

The term N_A represents the concentration of hydrogen atoms, at any point x and time t, actually in the process of jumping from one tetrahedral site to another. It is simply the probability of an atom being in a state of motion or activation, at a certain point, multiplied by the concentration of atoms at that point. For this reason, we shall call N_A the activation. Equation C-4 exhibits a behavior characteristic of the experimental observations mentioned before; the activation increases with

increasing temperature and decreases with increasing hydrogen composition. Indeed, $N_A \longrightarrow 0$ for $N \longrightarrow S$; that is, the activation is zero for stoichiometric zirconium hydride.

Now, how can the activation and the jump frequency be defined in the dilute solution phases (α or β) of the Zr-H system? This question is easily answered if we can assume that the probability that at least one neighboring hydrogen site will be vacant is always closely equal to one. This is undoubtedly true for the α-phase where hydrogen concentrations are everywhere extremely low. It should be mentioned at this point that evidence[C6] indicates that there is little preference for a coalescence of hydrogen vacancies. The assumption of random distribution of vacancies is inherent throughout these derivations. If this is so, then the small number of occupied hydrogen sites in α-zirconium renders the probability of finding a vacancy among neighboring sites a virtual certainty.

The body-centered cubic beta phase extends, at higher temperatures, to a maximum H/Zr ratio of about 1.3. There is good reason to believe that hydrogen occupies the octahedral sites in this phase,[C17] possibly in dipolar H-H double occupancy.[C18] It would appear that at least twelve possible paths for diffusion would be available for hydrogen in the octahedral sites, providing diagonal jumping is allowed. For this case, the lowest probability that a neighboring site will be vacant is

$$1 - \left(\frac{H/Zr}{S}\right)^{12} = 1 - \left(\frac{1.3}{1.95}\right)^{12} \approx 1 \quad .$$

Assuming then that a solute hydrogen atom in α- or β-zirconium will always diffuse upon attaining an activation energy ΔH, we may write, for the jump frequency in these phases,

$$\nu = \frac{k_1}{\Delta\tau} e^{-\frac{\Delta H}{RT}} \qquad (\text{sec}^{-1}) \quad . \qquad \ldots(C\text{-}5)$$

The activation is then

$$N_A = k_1 e^{-\frac{\Delta H}{RT}} \cdot N \quad . \qquad \ldots(C\text{-}6)$$

Note that the basic difference between the jump frequencies or the activations in the two cases considered lies only in the vacancy concentration dependency. It will be seen that these differences partition the overall problem of hydrogen redistribution into separate regions, defined by the particular hydrogen flux equation to be used in each phase.

3. Derivation of the Hydrogen Flux Equations

Whenever a hydrogen flux, J, at some point, x, in a hydride is measured, the quantity being determined is the net activation along the considered (x) axis. Consider a cross sectional area, A, at point, x, in a zirconium hydride configuration, as shown in Figure C-2.

Let N, T_1, and N_2, T_2 denote the total hydrogen concentration and the temperature at points x_1 and x_2, respectively. Defining the average velocity of a migrating hydrogen atom to be the average distance traveled in a unit jump (mean free path) divided by the average time required for a jump,

$$v = \frac{\lambda}{\Delta\tau} \quad , \qquad \ldots(C\text{-}7)$$

we may write

$$J_{1\text{-}2} = \vec{N} \cdot v \quad . \qquad \ldots(C\text{-}8)$$

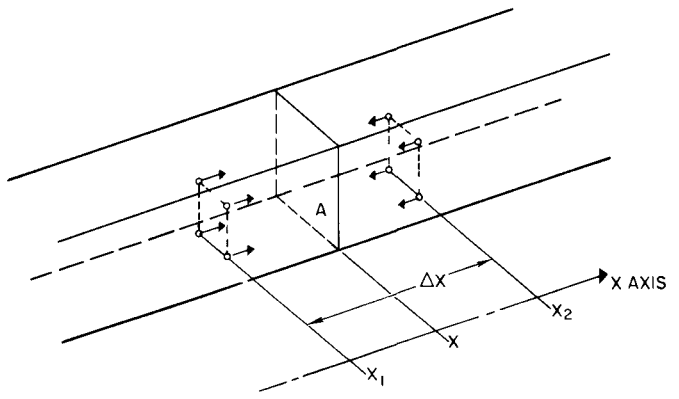

11-9-65 7611-01148

Figure C-2. Configuration Used in Derivation of Hydrogen Flux Equations

This is the basic definition of a flux from a point, x_1, to a point, x_2. The vector quantity, $\vec{N}$, is the concentration of atoms which cross the area, A, in the positive direction of the x-axis. It is the probability that an atom will jump across the area, A, from the point, x_1, multiplied by the concentration of atoms at x_1. Thus,

$$\vec{N} = \frac{\lambda}{\Delta x} \cdot k_2 \cdot \frac{(S - N)}{S} e^{-\frac{\Delta H}{RT}} \cdot N \qquad \ldots (C-9)$$

for the hydride phases of the Zr-H system. Here, k_2 is some fraction of the constant, k_1, used before and $(S - N_2)$ is the vacancy concentration at point x_2. The factor, $\lambda/\Delta x$, is necessary since some atoms starting from x_1 never reach x_2, if $\lambda < \Delta x$. The flux, J_{1-2}, would be correspondingly increased for $\lambda > \Delta x$. Combining Equations C-7, C-8, and C-9, we can write

$$J_{1-2} = \frac{\lambda}{\Delta \tau} \cdot \frac{\lambda}{\Delta x} \cdot k_2 \frac{(S - N_2)}{S} e^{-\frac{\Delta H}{RT_2}} \cdot N_1 \quad . \qquad \ldots (C-10)$$

Similarly, for the hydrogen flux from point x_2 to x_1, we have

$$J_{2-1} = \overleftarrow{N} \cdot v$$

$$J_{2-1} = \frac{\lambda}{\Delta \tau} \cdot \frac{\lambda}{\Delta x} \cdot k_2 \frac{(S - N_1)}{S} e^{-\frac{\Delta H}{RT_2}} \cdot N_2 \quad . \qquad \ldots (C-11)$$

With the above expressions for J_{1-2} and J_{2-1}, we are now able to derive the net hydrogen flux crossing the area, A, under the driving forces of temperature and concentration gradients in δ- or ϵ-phase ZrH_x.

a. Case I Concentration Gradient; No Temperature Gradient

For this case, we have $N_1 > N_2$ and $T_1 = T_2$. Then,

$$J_{net} = J_{1-2} - J_{2-1}$$

$$= \frac{\lambda^2}{\Delta\tau} \cdot k_2 e^{-\frac{\Delta H}{RT}} \left[\frac{N_1(S - N_2) - N_2(S - N_1)}{S \cdot \Delta X} \right]$$

$$= -\frac{\lambda^2}{\Delta\tau} \cdot k_2 e^{-\frac{\Delta H}{RT}} \left[\frac{N_2 - N_1}{\Delta X} \right] .$$

For $x \longrightarrow 0$, we get, in the limiting case,

$$J_{net} = -\frac{\lambda^2}{\Delta\tau} \cdot k_2 e^{-\frac{\Delta H}{RT}} \cdot \frac{\partial N}{\partial X} \quad . \qquad \ldots (C\text{-}12)$$

We define now

$$D \equiv \frac{\lambda^2}{\Delta\tau} \cdot k_2 e^{-\frac{\Delta H}{RT}} \quad , \qquad \ldots (C\text{-}13)$$

which is a standard diffusion coefficient form, and we can write

$$J_{net} = -D \frac{\partial N}{\partial X} \quad . \qquad \ldots (C\text{-}14)$$

b. Case II Temperature Gradient; No Concentration Gradient

For this case, we have $T_1 > T_2$ and $N_1 = N_2$. Then

$$J_{net} = J_{1-2} - J_{2-1}$$

$$= \frac{\lambda^2}{\Delta\tau} \cdot k_2 \frac{(S - N)}{S} N \left[\frac{e^{-\frac{\Delta H}{RT_1}} - e^{-\frac{\Delta H}{RT_2}}}{\Delta X} \right] .$$

For $x \longrightarrow 0$, we get, in the limiting case,

$$J_{net} = -\frac{\lambda^2}{\Delta\tau} \cdot k_2 \frac{(S - N)}{S} \cdot N \frac{\partial}{\partial X} \left(e^{-\frac{\Delta H}{RT}} \right)$$

$$= -D \cdot \frac{Q^*}{RT^2} \cdot \frac{\partial T}{\partial X} \cdot \frac{(S - N)}{S} \cdot N \quad , \qquad \ldots (C\text{-}15)$$

where $Q = \Delta H \cdot f$, f being some function of the order of unity to account for a variable activation energy with temperature or to account for the spatial distribution of the activation energy. (See Reference C19, pages 845-846, and Reference C20.) Equations C-14 and C-15 represent the hydrogen fluxes crossing the area, A, first for a concentration gradient and secondly for a thermal gradient. The signs in the equations show that the hydrogen redistribution is always in the direction of decreasing concentration or temperature. If both gradients serve simultaneously as driving forces, the total flux is the sum of the individual net fluxes,

$$J = -D\left[\frac{\partial N}{\partial X} + \frac{Q}{RT^2} \cdot \frac{\partial T}{\partial X}\frac{(S - N)}{S}N\right] \quad . \qquad \ldots(C\text{-}16)$$

With the derivation outlined above, we thus obtain a hydrogen flux in terms of N and temperature for the hydride phases of the Zr-H system. If the method of derivation is correct, we should be able to derive also the standard flux equation,

$$J = -D\left(\frac{\partial N}{\partial X} + \frac{Q}{RT^2}\frac{\partial T}{\partial X}N\right) \quad , \qquad \ldots(C\text{-}17)$$

given in the literature (obtained using irreversible thermodynamics) for hydrogen in a dilute solid solution. Note that the expression obtained for the hydrogen flux in the hydride phases is not applicable to the dilute solution phases because of the differences in the mechanism of diffusion.

For the solution phases, the probability of an atom jumping from the point, x_1, across the area, A, is then,

$$\frac{\lambda}{\Delta X} \cdot k_2 \cdot e^{-\frac{\Delta H}{RT}} \quad .$$

We have

$$J_{1-2} = \vec{N} \cdot v = \frac{\lambda}{\Delta \tau} \cdot \frac{\lambda}{\Delta X} \cdot k_2 e^{-\frac{\Delta H}{RT_1}} \cdot N_1$$

and

$$J_{2-1} = \frac{\lambda}{\Delta \tau} \cdot \frac{\lambda}{\Delta X} \cdot k_2 e^{-\frac{\Delta H}{RT_2}} \cdot N_2 \quad .$$

Proceeding as before, we obtain

$$J_{net} = J_{1-2} - J_{2-1} \quad .$$

Thus,

$$J_{net} = -D\frac{\partial N}{\partial X} \text{ for isothermal diffusion as } \Delta X \longrightarrow 0$$

and

$$J_{net} = -D\frac{Q^*}{RT^2}\frac{\partial T}{\partial X} \cdot N \quad \text{for thermal diffusion with constant hydrogen content as } \Delta X \longrightarrow 0$$

The total flux for simultaneous application of temperature and concentration gradients is then the sum of these net fluxes:

$$J = -D\left(\frac{\partial N}{\partial X} + \frac{Q^*}{RT^2} \cdot \frac{\partial T}{\partial X} \cdot N\right) \quad , \qquad \ldots (C\text{-}18)$$

which is identical with Equation C-17.

From experiment, it has been observed that the activation energy for hydrogen in ZrH_x appears to be numerically equal to the heat of transport, Q^*, if the experimental data are evaluated according to the above equations. This is true not only for the dilute solution phases, but for the hydride phases as well.

One of the most interesting results of Equation C-16 is the mathematical form of the steady-state solution ($J = 0$). For a zero hydrogen flux, we get

$$\frac{S \cdot \partial N/\partial X}{(S - N)N} = -\frac{Q^*}{RT^2}\frac{\partial T}{\partial X}$$

or

$$\frac{S - N}{N} = C_1 \cdot e^{-\frac{Q^*}{RT}} \quad , \qquad \ldots (C\text{-}19)$$

where C_1 is a constant of integration. We can compare this steady-state concentration distribution, which holds for δ or ϵ hydride, with the equilibrium distribution obtained for the dilute solution phases from Equation C-18 for $J = 0$.

$$N = C_2 \cdot e^{\frac{Q^*}{RT}} \quad , \quad \text{where } C_2 = \text{constant.} \qquad \ldots (C\text{-}20)$$

We note from Equation C-19 that the hydrogen concentration, N, approaches S, the maximum (stoichiometric) concentration, as T approaches 0°K for the hydride phases. This is the limiting condition to be expected since the activation approaches zero for $T \longrightarrow 0°K$ (see Equation C-4). The inability of Equation C-20 to demonstrate this limiting condition poses a major objection to its use in the hydride phases of the fuel material. Further, evaluations of Q^* data in the hydride phases, according to Equation C-19, can be shown to explain data discrepancies and peculiarities otherwise unresolved.

4. Nomenclature

N = total hydrogen content at point x at time τ (lb of H_2/ft^3)

N_A = concentration of activated hydrogen at point x at time τ (lb of H_2/ft^3)

J = hydrogen flux across unit area in x-direction (lb of H_2/ft^2-sec)

A = cross sectional area perpendicular to the H flow (ft^2)

D = diffusion coefficient (ft^2/sec)

Q^* = heat of transport (Btu/lb of H_2)

R = gas constant (kcal/mole-°K)

T = absolute temperature (°K)

ΔH = activation energy (kcal/mole)

c/a = ratio of the height/width (or depth) of a unit lattice cell

s = maximum H/Zr ratio attainable. Pertains to complete occupancy of all available H sites (stochiometry)

C = conversion factor from H/Zr to N (lb of H_2/ft^3)

$S = sC$ = maximum hydrogen concentration

$\Delta\tau$ = average time for a hydrogen atom jump ($\approx 10^{-12}$ sec)

ν = jump frequency, the frequency at which an average atom will jump (sec^{-1})

P = the number of neighboring H sites about a hydrogen atom to which the atom can jump

k_1 = P times a constant of the order of unity

k_2 = some fraction of the constant k_1 to account for the spatial distribution of the jumping atoms

λ = average distance traveled in a unit jump (ft)

$v = \lambda/\Delta\tau$ = average velocity of a jumping atom (ft/sec)

References

C1. J. Crank, "The Mathematics of Diffusion," (Oxford University Press, 1956)

C2. J. W. Droege, "Thermal Diffusion in a Solid Solution of Hydrogen in Beta Zirconium," BMI-1502 (February 24, 1961)

C3. E. A. Gulbransen and K. F. Andrew, "Diffusion of Hydrogen and Deuterium in High Purity Zirconium," J. of the Electrochem. Soc., 101, (1954) p 560

C4. E. A. Gulbransen and K. F. Andrew, "Solubility and Decomposition Pressure of Hydrogen in Alpha-Zirconium," Trans. Am. Inst. of Mining and Metallurgical Eng., 203, (1955) p 136

C5. T. B. Douglas, "High Temperature Thermodynamic Functions for Zirconium and Unsaturated Zirconium Hydrides," J. of Research, NBS, 67A, (September-October 1963) p 403

C6. J. F. Hon, "Nuclear Magnetic Resonance Study of the Diffusion of Hydrogen in Zirconium Hydride," J. of Chem. Phys., 36, (1962) p 759

C7. B. Stalinski, C. K. Coogan, and H. S. Gutowsky, "Proton Magnetic Resonance Studies of Structure, Diffusion and Resonance Shifts in Titanium Hydride," J. of Chem. Phys. 34, (1961) p 1192

C8. A. Sawatzky and E. Vogt, "Mathematics of the Thermal Diffusion of Hydrogen in Zircaloy-2," CRT-1049 (October 1961)

C9. J. M. Markowitz,"Hydrogen Redistribution in Thin Plates of Zirconium Under Large Thermal Gradients," WAPD-TM-104 (January 1958)

C10. J. M. Markowitz,"The Thermal Diffusion of Hydrogen in Alpha-Delta Zircaloy-2," Trans. Met. Soc. A.I.M.E., 221, (August 1961) p 819

C11. R. M. Barrer, "Diffusion In and Through Solids," (Cambridge Press, 1941)

C12. W. Jost, "Diffusion in Solids, Liquids, and Gases," (Academic Press, 1952)

C13. Advances in Chemistry Series No. 39, Nonstoichiometric Compounds, American Chemical Society, Washington, D.C. (1963)

C14. T. R. P. Gibb, Jr., "Primary Solid Hydrides," Progress in Inorganic Chemistry, Vol. III, (Inter-science Publishing, 1962)

C15. W. L. Korst, "X-ray Studies of δ and ϵ Zirconium Hydrides," NAA-SR-6880 (March 30, 1962)

C16. C. K. Coogan and H. S. Gutowsky, "Diffusion of Hydrogen in the Gamma Phase of Titanium Hydride," J. of Chem. Physics, 36, (1962) p 110

C17. C. E. P. Bevington, S. L. Martin, and D. H. Mathews, "The Absorption of Gases by Titanium and Zirconium," Proc. Intern. Cong. Pure Applied Chem. (London) 11, 3-16 (1947)

C18. O. M. Katz and E. A. Gulbransen, "Occluded Gases in Transition Metals," Chapter 4, Nonstoichiometric Compounds, (Academic Press, N.Y. and London, 1964)

C19. L. S. Darken and R. A. Oriani, "Thermal Diffusion in Solid Alloys," Acta. Met. 2, (November 1954) p 841

C20. R. A. Oriani, "The Unmixing of Metal Solutions by a Temperature Gradient," Thermodynamic and Transport Properties of Gases, Liquids, and Solids, (McGraw-Hill, New York 1959)

APPENDIX D
THE SINGLE-REGION MODEL

The single-region model is characterized by the use of only one node to represent the average temperature or hydrogen content of a fuel sample. This model was originally developed to indicate, in general, the approximate overall burnup characteristics of a SNAP fuel rod during reentry. It was also developed as an interim tool, while the complex model was being developed. The single-region model does not yield temperature or concentration profiles across the rod. Further, it is necessary to accept abrupt phase changes throughout the entire rod rather than sectional changes. Use is made of a calculated shape factor to compute admittance values for hydrogen and heat flows to the rod surface. Again, it is stressed that such a model merely approaches rigorous solutions, the reliability being greater for smaller radii, in the case of radial diffusion. Nevertheless, the model represents an improvement over previous approximations [D1, D2]* inasmuch as the basic equations are solved simultaneously, without the need for further simplifying assumptions.

The basic Equations 6 and 7 describing heat and hydrogen transport after cladding burnoff are simplified for the single-region model, since only the average rod behavior is of interest. They are:

$$V\rho C_p \cdot \frac{\partial T}{\partial t} = k \cdot F_s(T_s - \overline{T}) - H_{diss} \frac{\partial N}{\partial t} \cdot V - Z \cdot \overline{C}_p(T_s - \overline{T}) \qquad \ldots(D\text{-}1)$$

for heat flow where

$\overline{T}$ = the average fuel temperature,

T_s = the fuel surface temperature,

and

$$V \frac{\partial \overline{N}}{\partial t} = -D F_s \overline{N} \qquad \ldots(D\text{-}2)$$

for hydrogen flow. Here, F_s is the geometrical shape factor and $\overline{N}$ is the average hydrogen concentration of the fuel. The shape factor to be used can be calculated for the particular geometry through consideration of a steady-state heat balance. For a cylinder of length, L, the shape factor, F_s, is equal to $8\pi L$.

The finite difference forms of these equations are

$$\overline{T}_{t+\Delta t} = \overline{T}_t + \frac{\Delta t}{\rho C_p V} \left[(kF_s - Z\overline{C}_p)(T_s - \overline{T}) + Q \right]_t \qquad \ldots(D\text{-}3)$$

and

$$\overline{N}_{t+\Delta t} = \overline{N}_t + \frac{\Delta t}{V} \left[DF_s \, (O - \overline{N})_t \right], \qquad \ldots(D\text{-}4)$$

*Refer to the References listed at the end of Appendix D.

where

$$Q_t = -H_{diss}(\overline{N}_t - \overline{N}_{t-\Delta t}) \cdot \frac{V}{\Delta t} = +H_{diss} D F_s \overline{N}_t \quad .$$

At the surface nodes during this period, the heat balance is given by the equation,

$$A_s(q_{net} - q_{rad}) - (k F_s - Z\overline{C}_p)(T_s - \overline{T}) = 0 \quad , \qquad \ldots (D\text{-}5)$$

where

$$q_{net} = q_{aero} + q_{comb} + q_{tran} + q_{oxid}$$

and

$$q_{rad} = \epsilon \sigma T_s^4 \quad .$$

The surface concentration is held constant and equal to zero.

Before cladding burnoff, the transient behavior of the fuel element can be calculated from equations similar to those given in Section III (Equations 1, 2, and 5) plus Equation D-1. In these equations, $\partial N/\partial t = 0$ and $Z = 0$; also the term $k(\partial T/\partial r)\, r = R_f$ in Equation 5 becomes $\frac{kF_s}{A_s}(T_s - T)$ for the single-region model.

The analogous TAP-3 circuit network before cladding melting and burnoff can be described as follows:

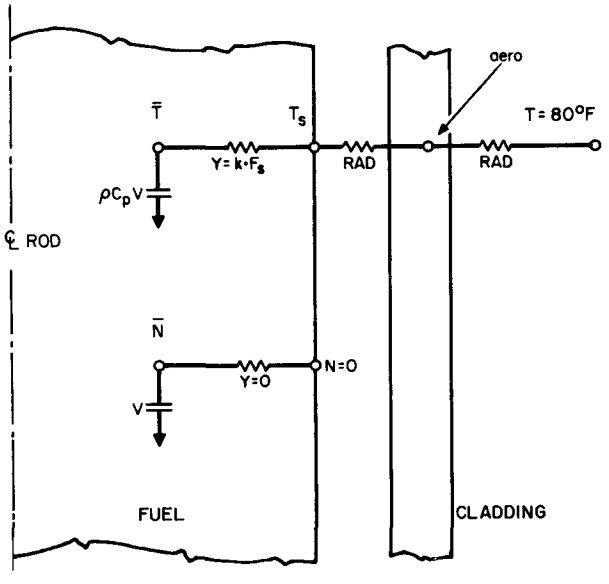

Aerodynamic heating is initially put into the cladding node. The cladding temperature rises and heat is lost by radiation to the surroundings and across the element gap to the fuel surface. It is assumed that the cladding (Hastelloy-N) undergoes melting at 2400°F with a latent heat of fusion of 133 Btu/lb. The hydrogen flow admittance remains equal to zero until cladding meltdown is complete.

After cladding meltdown, the cladding node is excluded from the calculations and radiation from the fuel surface to the environment is computed. For each unit mass of hydrogen which then leaves the rod, an endothermic heat, H_{diss}, is deducted from the heat stored in the fuel. The TAP-3 circuit network is then as follows:

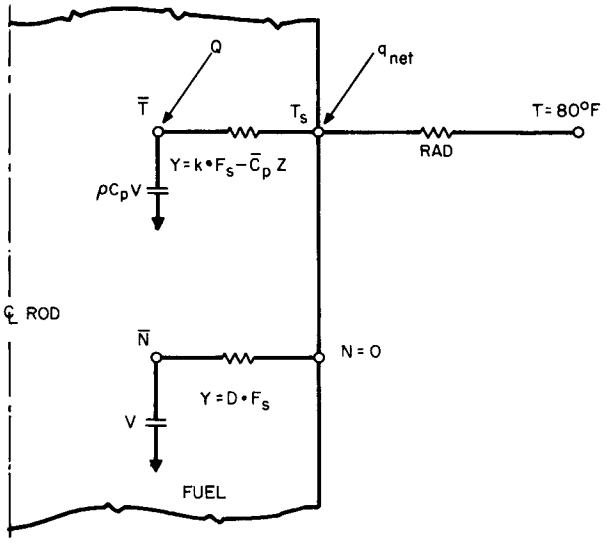

The fuel surface temperature, T_s, the average fuel temperature, T, and the average concentration are computed by means of the TAP-3 code using Equations D-5,D-3,and D-4, respectively. The net surface heating, q_{net}, is specified to the code and calculated as explained in the main body of this report.

When the surface reaches the melting temperature, the net heating is specified to the average fuel temperature fuel node. The fuel reaches and remains at the melting temperature (3280°F) until a heat quantity equal to the latent heat of fusion (90 Btu/lb x 3.1 lb) is absorbed. The calculation procedure is then terminated.

Analytical solutions using this single-region model are deemed sufficiently accurate for most applications, provided that the diameter of the fuel material is small (1/2 in. or less). Approximations of fuel behavior for larger diameters can be made using this model up to limiting sizes dictated by the accuracy desired.

A typical solution using the single-region model for a clad SNAP 10A fuel element under arc-jet conditions is given in Figure D-1. The corresponding solution using the multi-region model outlined in the main body of this report is also shown in Figure D-1. Material properties and initial conditions used in the two solutions were identical. In comparing the two solutions, one notes that the single-region model surface temperature, throughout the period of hydrogen evolution, is maintained at a high, near-constant level until nearly all hydrogen is lost. The time to initial fuel melting is longer for the single-region model case than for the multi-region model case (102 sec as compared to 94 sec). This results in a deviation or error in the total heat required to initiate ablation between the two cases of about 8%.

The single-region model is, of course, not capable of describing the ablation process. Its use is recommended for cases in which a rough estimate of the fuel behavior is desired for a minimum of calculative effort.

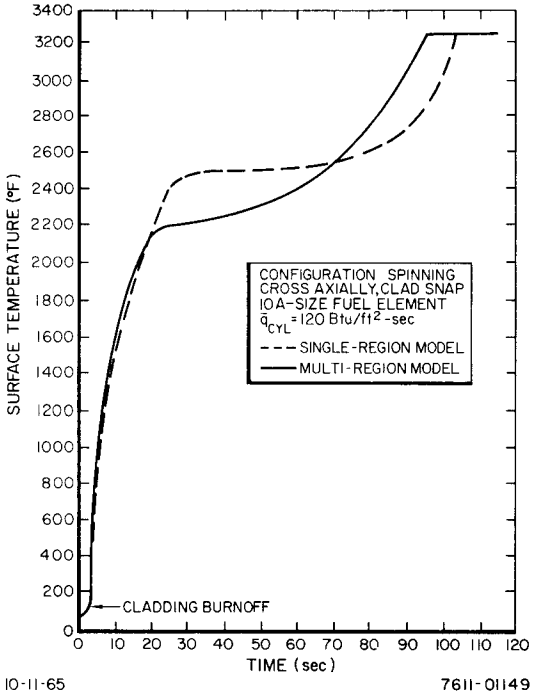

Figure D-1. Comparison of Fuel Surface Temperatures vs Time for Single- and Multi-Region Models

References

D1. J. W. Baughn, "SNAP Fuel Reentry Burnup Experiment in a Hyperthermal Wind Tunnel," NAA-SR-9779 (October 15, 1964)

D2. R. D. Elliott, "Aerospace Safety Reentry Analytical and Experimental Program, SNAP 2 and 10A," NAA-SR-8303 (September 30, 1963)